Electrolyte Design and Engineering for Electrochemical Energy System

by

Jing Zhang

A thesis

presented to the University of Waterloo

in fulfillment of the

thesis requirement for the degree of

Doctor of Philosophy

in

Chemical Engineering

Waterloo, Ontario, Canada, 2019

Examining Committee Membership

The following served on the Examining Committee for this thesis. The decision of the Examining Committee is by majority vote.

External Examiner	Dr. Yongfeng Hu Professor
Supervisor	Dr. Zhongwei Chen Professor
Internal Member	Dr. Eric Croiset Professor
Internal Member	Dr. Jeffrey Gostick Associate Professor
Internal-external Member	Dr. Bo Cui Professor

Author's Declaration

This thesis consists of material all of which I authored or co-authored: see Statement of Contributions included in the thesis. This is a true copy of the thesis, including any required final revisions, as accepted by my examiners.

I understand that my thesis may be made electronically available to the public.

Statement of Contributions

The body of this thesis is based upon a combination of published works. Various chapters are adapted from the following list of publications.

Chapter 3 of this thesis consists of a paper that was co-authored by myself, my supervisor, two post-doctoral fellows, Drs. G. Jiang and A. Kashkooli, two PhD students, P. Xu and M. Mousavi, and one collaborator, Dr. A. Yu. My supervisor, Dr. Z. Chen, directed the research. Dr. G. Jiang and I designed the experiment. I carried out the experiment, collected and analyzed the data, as well as the writing of the manuscript. P. Xu assisted with setting up the experiment station. Dr. A. Kashkooli and M. Mousavi contributed with the design of flow battery configuration. Dr A. Yu assisted with the writing of the manuscript. All authors reviewed the manuscript.

"An All-aqueous Redox Flow Battery with Unprecedented Energy Density", Energy & Environmental Science, 2018, 11, 2010.

Chapter 4 of this thesis consists of a paper that was co-authored by myself, my supervisor, three post-doctoral fellows, Drs. G. Jiang, J. Fu and H. Zarrin, one PhD students, P. Xu, and three collaborators, Drs. A. Yu, X. Song and K. Li. My supervisor, Dr. Z. Chen, directed the research. Dr. J. Fu and I designed the experiment. I carried out the experiment, collected and analyzed the data, as well as the writing of the manuscript. P. Xu assisted with setting up the zinc-air battery configuration. Drs. K. Li and X. Song synthesized and

supplied the raw cellulose fibers. Drs. G. Jiang and H. Zarrin assisted with the functionalization of nanocellulose. Dr A. Yu assisted with the writing of the manuscript. All authors reviewed the manuscript.

"Laminated Cross-linked Nanocellulose/Graphene Oxide Electrolyte for Flexible Rechargeable Zinc-air batteries", Advanced Energy Materials, 2016, 6, 16000476.

Chapter 5 of this thesis consists of a paper that was co-authored by myself, my supervisor, one post-doctoral fellow, Dr. G. Jiang, two PhD students, P. Xu and M. Li, four collaborators, Drs. M. Goledzinowski, F. J. E. Comeau, K. Li and A. Yu, two master students, T. Cumberland and J. Lenos. My supervisor, Dr. Z. Chen, directed the research. Dr. Jiang and I designed the experiment. I carried out the experiment, collected and analyzed the data, as well as the writing of the manuscript. P. Xu, T. Cumberland and J. Lenos assisted with setting up the experiment station. Dr. K. Li synthesized and supplied the raw cellulose fibers. Drs. M. Goledzinowski and F. J. E. Comeau provided technical supports for sensor testing. M. Li and Dr. A. Yu assisted with the writing of the manuscript. All authors reviewed the manuscript.

"Green Solid Electrolyte with Cofunctionalized Nanocellulose/Graphene Oxide Interpenetrating Network for Electrochemical Gas Sensors", Small Methods, 2017, 1700237.

Abstract

Electrochemical energy conversion and storage technology is considered as a promising replacement of fossil fuels to directly convert the chemical energy to electrical energy through electrochemical reactions, which has environmental-benign emissions and excellent operational efficiencies. As key components of an electrochemical device, both electrode and electrolyte will have substantial effects on the performance of an electrochemical energy conversion and storage system. While there have been many research and development concerning electrode materials, the investigations focusing on electrolyte are rather limited. It is worth noticing that the design and preparation of an ideal electrolyte is very necessary, as it plays a critical role in establishing important properties of an electrochemical energy conversion and storage system including internal resistance, thermal stability, power density, energy density, cycle life, and so on.

In this thesis, electrolytes are divided into two types by physical properties, which are liquid electrolyte and solid-state electrolyte. Liquid electrolyte can be further grouped into aqueous and non-aqueous ones based on different solvent utilization, while solid electrolyte can be further separated into all-solid-state and quasi-solid-state electrolytes. Overall, the development of electrolytes is moving from liquid towards solid electrolytes with the rapid growing demand of flexible, foldable, portable, micro and wearable electrochemical devices.

In this work, a novel strategy towards hybrid aqueous electrolyte was firstly put forward for an all-aqueous redox flow battery with unprecedented high energy density.

Theoretically, the electrolyte acidic/basic properties have a great influence on redox pair potential. By tuning the pH of electrolyte, the battery voltage can be effectively enhanced, finally leading to an increase in energy density. Inspired by this concept, an all-aqueous hybrid alkaline zinc/iodine flow battery is designed and demonstrated with a 0.47 V battery potential enhancement compared to the conventional counterpart. Also, a high-energy-density of 330.5 Wh L^{-1} was achieved for this all-aqueous hybrid alkaline zinc/iodine flow battery. It is an unprecedented record for an all-aqueous redox flow battery obtained to date, which is even 1.6 times of the highest reported energy density value. Overall, this hybrid alkaline zinc/iodine system demonstrates a new design with promising performance for an all-aqueous redox flow battery, and more importantly, opens a feasible and effective approach for achieving high-voltage high-energy-density all-aqueous electrochemical energy device.

After that, I present a functionalized nanocellulose-based membrane with a laminated structure to be used as a hydroxide-conducting solid-state electrolyte. The introduced functional groups in the nanocellulose significantly boost the hydroxide conductivity (e.g., 58.8 mS cm^{-1} at 70^{o}C) due to the enhanced ion-exchange capacity and the increased amorphousness of the membrane. Meanwhile, a cross-linking bonding network is formed between the functionalized graphene oxide and nanocellulose, providing the membrane with a superior mechanical property and excellent water retention. The battery using the novel membrane exhibited superior rechargeability and performance stability compared to the commercial A201 membrane. An excellent output power density was achieved when the flexible zinc-air battery was under stress at different bending

angles. This novel membrane will pave the way for future research in the field of flexible energy storage devices, particularly for emerging portable and flexible electronic applications.

In the last study, a functionalized graphene oxide-based membrane with three-dimensional interpenetrating structure was fabricated through a green, efficient and scalable approach. This membrane is used as a proton-conducting solid-state electrolyte in an electrochemical fuel cell gas sensor for the detection of alcohol. The graphene oxide nanosheets are inserted into the whole membrane fibrous skeleton, creating impermeable barrier layers to prevent ethanol gas penetration. The introduced functional groups in the graphene oxide significantly boost the proton conductivity due to the enhanced ion-exchange capacity. Importantly, the modification of graphene oxide facilitates the protons transportation in both in-plane and through-plane channels of the membrane. An alcohol fuel cell sensor equipped with the novel electrolyte membrane was fabricated on the basis of direct ethanol fuel cell principle, exhibiting excellent linearity, sensitivity as well as low ethanol detection limits approaching 25 ppm. This work will pave the way for future research in the field of electrochemical gas sensors as well as the graphene oxide utilization in gas detection application.

In summary, this thesis focuses on the development of electrolytes, including aqueous-based hybrid electrolyte as well as functionalized nanocellulose and graphene oxide based solid electrolytes. Several applications are demonstrated with the presented electrolytes materials, paving the way for future electrolyte research in high-energy-density or flexible wearable electrochemical energy and storage systems.

Acknowledgements

I would like to thank my advisor Professor Zhongwei Chen who gave me the opportunity to pursue my Ph.D. degree, and who guided and encouraged me throughout my Ph.D. studies. He gave me the freedom to pursue various research ideas; without his support, I would never have accomplished so much. Also, I want to thank my Ph.D. thesis examining committee, including Professor Eric Croiset, Professor Jeffrey Gostick, Professor Ali Elkamel, Professor Bo Cui from the University of Waterloo, and Professor Yongfeng Hu as my external examiner from Canadian Light Source / University of Saskatchewan for their time and contributions through this important process.

Here I also would like to thank my colleagues at Applied Nanomaterials and Clean Energy Laboratory, especially those who have worked on zinc air batteries, flow batteries and alcohol fuel cell sensors with me. The knowledge and ideas we shared and exchanged at the healthy and encouraging atmosphere give me hints to tackle challenges from the projects.

Moreover, I would like to express my gratitude to my parents and my husband for their unconditional support, encouragement and love. Dedicated to my parents and my husband for supporting and encouraging me all the time with their love and caring and to my friends who are beside me when I am at my tough time.

Finally, I would like to acknowledge the funding sources, Natural Sciences and Engineering Research Council of Canada, the Waterloo Institute for Nanotechnology, and the University of Waterloo, for the financial support during the completion of my project.

Table of Contents

List of Figures

List of Tables

List of Abbreviations

Electrochemical energy conversion and storage (EECS)

Electrolyte stable potential window (ESPW)

Electric double layer capacitor (EDLC)

Gel polymer electrolyte (GPE)

Solid polymer electrolyte (SPE)

Open-circuit voltage (OCV)

Redox flow battery (RFB)

Fourier Transform Infrared (FT-IR)

Scanning electron microscopy (SEM)

Transmission electron microscopy (TEM)

Energy dispersive x-ray spectroscopy (EDS)

X-ray photoelectron spectroscopy (XPS)

X-ray diffraction (XRD)

Water uptake (WU)

Thermogravimetric analysis (TGA)

Electrochemical Impedance Spectroscopy (EIS)

Standard hydrogen electrode (SHE)

Coulombic efficiency (CE)

Voltage efficiency (VE)

Energy efficiency (EE)

Chapter 1 Introduction

1.1 Motivation

Nowadays, the 21st century is witnessing the huge consumption of energy to meet the demand of booming economy. Fossil fuels, including oil, coal and natural gas, have been the world's main energy source.[1, 2] While the world's fossil fuels are being constantly consumed nowadays, two critical issues of energy crisis and environmental pollution are arising, thus bringing more attention to the public.[3] Firstly, all fossil fuels are finite and will suffer from the end of supplies someday, bring down the economic order with it. Moreover, using fossil fuels for energy has exerted an enormous toll on environment, from air and water pollution to global warming and climate change.[4] Taken together, these unfavorable factors will be huge impediments for future worldwide economic continual development. Investment in science and technology to create sustainable alternatives to fossil fuels is an urgent priority of our society and the development of highly efficient green energy is imperative. Electrochemical energy conversion and storage (EECS) system is considered as a promising replacement of fossil fuels to directly convert the chemical energy to electrical energy through electrochemical reactions, which has environmental-benign emissions and excellent operational efficiencies.[5, 6] Unlike some renewable resources such as large-scale solar and wind-based electricity generation, EECS systems can deliver electricity in more reliable electrochemical methods.

These EECS technologies are now being gradually putted into market in the development of modern portable electronic devices such as laptops and smart phones, as

well as hybrid electrical vehicles, plug-in hybrids, and all-electric vehicles. Supercapacitors, batteries and fuel cells are recognized as three main kinds of the important EECS systems.[7, 8] Based on different conversion and storage mechanisms, these three EECS systems exhibit different electrochemical features. “Energy density” (expressed in watt-hour per liter, Wh/L) and “power density” (in W/L) are two most important properties to be used to evaluate the energy contents and rate capability of a system.[5] The relationship between these two properties can be expressed by Ragone plot to compare the power and energy capabilities.[9, 10] Fuel cells can be regarded as high-energy systems, whereas supercapacitors are considered as high-power systems, leaving batteries in the intermediate position. Although these three EECS systems exhibit different energy storage characteristics, they all own “electrochemical similarities”. In other words, all of them consist of two electrodes separated by an electrolyte. The electrochemical reactions occur on the electrode surfaces, generating ions and releasing electrons. The ions go across the electrolyte to complete the reaction, and the electrons pass through external circuit to power electricity. As key components of an electrochemical device, both electrode and electrolyte will have substantial effects on the performance of an EECS system. While there have been many research and development concerning electrode materials, the investigations focusing on electrolyte are rather limited. It is worth noticing that the design and preparation of an ideal electrolyte is very necessary, as it will influence the performance of an EECS system in different ways.

Electrolyte plays a critical role in establishing important properties of an EECS system including internal resistance, thermal stability, power density, energy density, cycle

life and so on (as seen in **Figure 1-1**). For example, the ionic conductivity of electrolyte has a profound influence on internal resistance of the whole system.[11-15] A high-conductive electrolyte with high ion mobility and low viscosity usually shows outstanding rate capability, which is beneficial for power density.[16] Beside the property of ionic conductivity, the electrolyte potential window also has a major impact on power density, as well as energy density.[17] The operating potential window of an aqueous-based electrolyte is theoretically below 2.0 V, because the voltage of water splitting reaction is about 1.23 V (the potential window of H_2/O_2 evolution reactions at 1.0 atm and room temperature),[18-20] whereas the organic electrolyte or ionic liquid electrolyte can usually be operated above 2.0 V.[21-23] Enhancing the voltage of an EECS system could be one very feasible and effective approach to achieving high energy density. Thus, by optimizing the electrolyte potential window, a promising energy density could be reached. Some thermal properties like boiling point, freezing point, salt solubility et. al. play significant roles in electrolyte stability and thereby affect the EECS system operating temperature range.[13, 17] Non-ideal stability accompanied by the electrolyte degradation and aging phenomenon is also recognized as the leading cause of short cycle life.[24] Actually, it is impossible to design an electrolyte to satisfy all the requirements of an EECS system.

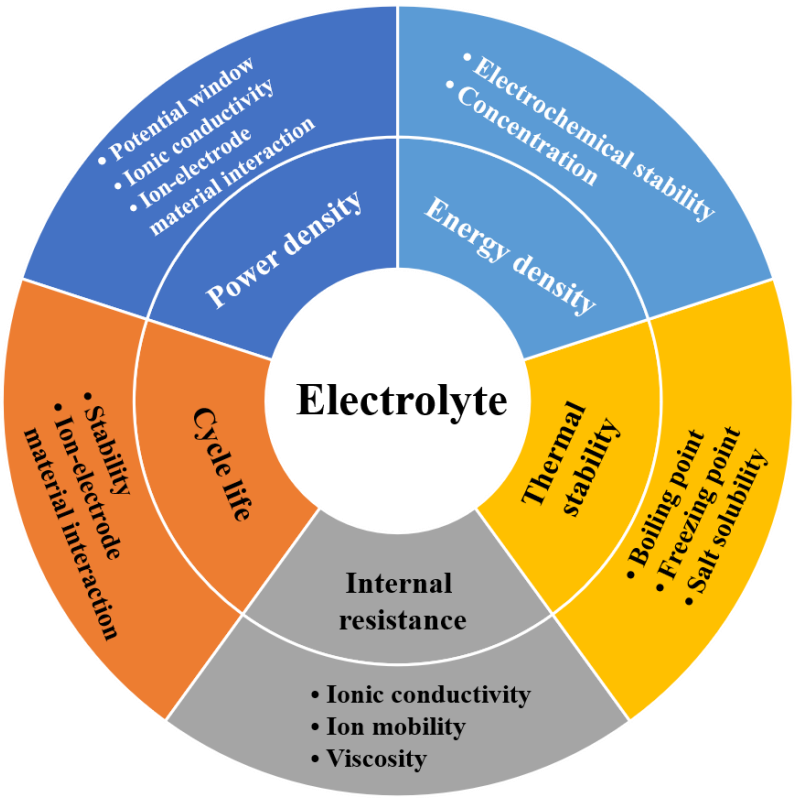

Figure 1-1. Physical, chemical, electrochemical effects of the electrolyte on an EECS system. Reproduced from reference 17, with permission from Royal Society of Chemistry.

1.2 Fundamentals of Electrolytes (materials and compositions) for Electrochemical Devices

A conventional electrolyte is an ionic conductive solution dissolved with salts in solvent. During charge or discharge process of an EECS system, the ions pass through the electrolyte to arrive at two electrodes, facilitating charge compensation and completing chemical reactions.[16] The nature of electrolyte, including the ions size and type; the operating potential window; the physical/chemical/electrochemical stabilities; the interaction with electrode materials; the solvent properties will all contribute to the EECS system performance.[25] In general, an ideal electrolyte is supposed to have following

properties: (1) good ionic conductivity; (2) wide potential operating window; (3) excellent thermal stability; (4) promising electrochemical stability; (5) inertness with electrode materials; (6) low viscosity and non-flammable; (7) environmentally friendly; (8) low cost and easy to commercialize; and so on. Thus, the research and development of electrolyte at present should focus on the overall performance to enlarge its advantages and overcome its drawbacks to fulfill the requirement of one specific EECS system.

To date, various electrolytes have been developed and reported in the literature. As shown in **Figure 1-2**, in this thesis, electrolytes are divided into diffident types by physical properties, which are liquid electrolyte and solid-state electrolyte. With respect to liquid electrolyte, it can be further grouped into aqueous and non-aqueous ones based on different solvent utilization. At present, the majority of electrolytes for most EECS systems is still aqueous-based solution, which has outstanding ionic conductivity owing to high ion mobility and low viscosity.[26-28] Recently, organic-based electrolytes are gradually coming in sight, particularly for lithium ion batteries, because of their high operating potential window superior to others. [29] Ionic-based electrolytes with unique structures and properties are burgeoning, which create more possibilities to electrolyte development and quickly grab researchers' attention.[30, 31] However, these liquid electrolytes all suffer from leaking problem and drying-out issue after a long period of running. Thus, all-solid-state or quasi-solid-state electrolytes are good alternatives with the rapid growing demand of flexible, foldable, portable, micro and wearable electrochemical devices.[32-34] The devices with solid-state electrolytes are simply sharped into multifarious configuration and packaged without leaking and drying-out concerns. Overall, a various of electrolytes have been

designed and developed in recent years, and researchers are becoming aware of their important functions for an EECS system.

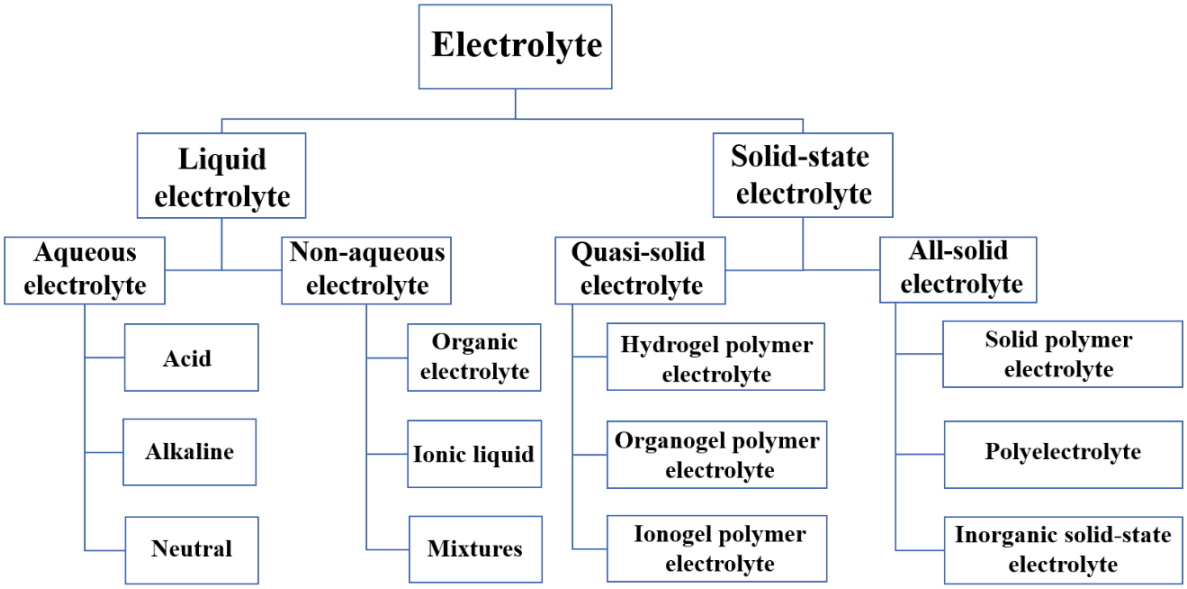

Figure 1-2. Classification of electrolytes for an EECS system. Reproduced from reference 17, with permission from Royal Society of Chemistry.

Aqueous electrolytes can be divided into three types: acid, alkaline and neutral, typically represented by H_2SO_4, KOH and Na_2SO_4. The significant advantage of aqueous electrolyte is its extremely high ionic conductivity compared with non-aqueous or solid-state electrolytes. For example, as the most common-used acid electrolyte, H_2SO_4 has a high ionic conductivity of 0.8 S cm^{-1} (1 M H_2SO_4 at 25 ^oC).[17] Ion concentration has great influence on ionic conductivity.[35, 36] The ionic conductivity cannot reach its highest value if the ion concentration is too high or too low. Most EECS systems use 1 M H_2SO_4 as electrolyte because the maximum conductivity value for H_2SO_4 is obtained at 1 M concentration at 25 ^oC. Same rules also apply for alkaline electrolyte. As shown in **Figure**

1-3, at room temperature (25 ºC), the highest conductivity of KOH solution is achieved at 25 − 30% concentration (7 M KOH).[37] That is why most zinc-air batteries prefer to use 7 M KOH solution as their electrolyte. It is worth noting that some EECS systems can be operated in both acid and alkaline mediums but will under go different electrochemical reactions. Acid and alkaline fuel cells are good examples for explanation and their reactions are as follows.

Acidic

HOR	$H_2 \rightarrow 2H^+ + 2e^-$	$E^o = 0$ V vs SHE	(1-1)
ORR	$1/2O_2 + 2H^+ + 2e^- \rightarrow H_2O$	$E^o = 1.23$ V vs SHE	(1-2)
Overall	$H_2 + 1/2O_2 \rightarrow H_2O$	$E^o = 1.23$ V vs SHE	(1-3)

Alkaline

HOR	$H_2 + 2OH^- \rightarrow 2H_2O + 2e^-$	$E^o = -0.83$ V vs SHE	(1-4)
ORR	$1/2O_2 + H_2O + 2e^- \rightarrow 2OH^-$	$E^o = 0.40$ V vs SHE	(1-5)
Overall	$H_2 + 1/2O_2 \rightarrow H_2O$	$E^o = 1.23$ V vs SHE	(1-6)

Besides acid and alkaline electrolytes, neutral electrolyte (*e.g.* Na_2SO_4) is also widely used in some EECS systems. The advantage for neutral electrolyte is the elimination of corrosion issue in strong acid and alkaline environments.[38] Through the investigation of ion size, ion mobility and ion transportation pathway can be identified and thereby the interaction between electrolyte and electrodes may be evaluated and thereby provide a

possible indication on the electrolyte design and control.

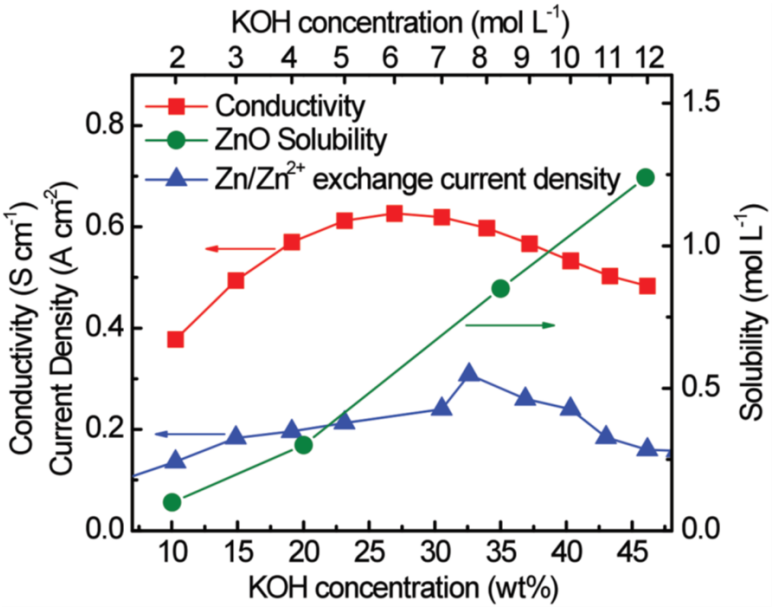

Figure 1-3. Electrolyte conductivity, Zn/Zn^{2+} exchange current density, and ZnO solubility as a function of KOH concentration. Reprinted from reference 37, with permission from John Wiley and Sons.

Generally, aqueous electrolyte is the most commercial category due to its great advantage of safety. Water is the solvent for aqueous electrolyte which is environmentally friendly and non-flammable. Compared with organic solvent, the devices with aqueous electrolyte are easy to be assembled and fabricated with no concerns of special considerations.[39] On the other hand, the organic solvents are usually equipped with some highly active metals, such as lithium and sodium, which are very sensitive to moisture and should be carefully handled in an inert atmosphere.[40]

However, the drawback of narrow operating potential window has largely affected the aqueous electrolyte in achieving its high energy density. As previously mentioned, the EECS devices voltage will be restricted by the potential of water decomposition reaction,

in which the hydrogen evolution reaction occurs at around 0 V *vs.* SHE, while the oxygen evolution reaction potential is about −1.23 V *vs.* SHE. The released gases of hydrogen and oxygen may destroy the package of an EECS device, which could be a potential safety risk.[41]

1.4 Organic Electrolyte

A typical organic electrolyte consists of conductive salt dissolved in organic solvent. The nature of conductive salts and solvents will have profound influence on the EECS systems, such as ion size and type, ion mobility, solvent stability, solvent operating temperature and potential, interactions between conductive salts and solvents, electrolyte stable potential window (ESPW), and so on.[42]

An ideal organic solvent should have the ability to dissolve most conductive salts and provide a relatively high ESPW. Most importantly, it should be quite safe and stable during the charge and discharge running of an EECS device. Unfortunately, the intrinsic properties of organic materials make them at the risk of a flammable, volatile and toxic environment. Thus, the fabrication and assembly process of a device with organic solvent should be very strict without trace of water molecules. Because the presence of any residual impurities (*e.g.*, water) may lead to the EECS system performance degradation.[43] That is why the demand of manufacturing process of organic solvent needs be at very high level and usually costly. The second critical factor for organic solvent is the operating temperature. The lower temperature limits of various organic solvents are different, thereby the resulting in big difference of operating temperature.[44] For example, acetonitrile (ACN)

and propylene carbonate (PC) are two most commonly used organic solvents for electric double layer capacitors (EDLCs). The specific capacitance of the EDLC with 1M ACN organic solvent didn't change with the decreasing temperature, while the capacitance of the EDLC with 1M PC solvent obviously declined when temperature dropped from 60 to −40 °C.[45] A few literatures have been focusing on broadening the operating temperature of an organic solvent, such as some additives.

An ideal conductive salt for an organic solvent is expected to own a high ionic conductivity. Theoretically, the conductivity value is determined by two factors, i.e. ion concentration and ion mobility.[46, 47] The ion concentration of an organic electrolyte is limited to the dissolving ability of solvent with conductive salts, and the ion mobility will largely be affected by the solvent viscosity and ion size. Obviously, the smaller particles have more freedom to transport in the electrolyte. But due to the high viscosity of organic solvent, the ions cannot move as fast compared to the counterpart in aqueous electrolyte, thus resulting in relatively low conductivity. For example, the ionic conductivity of 1M tetraethylammonium tetrafluoroborate ($TEABF_4$) in ACN solvent is about 0.06 S cm^{-1}, whereas the conductivity of 1 M H_2SO_4 at 25 °C is around 0.8 S cm^{-1}.[23]

Aging and degradation of an EECS system with organic solvent are an important issue need to be addressed. Harsh working condition may be the top threat for aging and degradation. As we mentioned previously, the outstanding advantage of organic electrolyte is the wide operating potential window. Some EECS system equipped with organic electrolyte can even reach up to 2.5 − 2.8 V voltage. However, the extremely high voltage is also a big challenge for the electrode materials. At high voltage condition, the electrode

materials may suffer from oxidation risk and some carbon-based electrodes even release some gases, such as CO_2 or CO, which will be possible damage for a sealed battery package.[48] The understanding of aging and degradation process is very important for the protection of an EECS system. Several literatures have started to focus on the mechanism behind this phenomenon, and some experimental approaches and analytic methods have already been applied to deeply understand the mechanism, including quartz-crystal microbalance (QCM),[49] nuclear magnetic resonance (NMR),[50-53] in situ small angle neutron scattering (SANS),[54] in situ Raman microspectrometry,[55] and so on.

1.5 Ionic Liquid Electrolyte

Ionic liquid is a good electrolyte candidate for an EECS system because of its unique physical and chemical properties, including good thermal stability, superior electrochemical stability, low volatility and non-flammability. Ionic liquids are salts composed of solely cations and anions with melting points below 100 ºC, thus it is also known as room temperature molten salts.[21, 56, 57] The commonly used cations of ionic liquids are imidazolium (*e.g.,* $[EMIM]^+$), ammonium (*e.g.,* $[DEME]^+$), phosphonium (*e.g.,* P_{2224}), sulfonium (*e.g.,* $[Me_3S]^+$), pyrrolidinium (*e.g.,* PYR_{14}), and so on. The typically employed anions of ionic liquids are bis(trifluoromethanesulfonyl)imide ($TFSI^-$), bis(fluoro-sulfonyl)imide (FSI^-), hexafluoro-phosphate ($PF6^-$), dicyanamide (DCA^-), tetrafluoro-borate ($BF4^-$). Based on the different cations and anions compositions, ionic liquids can be classified into three types: aprotic, protic and zwitterionic ionic liquids (**Figure 1-4**).[58]

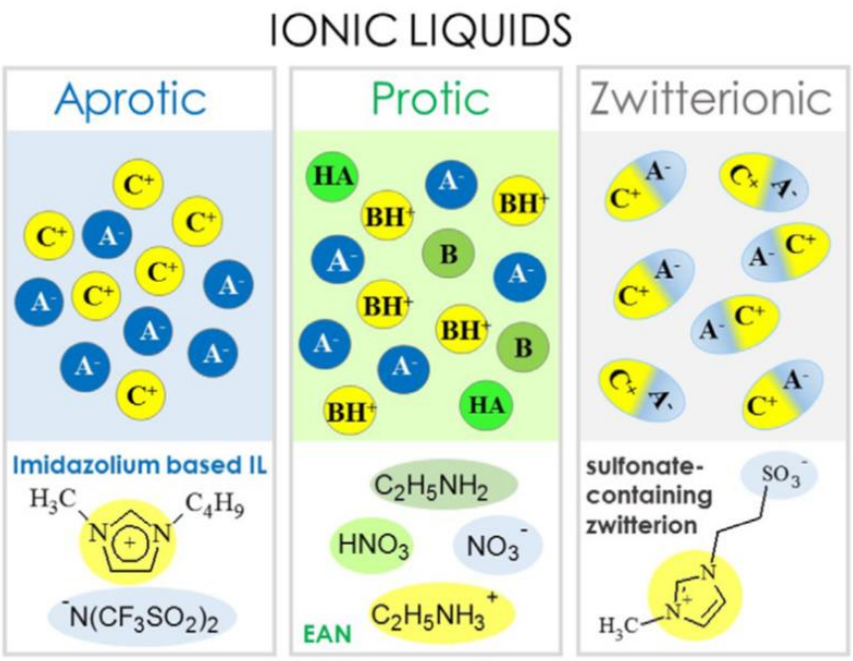

Figure 1-4. Classification of Ionic liquids. Reprinted from reference 58, with permission from IOP Publishing.

Actually, ionic liquids are highly tunable materials which can be designed with the composition of various cations and anions to customize certain physical and chemical properties. This is the most attractive characteristic of ionic liquid which can be used to meet the requirement of some specific EECS systems through the optimization of anion and cation combinations. For example, pyrrolidinium-based ionic liquids usually own larger ESPWs while imidazolium-based ionic liquids have better ionic conductivity.[23, 59] As mentioned previously, an EECS system with organic electrolyte (*e.g.,* ACN and PC) normally have a voltage limitation of 2.5 − 2.8 V. A voltage exceeding this value may cause the degradation to electrode materials as well as electrolytes themselves. But, through the combination of pyrrolidinium cation, the ionic liquid electrolyte can withstand an operation voltage of 3 V.[60, 61] With respect to imidazolium-based ionic liquid, i.e. [EMIM][BF_4]

electrolyte, a higher conductivity of 14 mS cm^{-1} at 25°C has been achieved among all ionic liquid-based electrolytes. However, this value is still lower than organic electrolytes, such as $TEABF_4$ /ACN with a conductivity of 59.9 mS cm^{-1} at 25°C.[17] The relatively low conductivity values of ionic liquid electrolyte come from two reasons: (1) high viscosity. The high viscosity of ionic liquid electrolyte will largely affect the ion mobility level thereby significantly decrease the conductivity value. Theoretically, the viscosity value is much lower than that of organic electrolyte. For example, the viscosity of [EMIM][BF_4] and [BMIM][BF_4] are 41 cp and 219 cp,[62, 63] respectively, whereas the viscosity for ACN organic electrolyte is much smaller as 0.3 cp.[64] (2) aggregation. Some cations of ionic liquid are similar to surfactants. Because of the special structure as surfactants, the cations tend to aggregate in ionic liquid, which is a critical problem for ion mobility.[65, 66] Therefore, the ionic liquid electrolyte usually cannot obtain the promising conductivity values as organic electrolyte.

The combination of ionic liquid with organic solvent could be an alternative strategy to draw the advantages of both to create an ionic-liquid-based electrolyte with lower viscosity, thus boosting higher ion mobility. Therefore, the mixture of ionic liquid with organic solvent usually exhibits superior ionic conductivity than solely ionic liquid electrolyte itself. For example, the mixture electrolyte of 2 M [EMIM][PF6] and EC-DMC organic solvent has a conductivity as high as 27 mS cm^{-1}, which demonstrates its superiority than solely ionic liquid [EMIM][BF4] electrolyte with a conductivity of 14 mS cm^{-1} at 25°C.[67] However, not all combinations of ionic liquid with organic solvent could prove to be beneficial to EECS system. More attention should be paid to the drawbacks

brought from the mixture of both.

1.6 Solid-state Electrolyte

Nowadays, we are moving towards a next-generation electrochemical energy period with the demand of flexible electronics, wearable electronics, portable devices, stretchable electronic displays, and so on. However, in these new smart applications, their merits are largely limited by the bulky battery configurations, as a result of relying on liquid electrolytes. To end this, one approach is to swap liquid electrolyte for versatile, solid-state alternatives, making the EECS systems safer, lighter, and more portable.

As a promising solid-state electrolyte, it is expected to be processed with the following characteristics: (1) high ionic conductivity. For a solid electrolyte material, the primary property of interest is the ionic conductivity. However, the ionic conductivity mechanism is still not that clear because of various matrix material as well as complex charge carriers. It is commonly acknowledged that ion mobility and ion concentration are two important factors to contribute to an ideal ionic conductivity value. The high ion concentration will provide a large number of charge carriers, while a good ion mobility guarantees a “free” movement of these charge ions; (2) good dimensional stability and mechanical property. The swelling ratio (dimensional stability) of solid electrolyte is an important indicator to evaluate the electrolyte membrane performance. As a promising solid membrane, a low swelling ratio without the sensitivity of water molecules will be an ideal property, thus the solid membrane will not suffer from shape change with the fluctuation of the humidity environment. Also, a solid membrane with good tensile strength

and strain will be beneficial to the requirement of some stretchable, flexible, wearable electronic devices. (3) excellent thermal, chemical, electrochemical stability. An electrochemical energy system often suffers from an extremely acidic or alkaline operating environment. For example, the common-used electrolyte for zinc air battery is 20 − 40% high concentrated KOH solution.[37] Therefore, a solid electrolyte membrane without any degradation in harsh environment is a guarantee for smoothly running of an electrochemical energy system.

With the rapid growth of solid-state electrolyte development, it can be roughly divided into two major types: quasi-solid-state electrolyte and all-solid-state electrolyte. The following sections will provide detailed discussion for these two electrolytes respectively.

1.6.1 Quasi-solid-state Electrolyte

Currently, gel polymer electrolyte (GPE) is the most extensively studied electrolyte, which is also be called as quasi-solid-state electrolyte due to the presence of a liquid phase in it. [68-70] As shown in **Figure 1-5a**, the GPE is usually composed of a host polymer and a liquid electrolyte or a conductive salt dissolved in a liquid solvent. The host polymer can serve as the three-dimensional network to trap the liquid phase into the polymer matrix. Various polymer matrices have been explored as polymer hosts for preparing GPEs, including poly(ethylene oxide) (PEO), poly(vinylidene fluoride) (PVDF), poly(vinylidene fluoride-hexafluoropropylene) (PVDF-HFP), poly(methyl methacrylate) (PMMA), poly(vinyl chloride) (PVC), poly(vinyl alcohol) (PVA), poly(acrylic acid) (PAA), poly(acrylonitrile) (PAN), poly(ethyl methacrylate) (PEMA), poly(ε-caprolactone) (PCL),

chitosan, and so on.

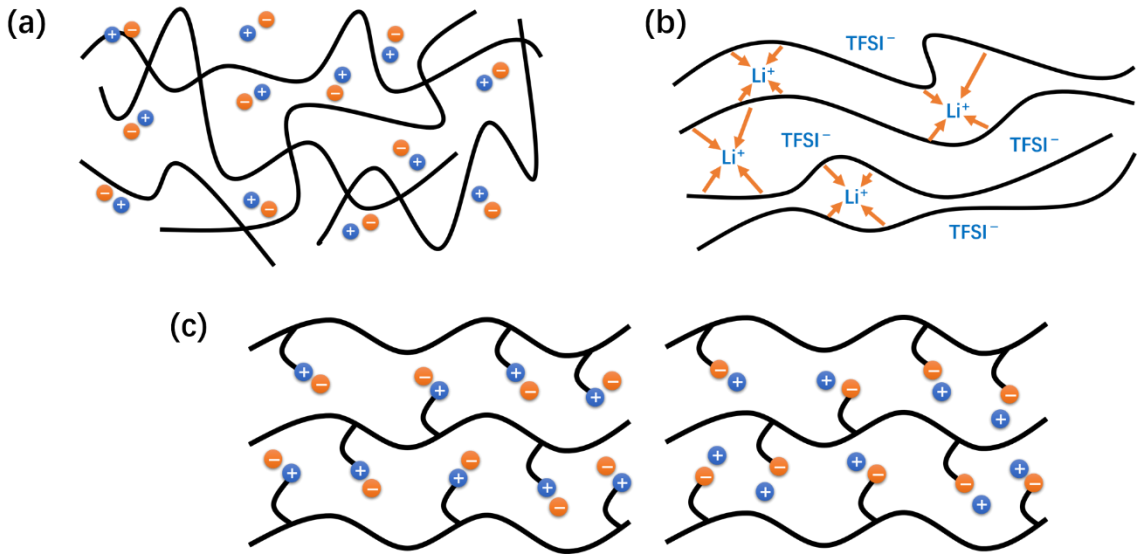

Figure 1-5. Schematic diagrams of (a) a gel polymer electrolyte, (b) a dry solid polymer electrolyte, and (c) a polyelectrolyte.

In this thesis, based on the difference of liquid phases, the GPE will be classified into three types: hydrogel polymer electrolyte, organogel polymer electrolyte and ionogel polymer electrolyte. Hydrogel polymer electrolyte is a GPE which uses water as a plasticizer. For example, PVA is the most popular hydrogel polymer host which can be prepared with a series of H_2SO_4, H_3PO_4, KOH, NaOH, KCl and NaCl.[71, 72] Chen *et al.* reported a thin-film, flexible, and rechargeable zinc-air battery with a PVA-gelled electrolyte which is synthesized from a mixture of KOH/PVA (35/2 wt%) solution.[73] If an organic solvent is applied instead of water, the GPE can be named as organogel polymer electrolyte. Same with the organic liquid electrolyte we discussed above, the organogel polymer electrolyte normally can be operated in an increased battery voltage up to 2.5 − 3 V,[74-78] which is much higher than that of hydrogel polymer electrolyte. Ionic liquid can also

be considered to incorporate into polymer matrices, obtaining a new type of GPE called as ionogel polymer electrolyte. The conductivity and operating voltage of ionogel polymer electrolyte mainly depend on the nature of ionic liquid employed in the system as well as the property of polymer host applied.

Overall, the conductivity of GPE is outstanding among all the solid-state electrolyte because of the present of liquid phase, which provides a freer and easier moving pathway for the ions rather than the blocked solid-state phase. However, GPEs also have their own drawbacks, such as the poor mechanical strength and drying out issue particularly when water is used as the solvent.

1.6.2 All-solid-state Electrolyte

In this thesis, all-solid-state electrolytes are divided into three types: solid polymer electrolyte (SPE), polyelectrolyte and inorganic solid-state electrolyte. As shown in **Figure 1-5b**, SPE is a solvent-free system which consists of a polymer host and a salt without any liquid phase. The conductivity of SPE is not as high as the GPE system, because the ions move across the polymer without any assist of water or organic solvent. PEO is the most common-used polymer particularly in lithium-based batteries, including lithium ion battery and lithium sulfur battery. In the polyelectrolyte, the ionic conductivity contributes from the charged polymer chains. As shown in **Figure 1-5c**, the anions can move through polycations-type electrolyte chains, whereas the cation conducting property can be achieved by the polyanions-type electrolyte. Inorganic solid-state electrolyte is an all-solid-state phase composed of inorganic materials, such as Li_2S–P_2S_5 glass-ceramic electrolyte reported by Francisco *et al*.[79] Unlike polymer-based solid electrolyte, inorganic solid-state

electrolyte is not able to be flexible, bendable and stretchable. The interfacial contact of inorganic solid-state electrolyte is also a big issue. However, it usually has good thermal stability and robust mechanical property, thus it can be operated in high temperature up to 150 − 200 ^{o}C.[80, 81]

1.7 Structure of Thesis

The main objectives of this thesis are to i) design high-performance electrolyte materials for electrochemical energy systems, ii) understand the ion transportation mechanisms behind different electrolyte materials, and iii) contribute to the development of next-generation electrochemical energy systems with the demonstration of flexible and bendable electronic devices. Therefore, in this thesis work, the design and characterization of different electrolyte materials were investigated; their relevant physical, chemical and electrochemical properties were optimized respectively, then combined to fabricate different EECS systems. **Figure 1-6** depicts a breakdown of work conducted throughout this thesis.

This thesis is organized in six chapters. **Chapter 1** introduces readers a general background, motivation, classification of current electrolytes for electrochemical systems, and the scope of the thesis work. **Chapter 2** presents some key performance measurement techniques employed throughout the thesis, with in depth details provided within subsequent chapter 3 through 5. Three different tasks that have been published are discussed in subsequent chapter 3-5. **Chapter 3** focuses on a novel strategy of tuning the pH of the electrolyte environment to enhance the battery voltage, and eventually achieve

the goal of high energy density for all-aqueous redox flow batteries. **Chapter 4** deals with a functionalized nanocellulose/graphene oxide membrane with a laminated structure to be used as a hydroxide-conducting solid-state electrolyte in flexible and rechargeable zinc-air batteries. **Chapter 5** describes a co-functionalized cellulose/graphene oxide proton-conducting solid electrolyte with a 3D interpenetrating network structure. The solid electrolyte has successfully to be applied in a fuel cell gas sensor for the detection of alcohol. **Chapter 6** summarizes the important results and some discussions on the future direction that the work may take.

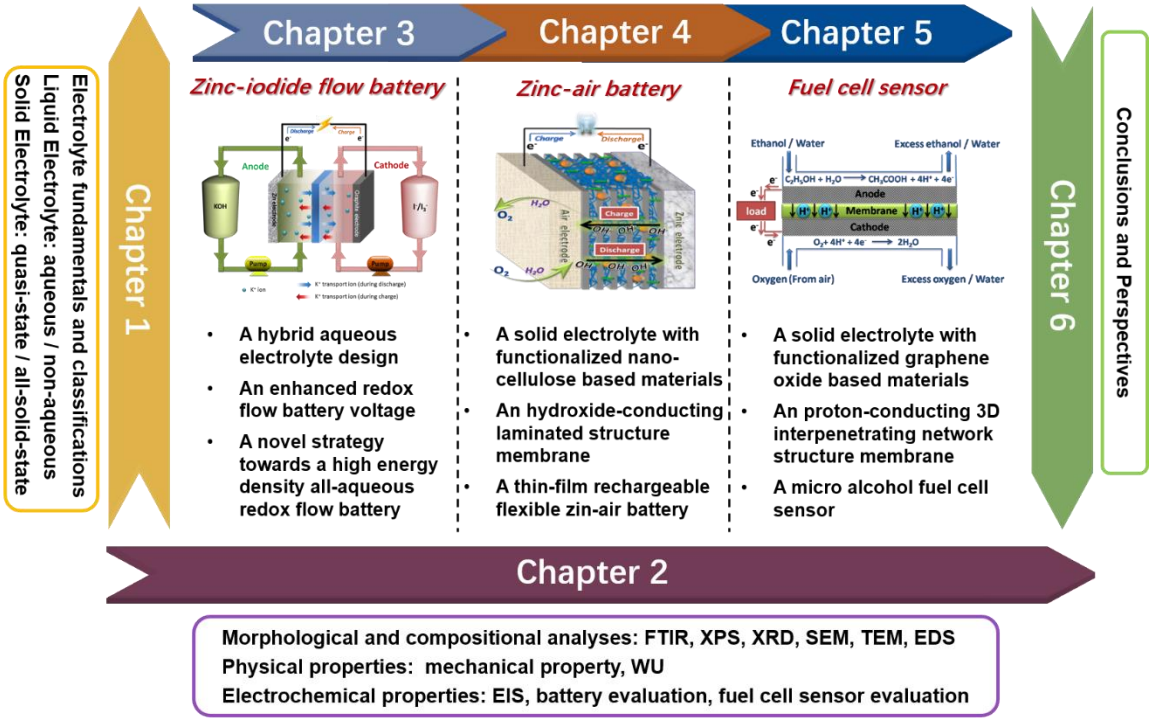

Figure 1-6. Schematic illustration of the research topics throughout this thesis.

Chapter 2 Characterization Techniques

This chapter presents some key performance measurement techniques related to the evaluation of materials and systems developed in this work. In this thesis, the morphological and compositional analyses as well as physical properties are applied to extensively characterize the nanocomposite electrolyte membranes synthesized in this work. A variety of electrochemical techniques are applied to evaluate the performance of electrochemical systems, including zinc iodide battery, zinc air battery and fuel cell sensor. The detailed experimental procedures, characterization and evaluation of each developed materials are provided within the proceeding chapters.

2.1 Morphological and Compositional Analyses

2.1.1 Fourier Transform Infrared (FT-IR) Spectroscopy

FT-IR spectroscopy[82, 83] is a very common-used method to recognize the molecular structures of organic compounds, mainly because it delivers significant amount of information and is fairly inexpensive and easy to perform. Advantages of FT-IR spectroscopy include:

(i) better signal-to-noise ratios;

(ii) the ability to record complete spectra in much shortest timescales.

Basically, the useful parts of the infrared (IR) region for the analysis of polymeric materials have a wavelength ranging from 2500 to 16000 nm. The related photon energies of this range of the IR are not big enough to excite electrons; yet, they are able to cause vibrational excitation of covalently bonded atoms and groups which can be stretched and

bent. The characteristic of organic compounds is that they can go through a broad variety of vibrational motions of their constituent atoms, resulting in the absorbance of IR radiation related to the energy of the corresponding component vibration. Consequently, the existing bonds and functional groups in the polymer can be identified by comparing the absorptions positions in the IR spectrum with the characteristic absorption regions. In this study, the synthesized polymer matrix is examined by FT-IR to generally identify the molecular structure.

2.1.2 X-Ray Photoelectron Spectroscopy (XPS)

XPS,[84, 85] also recognized as electron spectroscopy for chemical analysis (ESCA), is a prevalent characterization tool for the investigation of elemental composition and chemical state. In principle, X-rays with known energy irradiate on analyte, causing emission of electrons by photoelectric effect and the kinetic energy and number of electrons that escape from the material's surface (top 1 to 10 nm) are detected and analyzed based on the electron binding energy. The binding energy spectrum versus the number of electrons can directly identify the elements on the surface of the material and provide the relative amounts of each element. In this thesis, XPS is mainly utilized to identify and quantify the elements in the developed solid-state electrolyte. Moreover, in many cases also the different chemical states of the elements can be distinguished.

2.1.3 X-Ray Diffraction (XRD)

XRD [86, 87] is a versatile characterization technique which allows the determination of crystal structure and atomic spacing. The X-rays from the source interact with the sample to produce diffraction patterns at the angles corresponding to specific crystal planes.

The x-ray source is swept over a range of angles and the diffracted x-rays at specific angles are collected, processed and counted by the detector. The angle of diffraction is related to the specific crystal orientation of the sample by Bragg's law as shown by Equation 2-1 below,

$$n\lambda = 2d\sin\theta \quad (2\text{-}1)$$

where n, λ, d, and θ represent the order of the spectrum (any integer), the wavelength of the X-rays, the spacing between diffracting planes, and the incident angle, respectively. The diffraction pattern at specific angles obtained by XRD can be compared to the theoretical diffraction pattern calculated by the crystal planes to help identify the material. Having said this, XRD patterns cannot be produced by amorphous materials as they do not have ordered crystal planes that interact with X-rays to produce diffracted patterns. In this thesis, XRD is used to identify the developed solid-state electrolytes and confirm their crystal structures.

2.1.4 Scanning Electron Microscopy (SEM)

SEM[88] is a powerful imaging tool used to investigate morphology and topological features of micro and nanostructured materials. It involves illuminating the sample with a powerful beam of electrons, and projecting images based on collected secondary or backscattered electrons. The image resolution is similar to the size of the utilized electron beam and can be on a nanometer or micrometer scale. In the thesis, SEM will be utilized to investigate the distinct nanostructures of the fabricated materials.

2.1.5 Transmission Electron Microscopy (TEM)

TEM[89] is one of the essential physical characterization techniques, which allows

direct visualization of the sample's morphology similar to SEM. TEM also utilizes an electron beam as the source to create high resolution images. However, unlike in SEM which detects backscattered or reflected electrons above the sample, TEM detects electrons which are transmitted through a thin sample which are then converted to an electric signal to produce the final image. This allows TEM to resolve features in the atomic range including the visualization of crystal orientation in ordered metal or transition metal oxide samples.

2.1.6 Energy dispersive x-ray spectroscopy (EDS)

EDS or EDX[90, 91] is an elemental analysis technique which allows identification and quantification of the sample's chemical composition. This technique is commonly coupled to an SEM or TEM system to be conducted simultaneously with microscopic analysis. The EDS signal is obtained by detecting x-rays emitted from the sample during the interaction with the electron beam. The fluorescence X-rays of the emitted x-ray is specific to each element which provides blue print for elemental identification. A typical EDS result is displayed as a spectrum with x-ray counts versus fluorescence X-rays to show various elements found in the sample. The EDS can also be used to create elemental "maps", which shows the distribution of localized elements over a selected area of the sample. The maps show varying intensities depending on the amount of the localized elements. This is particularly interesting for hybrid catalysts consisting of organic and inorganic constituents to clearly identify the elements and their distribution in a sample.

2.2 Physical Properties

2.2.1 Mechanical Property

Polymeric materials and polymer-based composites are often thought of as being mechanically weak compared with metals and ceramics. However, these days many polymer-based composites are used in structural engineering applications and are subjected to appreciable stresses. The mechanical properties of these materials have consequently been somewhat taken seriously nowadays.[92, 93]

There are a bewildering number of mechanical tests and testing instruments. In this thesis, stress-strain tests are built up to measure the deformation of a specimen as the force is applied at a constant rate. Stress-strain curves are an extremely important graphical measure of a material's mechanical properties. The slope of the straight-line of the curve is the elastic modulus of the material. In a tensile test this modulus is Young's modulus E.

$$\text{Stress} = \frac{\text{force of load F}}{\text{cross-sectional area A}} \tag{2-2}$$

$$\text{Strain} = \frac{L - L_0}{L_0} \tag{2-3}$$

$$\text{Young's modulus E} = \frac{\text{Stress}}{\text{Strain}} \tag{2-4}$$

where L_0 is the original length of the specimen and L is the stretched length.

2.2.2 Water Uptake (WU)

WU[94, 95] is a measurement which exhibits the capability of an ion conductive electrolyte membrane to retain the water. The WU of membrane has a great influence on the membrane's mechanical properties as well as ionic conductivity. Increased hydration of membrane facilitates WU property, thus inducing an enhanced ion conductivity value.

To calculate WU, the desired membrane is firstly immersed into deionized water at room temperature for 24 hrs to insure saturation. Then the saturated membrane is taken out and weighed immediately after the remove of water droplets from the surface. After that, the membrane is vacuum dried at 80 °C for 24 hrs. The dried membrane is weighed immediately in a plastic sealing bag. The WU can be determined from the following:

$$WU\ (\%) = \frac{W_{wet} - W_{dry}}{W_{dry}} \times 100 \qquad (2\text{-}5)$$

where WU (%), W_{wet} and W_{dry} are the water uptake by weight percentage, the weight of wet membrane and the weight of dry membrane respectively.

2.2.3 Thermal Gravimetric Analysis (TGA)

TGA[96, 97] is a continuous process to study the thermal degradation of polymeric materials and polymer-based composites. TGA involves the measurement of sample weight as the reaction temperature is changed by means of a programmed rate of heating. Mass is lost if the substance contains a volatile fraction. Thus, the sample weight decreases slowly as reaction begins, then drops rapidly over a comparatively narrow temperature range, and finally levels off as the reactant becomes spent.

2.3 Electrochemical Properties

2.3.1 Ionic Conductivity Measure via Electrochemical Impedance Spectroscopy (EIS)

The accurate measurement of ionic conductivity through the electrolyte membrane is of prime significance for the characterization of electrolyte materials. The conductivity property can be evaluated through the measurement of resistivity of the conductive membrane against the flow of alternating current (AC), which is known as AC impedance

method. The AC impedance method can be classified into the two-terminal and four-terminal methods. The four-terminal method is suggested to be applied to measure the resistivity of ion conductors with low resistance, which has already eliminated interference of interfacial resistance and polarization. The two-terminal method is usually used to measure the resistivity in material of high resistance (above 10 kΩ) as the contributions of other interferences are low enough to be neglected in the total resistance. Thus, in this thesis, all the conductivity testing is conducted through four-terminal AC impedance spectroscopic technique for more accurate experimental data. The ion conductivity is calculated using the following equation:

$$\sigma = \frac{L}{A \times R} \tag{2-6}$$

where σ is the ionic conductivity, L is sample length (or distance between the reference electrodes in the membrane), R is the resistance of the membrane, and A is the cross-sectional area of the membrane.[98-100]

Furthermore, the ion conduction behavior of the membrane can be elucidated by the relationship between the conductivity and the temperature derived from the Arrhenius equation below:

$$\ln\sigma = \ln\sigma_0 - \frac{E_a}{RT} \tag{2-7}$$

where Ea is the activation energy for ion conductivity, R is the gas constant, T is the absolute temperature, and σ_0 is the frequency factor.

2.3.2 Battery performance evaluation

This section provides an overview of the variety of experimental testing techniques that may be employed to evaluate the performance of batteries in this work. Factors such

as open-circuit voltage (OCV), operating voltage, power density, energy density, specific capacity, coulombic efficiency, voltage efficiency, energy efficiency as well as cycling stability are essential parameters that should be evaluated in the investigation of zinc iodide battery in Chapter 3 and zinc air battery in Chapter 4. These parameters can be revealed with galvanodynamic polarization and galvanostatic techniques, including galvanostatic full-discharge and galvanostatic cycling.

2.3.2.1 Galvanodynamic polarization

The galvanodynamic polarization technique is used to evaluate the degree of departure of a battery's operating voltage from its OCV in response to discharging and charging currents. It is usually carried out by applying negative (discharging) or positive (charging) currents with progressively higher magnitudes to the battery electrodes. The responding potentials are recorded as a function of applied current, yielding discharge and charge polarization curves. The difference between the operating voltage and the OCV (i.e., discharge or charge overpotential) directly represents the sum of the voltage losses associated with activation and mass-transfer polarization at each electrode, as well as the ohmic resistance of each component of the electrochemical circuit. In the study of electrolyte, we place more importance on the region of ohmic loss, which mostly comes from the internal resistance of the electrolyte to ionic flow and the interfacial resistances between the electrodes and electrolyte. The power density of the battery can be plotted as a function of current density by multiplying the discharge voltage by the applied current density, producing the power density and the corresponding current density.

2.3.2.2 Galvanostatic full-discharge and cycling

The capacity of battery can be determined through galvanostatic full-discharge technique by applying a fixed discharge current until a defined cut-off voltage is reached. The capacity of battery is often normalized by the mass of electrode or the mass of the whole battery. An extremely flat full-discharge curve indicates little ohmic polarization of the battery. Galvanostatic cycling is an accelerated testing technique for investigating the electrochemical durability of batteries. Through galvanostatic discharge/charge cycling, the responded discharge and charge voltages are recorded as a function of alternately fixed negative (discharge) and positive (charge) currents. In comparison to galvanodynamic polarization testing, the galvanostatic cycling test involves the choice of more test conditions, including discharge/charge current density, the number of cycles, as well as the time length and cut-off voltage for each cycle. All of these parameters will affect the test results.

2.3.3 Fuel cell sensor performance evaluation

The fuel cell sensor performance can be evaluated by application of membrane electrode assembly (MEA) with a series of electrolyte membranes. The MEA is fabricated by sandwiching the as-prepared membranes with commercial gas diffusion electrode (GDE) (Fuel Cells Etc.). Then, the MEA is punched into desired size and assembled into sensor housing with two Pt wires as current collectors. Before testing, the sensor housing with MEA assembled is stabled in the humidity chamber with 25 °C and room humidity 60% for 72 h to equilibrate the components with the desired condition. The resulting sensor housing is then inserted into the testing device to evaluate the performance. A certain concentration of ethanol standard solution is prepared and warmed up in the simulator, and

the ethanol vapor is generated by purging the air with a fixed flow rate. The fuel cell sensor is initiated by pumping in the desired volume of gas into the sensor housing. Then, the response curves, including the parameters of peak height, peak area, response time and recover time, are recorded by a digital multimeter. Each sample was repeated five times and the average of each parameter was taken into account.

Chapter 3 An All-Aqueous Electrolyte Redox Flow Battery with Unprecedented Energy Density

3.1 Introduction

In order to meet the soaring worldwide energy demand, various renewable energy resources are integrated into today's electrical grids, such as wind power and solar energy. However, these renewable power outputs are usually unstable and inconsistent due to their fluctuation along with the change of weather or location.[101-103] Thus, a great need for advanced energy storage systems to mitigate undulating outputs and stabilize power grids is looming. Redox flow batteries (RFBs) are of particular interest because of the flexible power and energy storage originating from their unique architecture.[104-106] In contrast to capsule-enclosed batteries, RFBs store electrolyte with redox-active materials in external reservoirs.[107-109] The redox reactions occur instantly on the electrodes' active surfaces when liquid electrolyte is flowing into the cell. Therefore, the battery capacity can be increased up to the megawatt-hour (MWh) range by simply expanding the volume of reservoir.[110, 111]

Among various RFB systems, all-vanadium redox flow battery is recognized as one of the most promising commercialized candidates benefitting from its long cycle life, high efficiency as well as excellent electrochemical reversibility. However, in the soaring high energy demand, its merits are largely limited by the low energy density. With a certain electrolyte volume and concentration, the energy density of a RFB is usually determined by two factors: (1) number of transferred electrons of the redox reaction;[112] (2) flow battery voltage.[113] Thus, enhancing battery voltage could be one very feasible and effective

approach to achieving high energy density.

Inspired by this concept, various non-aqueous RFBs have been put forward with elevated battery voltage because of their wide electrochemical window employing organic solvents.[114-121] Non-aqueous lithium-RFBs are typical illustrations with elevated battery voltage (>2.0 V), which subtly combine lithium-ion or lithium-sulfur batteries with flow battery technology.[115, 118, 120] However, these non-aqueous lithium-RFBs have their inevitable drawbacks: Firstly, because of the employment of lithium metal, they are very sensitive to moisture as well as the gas of O_2, N_2, CO_2 in the air.[114, 116] Secondly, ionic mobility in non-aqueous solutions is much slower than in their aqueous counterpart.[6] Lastly, most of the non-aqueous lithium-RFBs are based on the size of coin-cell with a volume of electrolyte less than 5 ml, and has incapability for scaling-up. Alternatively, semi-aqueous lithium-RFBs were proposed by using a completely ionized aqueous redox-active species in the aqueous catholyte to match up with a non-aqueous lithium anode.[122-125] They demonstrate high energy densities as well as long cycle lives, benefitting from the unique battery structure which possesses the advantages of both aqueous and non-aqueous RFBs. However, owing to this specific battery configuration, a fragile and costly crack-free glass ceramic membrane must be assembled to eliminate organic/aqueous electrolyte cross-over issues, the manufacture of which will largely limit the scalability and increase the cost of flow batteries.[122, 125] Also, the resistance of ceramic membrane is usually high, thus making the semi-aqueous RFBs cannot discharge at a very high current density. Therefore, non-aqueous and semi-aqueous RFBs are far from commercialization, while all-aqueous RFBs are still irreplaceable.[126] By introducing the concept of middle electrolyte, a multiple ion-

exchange membrane design for all-aqueous RFBs has been put forward, which creates the flexibility to allow new electrolyte combinations and gives a promising potential of high energy density for an all-aqueous RFB system.[127] However, this complex battery structure also brings new challenges to commercial scalability including electrolyte leakage and membrane fabrication.

The pursuit of high energy densities for all-aqueous RFBs has met the bottleneck period until early in 2015, Li et al. reported a promising high energy density (167 Wh l^{-1}) zinc-polyiodide all-aqueous flow battery, which is approaching the energy density of low-end lithium-ion batteries, successfully demonstrating a bright future for all-aqueous high energy density RFB systems.[30] Further improvement of all-aqueous RFBs performance is still burgeoning in these years. But little effort has been expended on the methodology of enhancing battery voltage to improve the energy capacity of all-aqueous RFBs. This is because in theory, the high battery voltage is not attainable in aqueous electrolytes owing to the narrow water electrolysis potential window of 1.23 V.[125] However, considering kinetic, the practical water splitting potential is usually above 2 V because of the high over-potential of hydrogen/oxygen evolution reaction at electrode surfaces.[31] If the low hydrogen evolution potential in alkaline medium could be combined with the high oxygen evolution potential in acid medium in one system, the battery could achieve a stable cell potential window even as high as ~ 3V.[113] Thus, the water electrolysis reaction is not the restraining factor in aqueous solution if the battery can be designed and fabricated properly. Then, the next logical question is how to enhance the voltage of all-aqueous RFBs. According to the pourbaix diagram, the pH value of aqueous electrolyte has a great

influence on the redox potential of electrode candidates.[33] By carefully observing the redox potential table, we can find that some redox potentials of metal pairs exhibit a huge difference between acid and alkaline environments. For example, a zinc redox potential of -0.763 V (Zn2+/Zn) versus standard hydrogen electrode (SHE) is obtained in acid electrolyte (Equation 3-1),[30] whereas a redox potential of -1.260 V ($Zn(OH)_4^{2-}$/Zn) versus SHE is gained in alkaline solution (Equation 3-2).[37]

In acid: $Zn^{2+} + 2e^- \rightarrow Zn$ E^0=−0.763 V (3-1)

In alkaline: $Zn(OH)_4^{2-} + 2e^- \rightarrow Zn + 4OH^-$ E^0=−1.260 V (3-2)

Therefore, by simply tuning the acid-base environment for this redox pair, the battery voltage will significantly increase (eg. 0.497 V potential enhancement for zinc redox pair from acid and to alkaline electrolyte), which ultimately leads to an enhanced energy density. For the first time, this ingenious design of tuning electrolytic pH value for achieving a high energy density for all-aqueous RFBs is proposed in this work. Simply and effectively, this novel strategy opens a promising route for the development of all-aqueous high-energy-density RFBs.

3.2 Experimental Methods

3.2.1 Battery cell assembly

In anode half-cell, zinc plate with apparent area of 7 cm^2 served as anode and copper foil as current collector. In cathode half-cell, graphite foil with apparent area of 7 cm^2 served as cathode and stainless-steel mesh as current collector. The commercially available cation exchange membrane (Nafion 117, Dupont, USA) was used as the separator to be sandwiched between two half cells. First, the Nafion 117 membranes were treated with 3% H_2O_2 under 100°C for 1 h and then washed with deionized water at 100°C for 1 h. Secondly, the Nafion 117 membranes were transferred into 0.5 M H_2SO_4 at 100°C for 1 h and then washed with deionized water at 100°C for 1 h. Lastly, the Nafion 117 membranes were treated with 1 M KOH at 100°C for 1 h to change the membrane into K^+ conductive membrane. The original catholytes with different concentrations were prepared by dissolving appropriate potassium iodide (KI, ≥ 99%, Aldrich) with iodine (I_2, ≥ 99%, Aldrich) in deionized water. The volume of catholyte was designed to be 10 ml for each cathode half-cell. The original anolytes were prepared with corresponding concentration of potassium hydroxide (KOH, ≥ 85%) for balanced osmolarity. The single cell was assembled as shown in **Figure 3-1**.

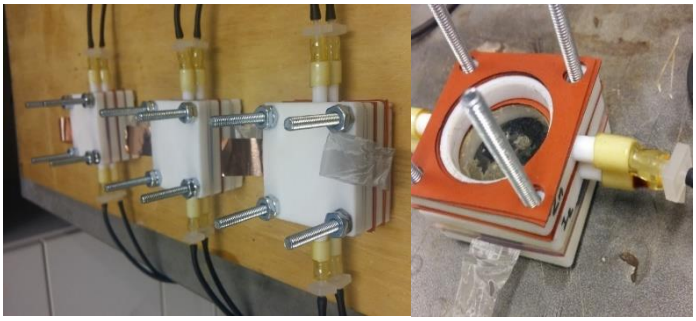

Figure 3-1. Photographs of the hybrid alkaline Zn-I_2 flow battery cell configuration.

3.2.2 Characterization and electrochemical measurements

The cyclic voltammogram test was conducted in a three-electrode cell using a CHI660C workstation (CH Instruments, USA). A graphite rod, glassy carbon and Ag/AgCl (filled with 3M KCl) electrode were used as the counter, working and reference electrodes, respectively. Testing was performed in 0.1 M zinc acetate (ZnAc) with 3M KOH solution to determine the potentials of the $Zn(OH)_4^{2-}/Zn$ redox pair, and in 0.1M KI electrolyte to determine the potentials of the I_3^-/I^- redox pair. Discharge and charge cycling were carried out by a recurrent galvanic pulse method at different current density. The morphology of the membrane was imaged by SEM (LEO FESEM 1530).

3.2.3 Permeability measurements.

Permeability of ions through Nafion 117 was investigated in a membrane separated diffusion cell. All the membranes were activated to K^+ ion conductor with an effective area of 2.54 cm^2 and a thickness of 170 mm. The solution volume of each half-cell was 250 mL. The left compartment was filled with saturated Zn^{2+} ions in 2M and 4M KOH solutions, respectively. The right compartment was filled with 2M and 4M KI solutions, respectively. To detect the zincate ions that were diffused during the permeability test, the permeate solution (0.5 mL) was collected every hour and then diluted and acidified with diluted mixed acid solution of 0.45 mol L^{-1} HCl and 0.2 mol L^{-1} HNO_3. Zincate ions were transformed into zinc ion during this process. After the volume was fixed at 25 mL, the sample solutions at different diffusion time were ready for the zinc determination via ICP-OES (Perkin Elmer Ltd., USA). According to the standard line created by the commercial standard zinc ion solutions, the zinc ion concentration in each acidic diluted solution was

obtained. The permeability coefficient can be calculated by the following equation:

$$V_{\mathrm{R}} \frac{\mathrm{d}c_{\mathrm{R}}(t)}{\mathrm{d}t} = \mathrm{A}\frac{P}{L}[c_{\mathrm{L}} - c_{\mathrm{R}}(t)] \quad (3\text{-}3)$$

Where P is the ion permeability coefficient ($cm^2\ min^{-1}$). L is the membrane thickness (μm), A is the effective area of the membrane (cm^2), C_L and C_R are the initial concentrations of ions in the left and right compartments (mol L^{-1}), respectively, and V_R is the volume of the solution (mL). Assumption is suggested that P is independent of concentration.

3.3 Results and Discussions

In this study, on the basis of the above consideration, triiodide/iodide (I_3^-/I^-) redox pair is chosen as the cathode reactive species and couples with an alkaline $Zn(OH)_4^{2-}/Zn$ anode to compose a hybrid electrolyte all-aqueous RFB. Equation 3-4 illustrates the redox action of I_3^-/I^- via two-electron transfer. Iodide has been recognized as one of the most promising cathode redox candidates owing to the following reasons. Firstly, benefiting from its high solubility (over 8 mol L^{-1}) in aqueous electrolyte, iodide has the ability to deliver high energy density.[123] Moreover, the suitable I_3^-/I^- redox potential (0.536 V vs SHE) makes it possible to avoid water electrolysis.[128]

$$I_3^- + 2e^- \rightarrow 3I^- \qquad E^0=0.536\ \mathrm{V} \quad (3\text{-}4)$$

$$I_2(s) + I^- \leftrightarrow I_3^- \qquad K=723\pm10 \quad (25^{\circ}C) \quad (3\text{-}5)$$

As in Equation 3-5, I_3^- can be constructed by the addition of solid I_2 into I^- solution (potassium iodide (KI) solution is employed in this work).[124, 129] The solubility of I_2 will dramatically improve with the presence of excess I^-. With the increasing concentration of I_2, other polyiodide species (such as I_5^-, I_7^-, and I_9^-) will also be formed. But, I_3^- is the predominant electroactive species and the only isolated polyiodide that exists in aqueous

solution. During discharge (**Figure 3-2a**), zinc oxidation reaction occurs at the anode in an alkaline potassium hydroxide (KOH) anolyte, yielding soluble zincate ($Zn(OH)_4^{2-}$) ions and liberated electrons. The electrons travel through an external circuit from anode to cathode, producing electricity. I_3^- is reduced into I^- at the cathode once having received the electrons. At the same time K^+ migrates from anode to cathode to complete the reaction. During charge (**Figure 3-2**b), the reverse redox reactions occur at the two electrodes, in which zincate is reduced into zinc deposited onto the anode, while I^- is oxidized back to I_3^- at the cathode. Meanwhile, K^+ travels through the membrane from cathode to anode. The overall working principle of the proposed alkaline anolyte Zn-I_2 RFB can be described as follows:

$$\text{Anode: } Zn(OH)_4^{2-} + 2e^- \rightarrow Zn + 4OH^- \qquad E^0=-1.260\ V \qquad (3\text{-}6)$$

$$\text{Cathode: } I_3^- + 2e^- \rightarrow 3I^- \qquad E^0=0.536\ V \qquad (3\text{-}7)$$

$$\text{Overall: } Zn + I_3^- + 4OH^- \leftrightarrow Zn(OH)_4^{2-} + 3I^- \qquad E^0=1.796\ V \qquad (3\text{-}8)$$

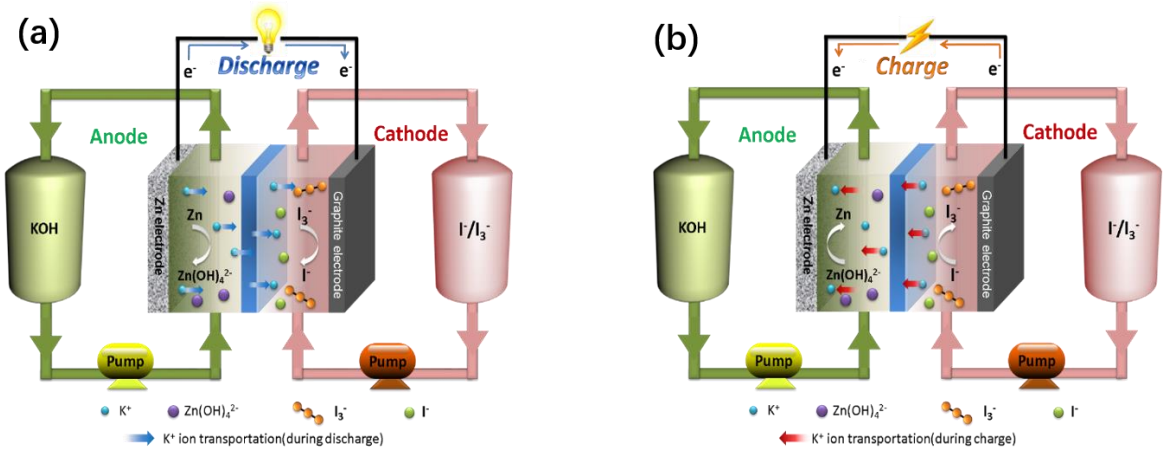

Figure 3-2. Schematic illustration of the working principle of (a) discharge and (b) charge processes of the designed alkaline Zn-I_2 redox flow battery.

Theoretically, this newly-designed alkaline Zn-I_2 RFB outweighs its conventional counterpart by a 0.497 V (**Figure 3-3**) increase in battery voltage and a 38.26% enhancement in energy density, which is a very significant improvement. If we make an assumption that Zn metal is unlimited and the concentration of I_3^- solution is 1 mol/L. Then, the calculation details of energy density enhancement are as follows:

$$Volumetric\ Energy\ Density\ \ (Wh\ L^{-1}) = \frac{F \times c \times n \times OCV}{3600}$$

where F is the Faraday constant 96485 C/mol, n is the number of electrons transferred during reaction per mole reactant, c is the concentration of I_3^- solution, OCV is the battery's nominal voltage.

(1) For conventional Zn-I_2 flow battery

$Zn + I_3^- \leftrightarrow Zn^{2+} + 3I^-$ E=1.299 V

$$Volumetric\ Energy\ Density\ (Wh\ L^{-1}) = \frac{96485 \times 1 \times 2 \times 1.299}{3600} = 69.63\ Wh\ L^{-1}$$

(2) For alkaline Zn-I_2 flow battery

$Zn + I_3^- + 4OH^- \leftrightarrow Zn(OH)_4^{2-} + 3I^-$ E=1.796 V

$$Volumetric\ Energy\ Density\ (Wh\ L^{-1}) = \frac{96485 \times 1 \times 2 \times 1.796}{3600} = 96.27\ Wh\ L^{-1}$$

Therefore, according to the calculation, by converting conventional Zn-I_2 flow battery to alkaline Zn-I_2 flow battery, the theoretical volumetric energy density increases by 38.26%.

$$Volumetric\ Energy\ enhancement\ \ (\%) = \frac{96.27 - 69.63}{69.63} \times 100\% = 38.26\%$$

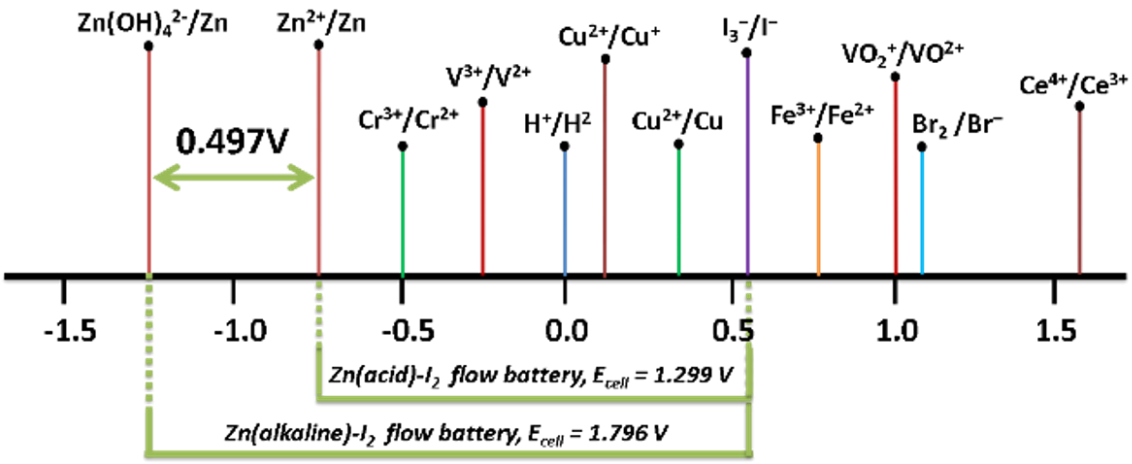

Figure 3-3. The standard redox potentials of various candidate redox pairs suitable for all-aqueous redox flow battery.

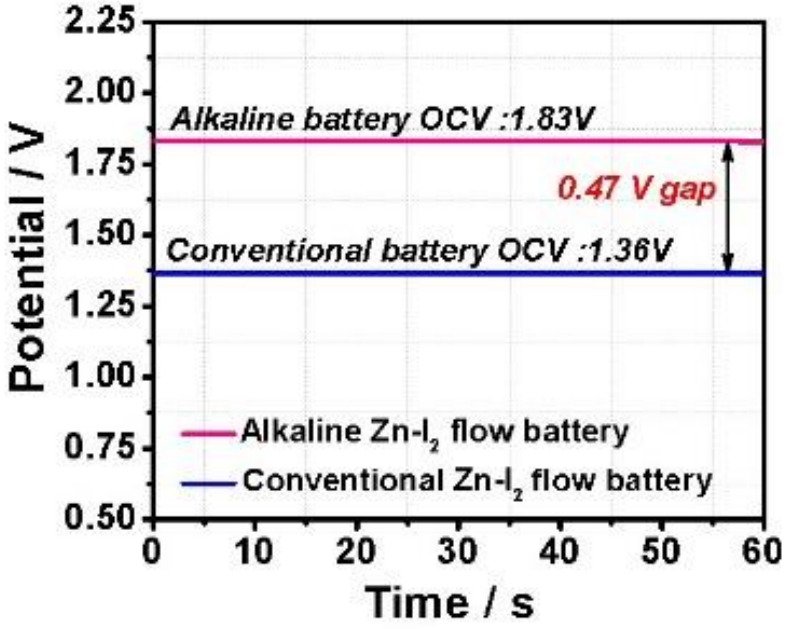

Figure 3-4. The open-circuit-voltage between conventional and designed alkaline Zn-I_2 redox flow battery.

The practical demonstration of open circuit voltage (**Figure 3-4**) also shows a real 0.47 V potential gap existing between the two batteries. In particular, as shown in **Figure 3-5**, cyclic voltammetry (CV) measurements of 0.1 M zinc acetate ($ZnAc_2$) with 3M KOH solution were performed to determine the potentials of the $Zn(OH)_4^{2-}/Zn$ redox pair. A typical voltammogram shape of zinc electrodeposition is illustrated without a hydrogen evolution peak. Also, a cyclic voltammogram of 0.1M KI electrolyte shows the pair of I_3^-/I^- redox reaction with no oxygen evolution reaction being observed throughout the entire scan range. All of these features demonstrate the feasibility and superiority of the alkaline Zn-I_2 RFB.

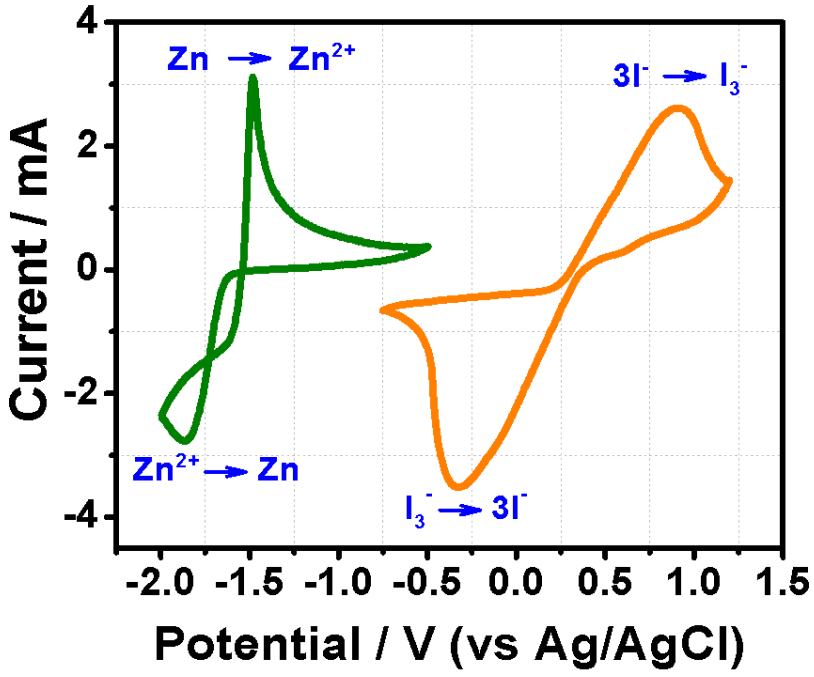

Figure 3-5. Cyclic voltammograms of 0.1 M $ZnAc_2$ with 3 M KOH (green curve) and 0.1 M KI (yellow curve) on a glassy carbon electrode at a scanning rate of 50 mV s^{-1}.

The evaluation of the battery performance was conducted under different current densities (10 ~ 100 mA cm^{-2}). In order to keep the osmolarity balanced, equivalent concentrations of KOH anolyte solution and KI/I_2 catholyte solution were prepared in each external electrolyte reservoir. A polymer membrane (Nafion 117) was assembled between two electrodes to limit the migration of negative ions. As shown in **Figure 3-6**, the battery specific capacity was investigated under a constant current density of 20 mA cm^{-2} as a function of the concentration of KI/I_2 catholyte solution. The high practical specific capacities were successfully obtained from 80.0 (2M) to 193.5 Ah L^{-1}catholyte (6M) with the increase in catholyte concentration. But, these impressive specific capacities are still considerably lower than the theoretical values (**Figure 3-7**).

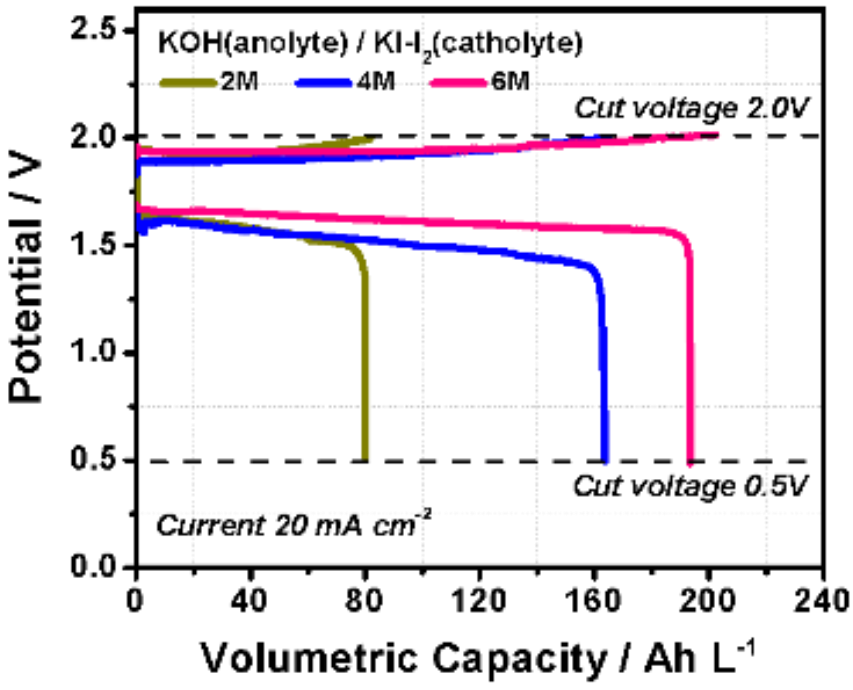

Figure 3-6. Representative galvanostatic charge and discharge curves in different electrolyte concentrations at a current density of 20 mA cm^{-2}.

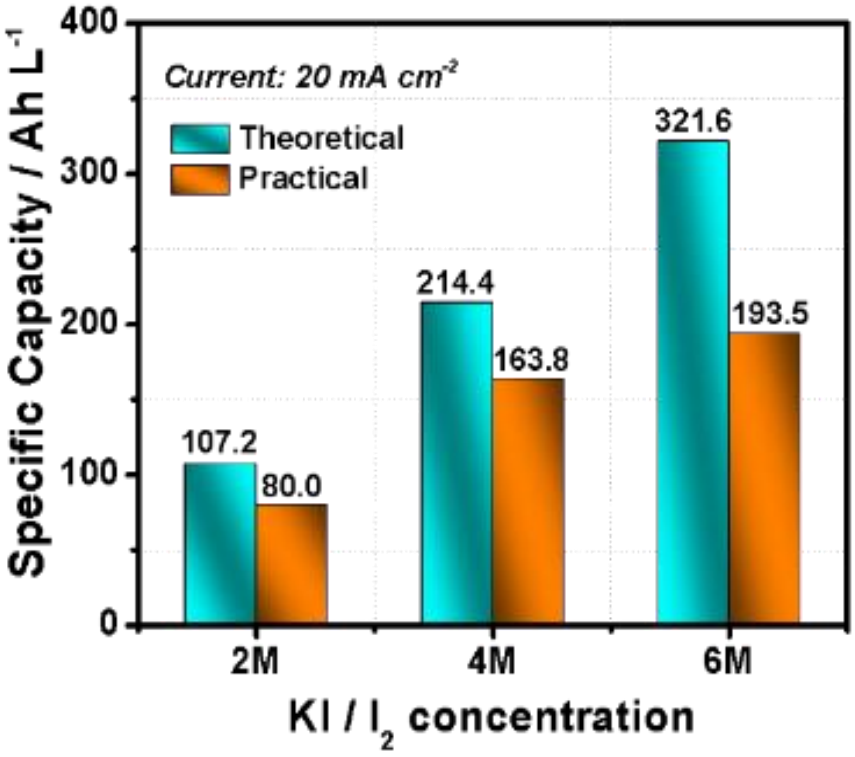

Figure 3-7. The practical specific capacity compared with the theoretical values as a function of the catholyte concentration.

In this work, in order to get the highest energy density, 6M anolyte and catholyte solutions are chosen for the battery cycling test. 10 h charge and discharge times are used for each cycle. The anolyte (KOH solution) volume is 200 mL and the concentration of KOH solution is 6M. The catholyte (KI-I_2 solution) volume is 10 mL and the concentration of KI and I_2 solution is 6M. The discharge current density is 20mA cm^{-2}, and the electrode area is 7 cm^2. Here, we make an assumption to calculate the concentration of zincate ion for the state of charge (SOC) aspect:

The following is the calculation procedure:

(1) The theoretical capacity calculation of the battery

$$Specific\ Capacity\ \ (Ah\ L^{-1}) \ = \frac{F \times c \times n}{3600}$$

where F is the Faraday constant 96485 C/mol, n is the number of electrons transferred during reaction per mole reactant, c is the concentration of I_3^- solution. (1Ah = 3600C)

6M I_3^- concentration: $Specific\ Capacity\ \ (Ah\ L^{-1}) \ = \frac{96485 \times 2 \times 6}{3600} = 321.6\ \ (Ah\ L^{-1})$

The anolyte and zinc reactant are abundant, so the capacity limitation of the battery is the catholyte reactant. The volume of KI-I_2 solution is 10 mL. Therefore, the theoretical capacity of the battery is 3.216 Ah.

(2) The number of electrons produced after 10 h discharge

When the battery discharges for 10h, then 20mA cm^{-2} × 7 cm^2 × 10h = 1.4 Ah electricity released. Because 1Ah = 3600C and 96485C/mol e^-, the amount of e^- produced is 0.0522 mol after 10 h discharge.

(3) The concentration of zincate ions after 10 h discharge

The ratio of zincate and electrons produced in this system is 1:2 ($Zn + 4OH^- \rightarrow Zn(OH)_4^{2-} + 2e^-$), so the amount of zincate ions is 0.0261 mol. The volume of anolyte solution is 200 ml. Therefore, the concentration of zincate ion after 10 h discharge is 0.1305 mol/L.

Based on the calculation above, we make a table in **Table 3-1**.

Table 3-1. Zincate ion concentration as a function of discharge time in 6M anolyte solution.

Discharge hours	0h	1 h	2 h	4 h	6 h	8 h	10 h
Zincate ion concentration	0	0.01305	0.0261	0.0522	0.0783	0.1044	0.1305

Units: mol/L

The loss of capacity comes from the result of three things: (1) Polyiodide formation: As discussed above, I_3^- solution can be achieved by the dissolution of I_2 into KI solution. Ideally, equal amount of I_2 reacts with KI solution, aiming at achieving an equal amount of I_3^- solution. However, in addition to I_3^- ions, some extended polyiodide compounds can also be formed through interactions between fundamental blocks: I_2, I^-, and I_3^-. Therefore, the practical amount of I_3^- ions cannot reach the theoretical value as desired, leading to the loss of capacity compared to the theoretical values. (2) Electrolyte crossover: The cationic exchange Nafion membrane was assembled between anode and cathode to resist the movement of any existing anions $Zn(OH)_4^{2-}$, I_3^-, and I^-, whereas K+ ions as mediator can smoothly shuttle between two electrodes to conduct the charges in the battery. The EDX of Nafion membrane after discharge was investigated on both anode and cathode sides to confirm the elements existing in the membrane (**Table 3-2**).

Table 3-2. The elemental analysis of cycled Nafion 117 membrane on anode and cathode sides obtained from EDX.

	C	O	F	S	K
Anode side	17.51	7.10	61.89	2.87	3.69
Cathode side	14.53	7.02	47.65	1.53	4.37
	Zn	I	Au	Total	
Anode side	1.60	1.52	3.81	100	
Cathode side	12.34	8.73	3.85	100	

Units:wt%

The EDX result illustrates that Zn and I elements are present on both sides of the membrane, indicating that the electrolyte crossover issue exists in this system. The reason can be ascribed to the hydrophilic nature of the membrane. Nafion membrane is a hydrophilic polymer which conducts ions with the assistance of water molecules. Inevitably, a small number of hydrated anions will still pass through the membrane along with water molecules. In order to investigate the electrolyte crossover issue, the permeability of zincate ($Zn(OH)_4^{2-}$) ion was investigated (**Figure 3-8**). Two different concentrations of KOH solution (2M and 6M) were prepared in the left compartment with corresponding concentrations of KI solution in the right compartment to simulate the actual battery conditions conducted. Saturated zincate ($Zn(OH)_4^{2-}$) ion solutions were designed in the left compartment to create maximum ions crossover environments. As shown in **Figure 3-8**, the concentrations of zincate ($Zn(OH)_4^{2-}$) ions in the right compartment increase with the increasing of permeation time in both 2M and 6M KI solutions. The permeability coefficients of zincate ($Zn(OH)_4^{2-}$) ions across Nafion 117 obtained are $6.74\times10^{-7}cm^2min^{-1}$ and 11.62×10^{-7} cm^2 min^{-1} in 2M and 6M prepared electrolytes, respectively. Overall, K^+ ions exist in both reservoirs and can smoothly shuttle between two electrodes to conduct

the charges in the battery. Hydroxide (OH^-) ions in the left reservoirs continuously react with zinc to form a solution of potassium zincate ($Zn(OH)_4^{2-}$).

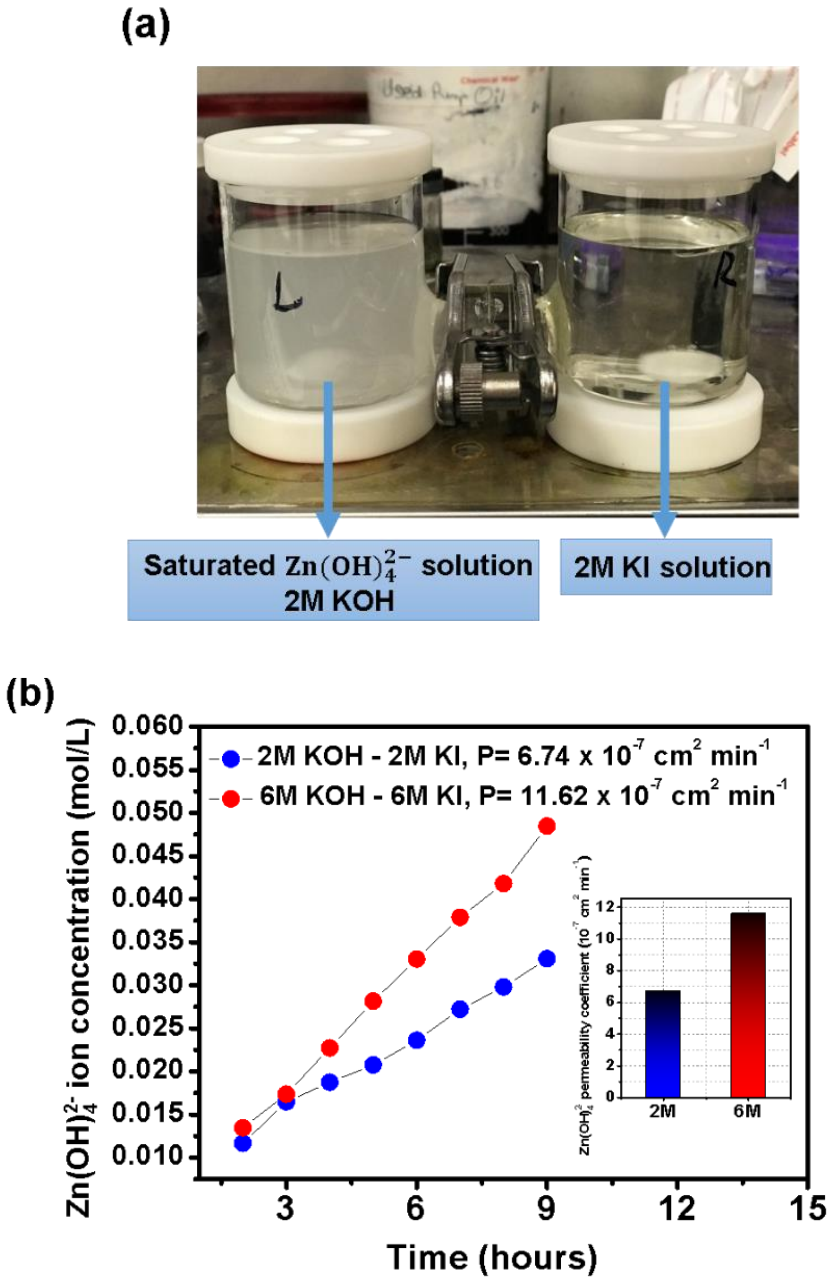

Figure 3-8. (a) The photograph of diffusion cell in simulation of actual battery testing condition. (b) The zincate ion concentration in permeate side with Nafion 117 membrane as a function of time (insert figure: zincate ion permeability coefficients with Nafion 117 membrane in 2M and 6M solution).

For a vanadium redox flow battery (VRFB) system, low vanadium permeability is essential for membrane. Compared with the latest reported VRFB with ultra-low vanadium permeability, the Nafion 117 membrane in our system still exhibits comparable performance with low ion permeability. Overall, the vast majority of anions have been blocked by the Nafion membrane and have reacted in their individual electrolyte reservoir, but still a small amount of undesired hydrated $Zn(OH)_4^{2-}$, I_3^-, and I^- ions were able to go across the membrane, which finally results in the loss of some battery capacity.

(3) Polarization: In this work, graphite foil was used as a current collector for the I_3^-/I^- redox reaction to simply demonstrate the design for this alkaline Zn-I_2 RFB. However, the graphite foil largely limited the battery performance because of its low surface area. Even though it is in the preliminary design stage, the alkaline Zn-I_2 RFB still exhibited distinguished performance.

As shown in **Figure 3-9**, the alkaline Zn-I_2 RFB can run in a wide current density region from 10 to 100 mA cm^{-2}. With the decrease of employed current density, the battery produced more electricity and finally reached a remarkable specific capacity of 202.2 Ah L^{-1} catholyte. Benefiting from the high voltage design of this alkaline Zn-I_2 RFB, the prominent energy density of 330.5 Wh L^{-1} catholyte was achieved at 10 mA cm^{-2}, which is the highest energy density obtained to date in an all-aqueous RFB system to the best of our knowledge. The diagram in **Figure 3-10** exhibits a summary of the performance of various all-aqueous RFBs. With respect to battery potential and energy density, the alkaline Zn-I_2 RFB shows the best performance among all conventional or newly-emerged redox flow batteries.

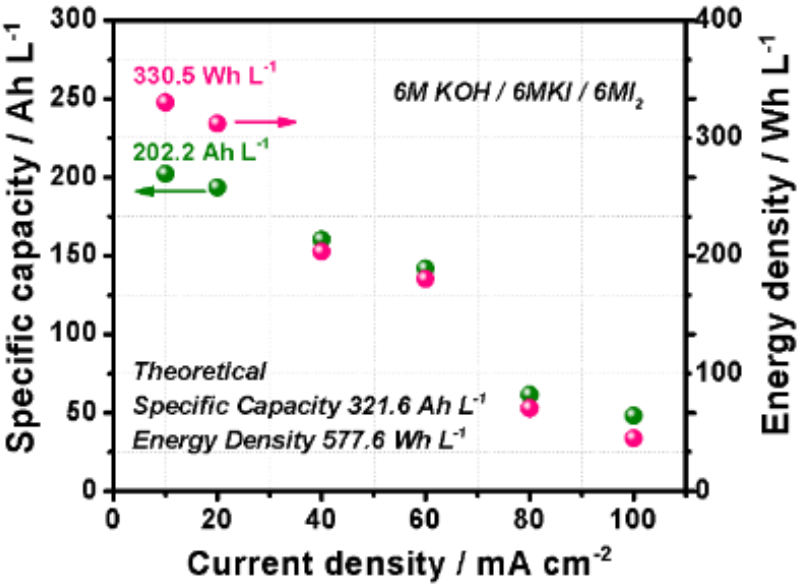

Figure 3-9. Influence of the discharging current density on the achievable specific capacity and energy density.

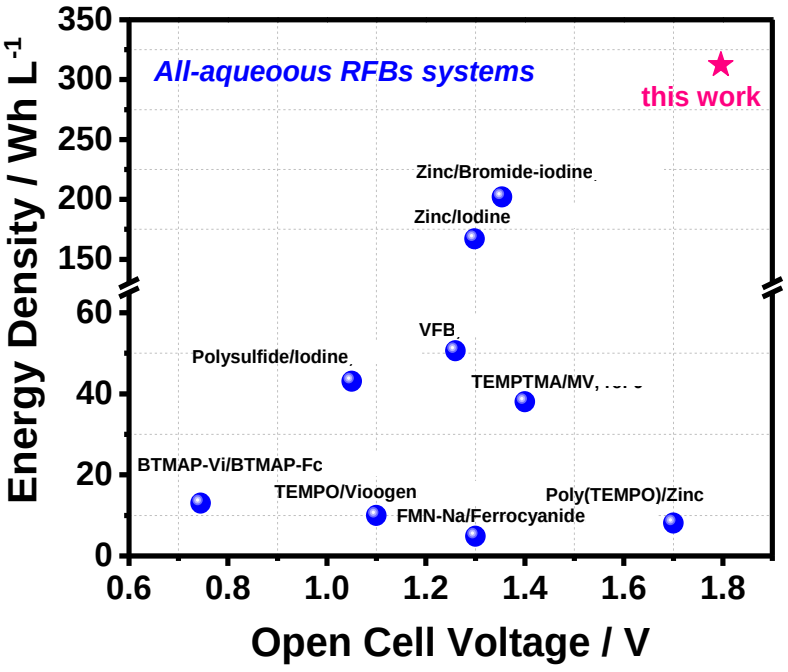

Figure 3-10. Diagram of energy density of all-aqueous redox flow battery in recent years compared with the value in this work.

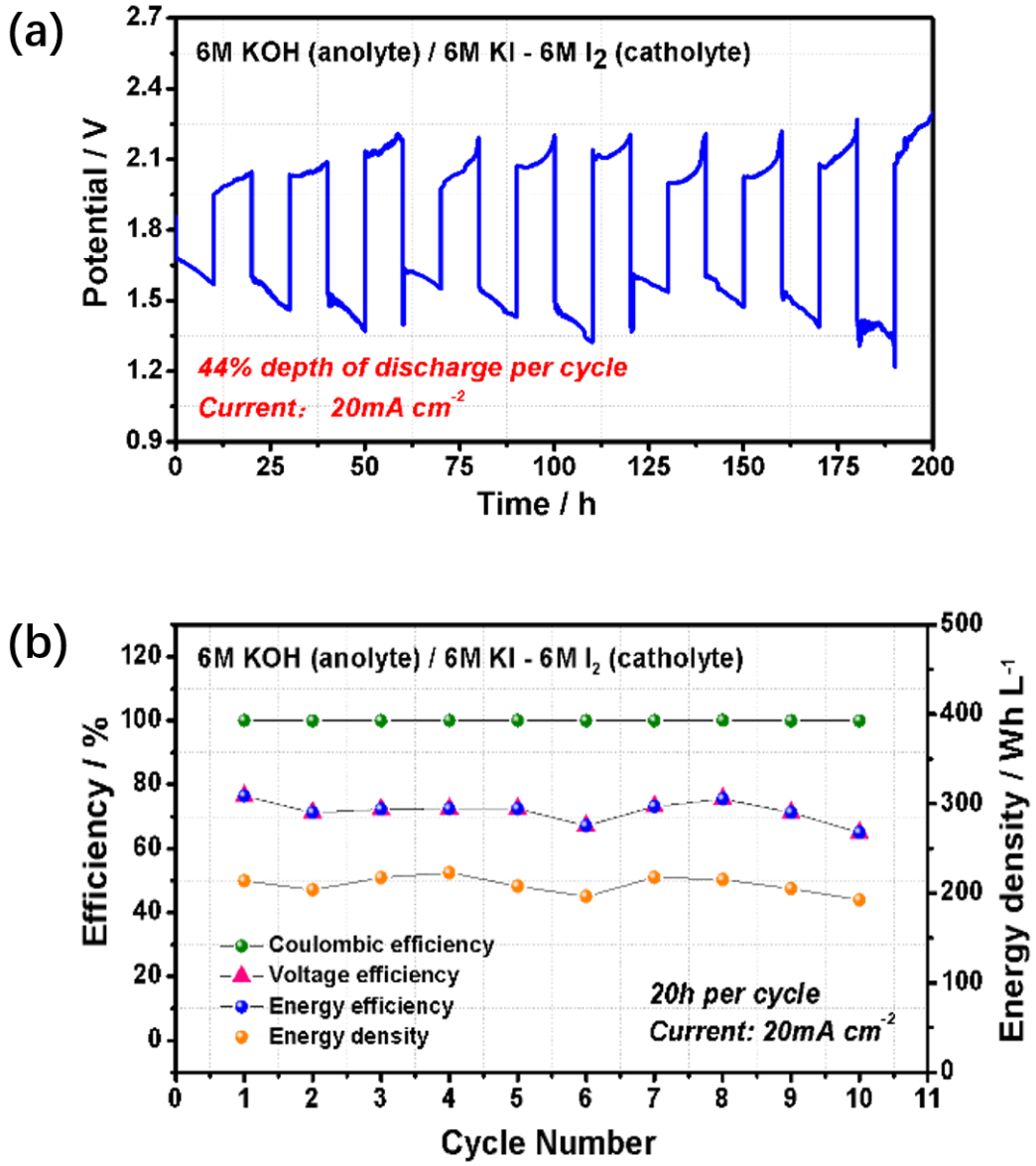

Figure 3-11. (a) Long-term cell cycling performance of voltage curve at 20 mA cm^{-2} and (b) the corresponding coulombic efficiency (CE), voltage efficiency (VE), energy efficiency (EE), and energy density of the experimental Zn-I_2 RFB.

To investigate the battery's ability to maintain its high energy density, the cycling performance of alkaline Zn-I_2 RFB was investigated through a long-term 20-hour per cycle testing at a current density of 20 mA cm^{-2}, which is a 44% depth of discharge cycles according to the theoretical battery capacity. As shown in **Figure 3-11**a and b, the battery

achieved a 100% coulombic efficiency during all 10 cycles (200 h), but the voltage and energy efficiencies exhibited fluctuations from 65% to 80%. The main reasons come from three parts on the zinc plate anode: passivation, electrode shape change and zinc dendrites.[130] During discharge, zinc is generally dissolved into the alkaline electrolyte, producing $Zn(OH)_4^{2-}$ ions in anolyte. However, if there is not enough OH^- offered in the anolyte and the $Zn(OH)_4^{2-}$ ions reach their solubility limit, an insulating ZnO film will be produced and precipitated on the electrode surface, causing an increase in the internal resistance of the electrode.[131] Also, during charge, zinc will be deposited back onto the electrode but at a different position, resulting in the shape change of the zinc electrode and a loss of usable capacity. Furthermore, zinc dendrites are also observed during charge due to a result of concentration-controlled zinc electrodeposition.[130, 132, 133] Therefore, after each three or four cycles, a fresh zinc plate was used to replace the exhausted zinc electrode to achieve stable energy density. Finally, an energy density of ~ 200 Wh L^{-1} was obtained during all of the cycles (200 h), which is the highest reported cycling energy density for an all-aqueous RFB.

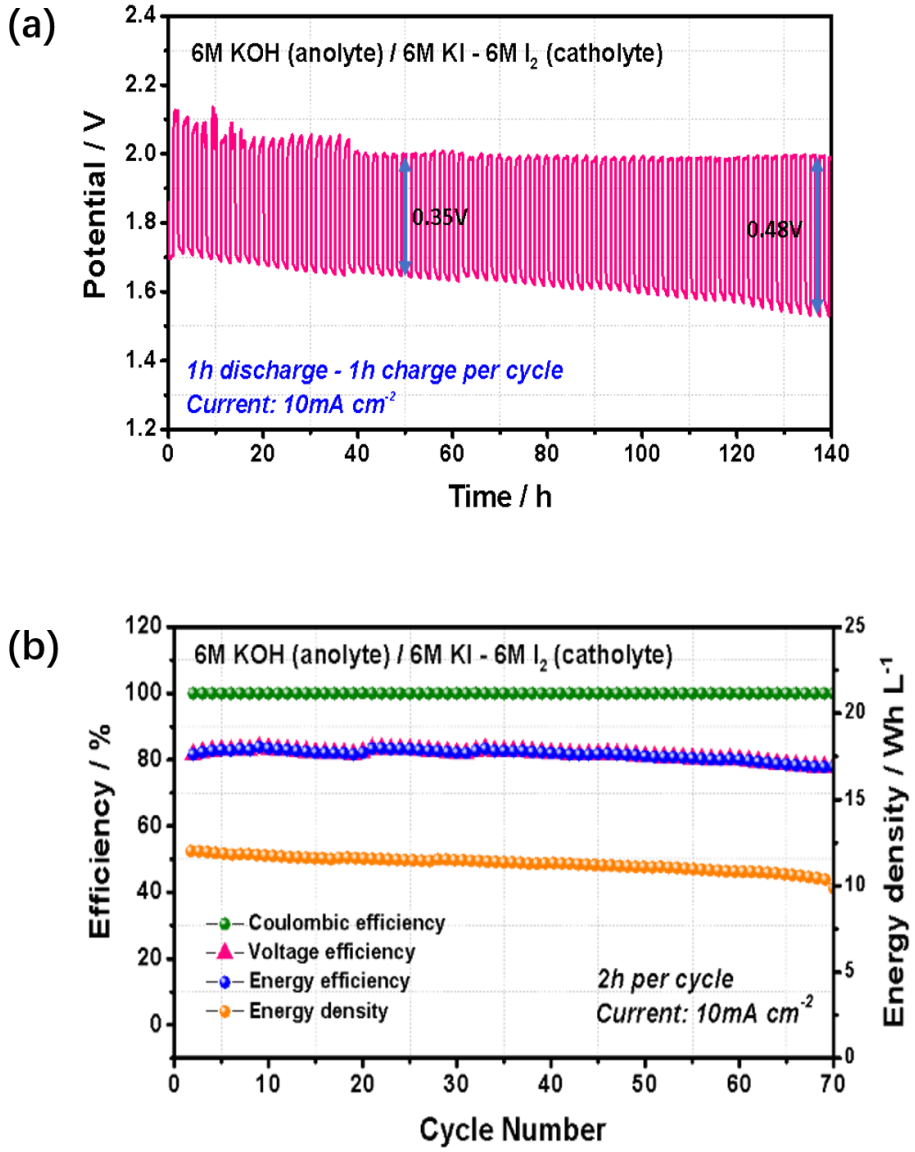

Figure 3-12. (a) Short-term cell cycling performance of voltage curve at 10 mA cm^{-2} and (b) the corresponding CE, VE, EE, and energy density of the experimental Zn-I_2 RFB.

The cycling performance of alkaline Zn-I_2 RFB was also investigated through short-term cycles with long stability. In the short-term cycling testing, the discharge and charge cycling performance of the battery was evaluated using a pulse cycling technique with each short 2-hour cycle at a current density of 10 mA cm^{-2}. As shown in **Figure 3-**

12a, the battery has a fluctuating charge voltage within the first 40 hours. This is because during the very early stages, short term discharge cannot produce enough $Zn(OH)_4^{2-}$ (in anolyte) and I^- (in catholyte) to afford a charge of the same time length, thus leading to an unstable performance in charge processing in the first 40 hours. Afterwards, the battery exhibits a very small polarization with a charge-discharge voltage gap of 0.35V. Even at 140 hours, the discharge voltage was still above 1.5 V with a corresponding charge voltage at around 2.0 V. During the overall 70 cycles (140 h), the battery displayed an excellent 100% coulombic efficiency and a promising 80% voltage/energy efficiency (in **Figure 3-12**b), which demonstrates a superior cycling stability of this alkaline Zn-I_2 RFB.

3.4 Conclusions

In summary, a novel strategy towards high energy density all-aqueous redox flow battery has been put forward in this work. Theoretically, high energy density can be achieved by enhancing battery voltage, and the electrolyte acidic/basic properties have a great influence on redox pair potential. Thus, by tuning the pH of the electrolyte, the battery voltage can be effectively enhanced, finally leading to an increase in energy density. With this strategy, we demonstrate an all-aqueous alkaline Zn-I_2 RFB achieving a high-energy-density of 330.5 Wh L^{-1} with a 0.47 V anode potential enhancement compared to the conventional counterpart, which is the highest energy density for an all-aqueous redox flow battery obtained to date. In addition, the alkaline Zn-I_2 RFB also exhibits a promising cycling performance with 100% coulombic efficiency, ~ 70% voltage and energy efficiency and high energy density of ~ 200 Wh L^{-1} maintained in 200 h. However, though these preliminary results are promising, numerous challenges still exist such as electrolyte

preparation issue, electrolyte crossover problem, electrode polarization, etc. More works are needed to perfect this system in the future, for example the development of a separator membrane, highly active electrocatalyst and advanced cell design.[134-140] Overall, this alkaline Zn-I_2 RFB system demonstrates a new design with promising performance for an all-aqueous redox flow battery, and more importantly, opens a feasible and effective approach for achieving high-voltage high-energy-density all-aqueous electrochemical energy device.

Chapter 4 Laminated Cross-linked Nanocellulose/Graphene Oxide Electrolyte for Flexible Rechargeable Zinc-Air Batteries

4.1 Introduction

In order to spur the development of next-generation portable electronics, it is essential to produce batteries with high energy-density, flexibility, reliability and safety.[141-144] Metal-air rechargeable batteries are considered as one of the best candidates due to their unique half-opened systems that consume inexhaustible oxygen at the air electrodes, resulting in a high theoretical energy density.[145-150] Particularly, zinc-air batteries have attracted most attention owing to their inexpensive materials, environmental benignity and safe operation.[151-155] Recent progress in flexible zinc air battery has been demonstrated with a polymer-based rechargeable zinc air battery which has high-energy density under mechanical bending stress.[141] A new design concept of stretchable wearable cable-type zinc air battery has also been proposed with unusual omni-directional flexibility.[156] Furthermore, a flexible fiber-shaped zinc air battery with a miniaturized one dimensional structure has been developed representing a considerable advancement in conventional battery design.[157] However, in portable applications, their merits are largely limited by the bulky battery configurations, as a result of relying on aqueous electrolytes.[158, 159]

To this end, one approach is to swap aqueous electrolytes for versatile, solid-sate alternatives, making zinc-air batteries safer, lighter and more portable. The main issues related to the solid-state electrolytes are insufficient ionic conductivity, electrolyte retention and complex synthesis process.[24, 160-162] To address these challenges, researchers have sought to highly efficient solid-state electrolytes based on graphene oxide (GO), the

oxidation product of natural graphite flakes.[163-165] GO has been demonstrated as a promising candidate because of its outstanding physicochemical stability and electrochemical properties.[166-168] Additionally, GO is a well-known electronic insulator with abundant oxygen-containing groups (epoxy, hydroxyl and carboxyl groups), which can be easily functionalized to improve its ionic conductivity.[163, 169] Owing to the wide range of oxygen functional groups on its basal planes and edges, GO is also readily exfoliated to yield well-dispersed solution of individual GO sheets in both water and organic solvents, and then flow-directed assembled into a free-standing paper-like material by vacuum filtration.[163, 170]

However, despite all the progress of the development of a free-standing GO electrolyte membrane, its advantages are diminished with the difficulty to form a mechanically robust membrane.[170, 171] Consequently, that makes the free-standing GO membranes less attractive for practical application in solid-state electrolytes in energy storage systems. To enhance the mechanical strength, several fillers can be incorporated into GO matrix. Among the multifarious materials, cellulose — the most abundant renewable material — is recognized as a good binder and surface modifier thanks to its low cost, high hygroscopicity, flexible porous substrate that allows strong binding of other materials. Particularly, considerable interest has been directed to nanocellulose fibre because of its low thermal expansion, high surface area, high surface area-to-volume ratio, strengthening effect, good mechanical and optical properties which may find many applications in nanocomposites.[172-175] Meanwhile, due to its highly reactive area rich in hydroxyl groups, cellulose can be easily refashioned through a surface-functionalization to

conduct ions and be utilized in advanced batteries.[158]

In this chapter, for the first time, we report on a laminate-structured nanocellulose/GO membrane functionalized with highly hydroxide-conductive quaternary ammonium (QA) groups to be applied as a robust solid-state electrolyte in flexible, rechargeable zinc-air batteries. The QA-functionalized nanocellulose/GO (QAFCGO) membrane is fabricated through chemical functionalization, layer-by-layer filtration, cross-linking and ion-exchange processes (**Figure 4-1**).

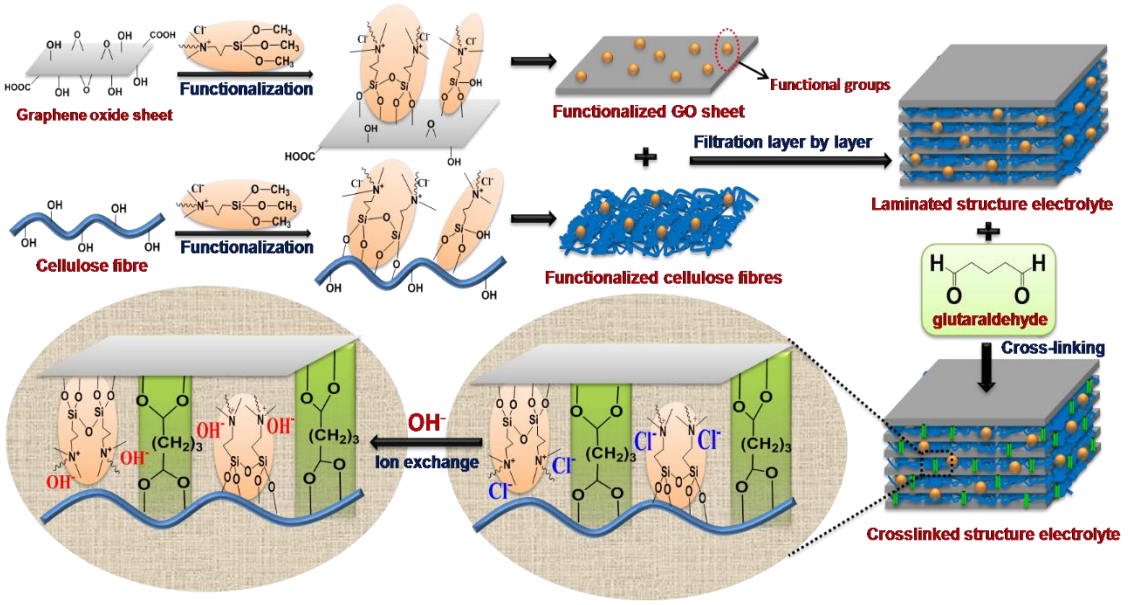

Figure 4-1. Schematic diagram of the overall preparation procedure (functionalization, filtration, cross-linking and hydroxide-exchange) for the QAFCGO membrane.

4.2 Experimental Methods

4.2.1 Synthesis of graphene oxide

Graphene oxide was synthesized by the improved Hummers' method from natural graphite flakes. First, concentrated H_2SO_4 (360 mL, 98%) and H_3PO_4 (40 mL, 85%) were mixed carefully in a round-bottom flask. Graphite powder (2g) was added into the mixture and mechanically stirred for 1 h. Then, the strong oxidizing agent $KMnO_4$ (18 g) was added slowly into the mixed solution, and the oxidation reaction lasted at 50^oC for 16 h. After cooling down the mixture, distilled deionized (DDI) water (400mL) and H_2O_2 (20 mL, 30%) were added dropwise and then stirred for 30 min. Afterward, the mixture was centrifuged and washed with DDI water, HCl (5%), and ethanol, respectively. Finally, the GO nanosheets were obtained by freeze-drying.

4.2.2 Preparation of cellulose nanofibers

Three steps of pre-refining, enzymatic processing and nano-refining were proceeded to produce the cellulose fibres from Northern Bleached Softwood Kraft pulp (New Brunswick, Canada). First, the pre-refining was conducted by using the Noram PFI mill (Quebec, Canada) with a revolution up to 30000 to disintegrate the original pulp. Then, an enzyme treatment of the refined pulp was carried out with a mixture of two enzymes (i.e., Mannanase and Xylanase) from Novozymes (Franklinton, USA) to gain a uniform pulp suspension. Finally, the enzyme treated pulp was washed several times with DDI water to remove unreacted residues, and then charged into the PFI mill again with the revolution to 30000 to produce cellulose fibres.

4.2.3 Functionalization of QAFGO and QAFC

In order to obtain quaternary ammonia-functionalized GO (QAFGO) and cellulose (QAFC), Dimethyloctadecyl[3-(trimethoxysilyl)propyl]ammonium chloride (DMAOP) (42 wt. % in methanol, Sigma Aldrich) was adopted as the precursor. First, freeze-dried GO (60mg) was dispersed in toluene (60ml) by sonication for 2 h to obtain a stable GO suspension. cellulose fibres (300 mg) was dispersed in methanol solution (150 ml) by sonication for 2 h to obtain a stable cellulose fibre suspension. DMAOPS was added into GO and cellulose suspension in ratio DMAOP:GO/cellulose being 20:1 by mass. The functionalization was carried out at room temperature under magnetic stirring for 48 h. Then, the suspension was centrifuged and washed several times with ethanol and DDI to remove the unreacted traces of DMAOP. At last, the QAFGO and QAFC were obtained and stored in DDI water.

4.2.4 Fabrication of hydroxide-conductive QAFCGO membrane

The hydroxide-conductive QAFCGO membrane was fabricated with QAFGO and QAFC through vacuum filtration, cross-linking and ion-exchange process. First, the vacuum filtration was carried out by alternating round of QAFGO (15 ml, 1 mg mL^{-1}) and QAFC (5 ml, 1 mg mL^{-1}) to obtain a laminated structure membrane. The membrane was then chemical cross-linked with 10 wt% glutaraldehyde (GA) and 0.2 wt% hydrochloric acid (HCl) in acetone at room temperature for 2 h. The ion-exchange was processed by immersing the membrane in 1 M KOH solution and equilibrated for 24 h to convert chlorine (Cl^-) counterion into hydroxide (OH^-). The OH^- exchanged membrane was then washed with DDI water until pH of 7. The hydroxide-conductive membrane with thickness

range of 30-50 μm was thereby obtained (the thickness of A201 was recorded to be 30 μm).

4.2.5 Fabrication of solid-state rechargeable zinc-air battery

A rechargeable zinc-air battery was fabricated through a layer-by-layer method by which the electrodes were placed face-to-face with the membrane. Zinc pellet and zinc film were prepared as zinc electrode for regular and flexible zinc-air battery, respectively. The zinc pellet was made of pure zinc power (purum powder, Sigma Aldrich) and the zinc film was consisted of zinc powder, carbon nanofiber, carbon black and poly(vinylidene fluoride-co-hexafluoropropene) polymer binder. An air electrode was prepared by Co_3O_4 nanoparticles (<50 nm particle size, Sigma Aldrich) as the bi-functional electroactive material sprayed onto a carbon cloth (Fuel Cell Technology). Catalyst ink consisted of 10 mg Co_3O_4, 67 μl of 5 wt.% Nafion (LIQUion™ solution, Ion Power Inc.) and 1.0 ml 1-propanol was sprayed onto a carbon cloth (Fuel Cell Technology) as the gas diffusion layer with a catalyst loading of 1.0 mg cm^{-2}. After spraying, the electrode is dried in an oven at 60 °C for 1 h.

4.2.6 Characterization and electrochemical measurement

The morphology of the membrane and the cellulose fibres were imaged by scanning electron microscopy (SEM) (LEO FESEM 1530) and transmission electron microscopy (TEM) (Bruker AXS D8 Advance). Fourier transform infrared spectra (FTIR) (Avatar 320), X-ray photoelectron spectroscopy (XPS), and (Thermo Scientific Al K-Alpha X-ray source) X-Ray Diffraction (XRD) (INEL XRG 3000) were utilized to analyze the chemical and crystal structure after functionlization of GO and cellulose. Electrochemical impedance spectroscopy (EIS) (VersaSTAT MC potentiostat) was carried out in the frequency ranging

from 100 kHz to 0.05 Hz with potential amplitude of 20 mV. The battery charge and discharge polarization data were collected using galvanodynamic method at a scan rate of 1.0 mA s^{-1} with cut-off voltage of 0.5 V for the discharge and 2.5 V for the charge. Discharge and charge cycles were carried out by a recurrent galvanic pulse method at a fixed current density of 1 mA cm^{-2} with each cycle consisting of 10 min for discharge followed by 10 min for charge.

4.3 Results and Discussions

In this chapter, a laminate-structured nanocellulose/GO membrane was synthesized and functionalized with highly hydroxide-conductive quaternary ammonium (QA) groups to be applied as a robust solid-state electrolyte in flexible, rechargeable zinc-air batteries. The QA-functionalized nanocellulose/GO (QAFCGO) membrane is fabricated through chemical functionalization, layer-by-layer filtration, cross-linking and ion-exchange processes. For the functionalization process, dimethyloctadecyl [3-(trimethoxysilyl)-propyl] ammonium chloride (DMAOP) has been selected as the functional precursor containing quaternary ammonium (QA) moieties. The hydroxide conductivity and the alkaline stability in the highly surface-active DMAOP are provided by quaternary ammonium groups which are already attached to this organic compound. Thus, the hydroxide conducting characteristic of the electrolyte membrane can be achieved directly through the precursor DMAOP without complex organic synthesis. First, the trimethoxy groups of trimethoxysilyl are hydrolyzed to form the corresponding silanols, and the hydrolyzed silanols undergo self-condensation to yield silanol oligomers intermediates (**Figure 4-2**, step 1). Then, these intermediates are adsorbed onto nanocellulose/GO

surface rich in oxygen-containing groups through hydrogen bonding (**Figure 4-2**, step 2). Finally, these silanols and their oligomers are covalently bound to the oxygen-containing groups of nanocellulose/GO by losing water (**Figure 4-2**, step 3).[165]

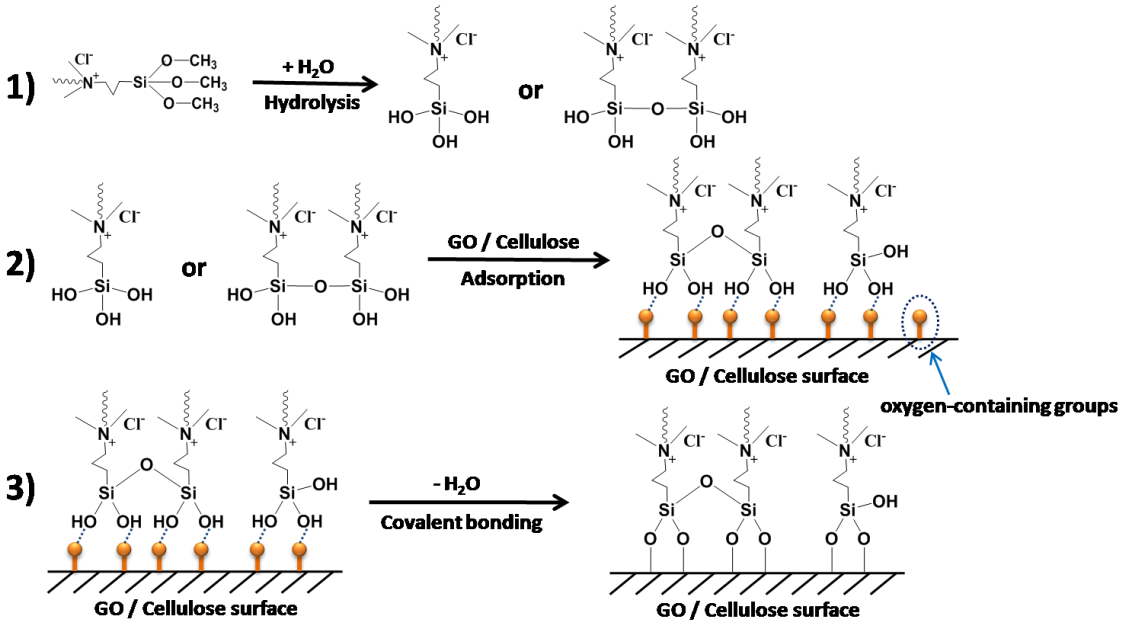

Figure 4-2. Proposed three-step reaction mechanism for GO/Cellulose surface functionalization with DMAOP.

In the next step, the water-based suspensions of QA-functionalized GO nanosheets and cellulose nanofibres alternately go through vacuum filtration to form a laminate-structured membrane (**Figure 4-3**a) supported by QA-functionalized GO at the top and bottom with a flat and uniform surface (**Figure 4-3**b). During the filtration process, the numerous cellulose nanofibres tend to construct a dense interwined porous network (**Figure 4-3**c), and perform as binder layers to integrate each single thin GO film into a robust membrane. The subsequent cross-linking reaction via glutaraldehyde (GA) strongly consolidates the integrated membrane through covalent linkages between GO and nanocellulose. GA, which contains two aldehyde functional groups, reacts with hydroxyl

groups on the surface of GO nanosheets and cellulose nanofibres, and forms an acetal structure, resulting in a steady-state cross-linked laminate-structured membrane.[160, 176, 177]

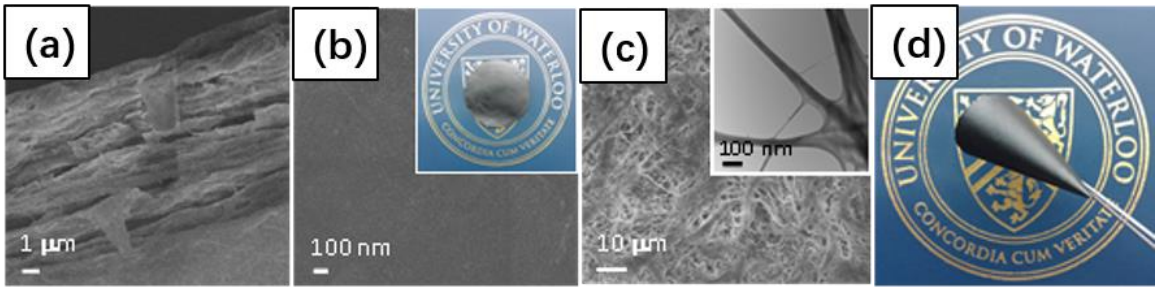

Figure 4-3. (a) A SEM image (cross section) of the QAFCGO membrane. (b) A SEM image (surface view) of the QAFCGO membrane with an inset photograph of QAFCGO membrane showing flat and uniform GO surface. (c) A SEM image of the cellulose dense interwined network structure with an inset TEM image of cellulose fibres. (d) A Photograph of the QAFCGO membrane showing flexibility.

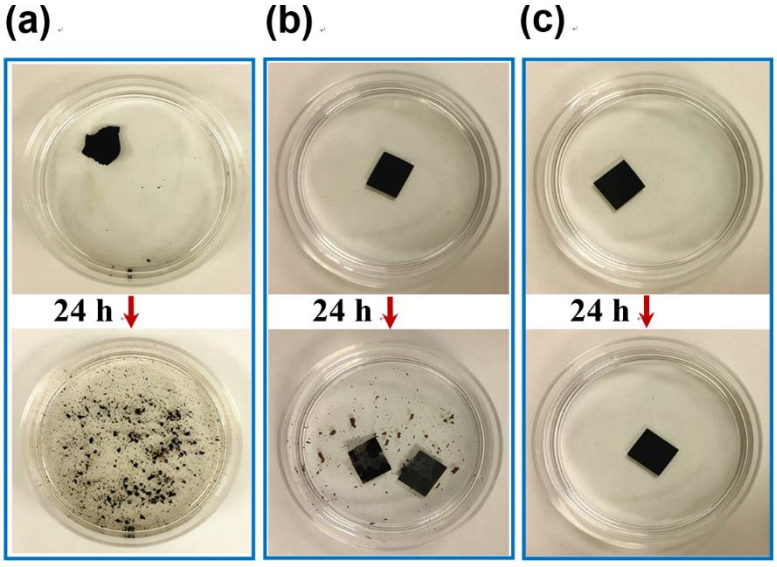

Figure 4-4. The stability of GO film and QAFCGO membrane in water. (a) GO film, (b) QAFCGO membrane without crosslinking, (c) QAFCGO membrane after crosslinking.

Figure 4-4a shows the poor chemical stability of GO membrane which has been completely redispersed in water after 24 h. Compared to the GO membrane, the composed GO nanosheets with interconnected nanocellulose framework (**Figure 4-4**b) has demonstrated more stable structure. Particularly, the cross-linked QAFCGO membrane remains intact in water after 24 h without any disintegration (**Figure 4-4**c). Finally, after the ion exchange process, the hydroxide-conducting QAFCGO membrane is obtained with excellent flexibility as shown in **Figure 4-3**d.

To confirm the successful functionalization reaction, FT-IR spectra of GO, pristine cellulose (PC), quaternary ammonium-functionalized GO (QAFGO) and quaternary ammonium-functionalized cellulose (QAFC) are compared in **Figure 4-5**a. In the GO spectrum, the characteristic peaks are observed at 1739 cm^{-1} (carbonyl C=O), 1619 cm^{-1} (sp^2 carbon C=C), 1384 cm^{-1} (O-H vibration of C-OH), 1224 cm^{-1} (carbon-hydroxyl C-OH), 1054 cm^{-1} (epoxide C-O-C), 856 cm^{-1} (epoxy rings) and a broad band at 3200 – 3500 cm^{-1} (free hydroxyl O-H), which indicates abundant oxygen-containing groups on its basal planes and edges.[163, 164] In the spectrum of QAFGO, after functionalization, the peaks assigned to the vibration of C=O (1739 cm^{-1}), C-OH (1224 cm^{-1}), C-O-C (1054 cm^{-1}) and epoxy rings (856 cm^{-1}) disappear.[165] Alternatively, two new small peaks at 2852 and 2921 cm^{-1} emerge in the spectrum, owing to methyl and long chains of methylene groups in the precursor (DMAOP), which indicates the effective grafting reaction between the oxygen functional groups of GO and QA groups of DMAOP. In the PC spectrum, the peak at 3342 and 2900 cm^{-1} are attributed to the O-H and sp^3 hybridized C-H stretch vibration in the PC membrane. The small peak at 1641 cm^{-1} could be assigned to the O-H of water

absorbed from cellulose.[178] In the C-O stretching vibration region, the peaks at 1163, 1111, 1059 and 1035 cm^{-1} are corresponding to the vibrations of C1-O-C4, C2-O2H, C3-O3H and C6H2-O6H.[179] Similar to QAFGO, two new peaks at 2852 and 2921 cm^{-1} have appeared after functionalization reaction, which come from the moiety of DMAOP and confirm the successful functionalization of nanocellulose.

The XPS analysis of GO, PC, QAFGO and QAFC is carried out to assist the FT-IR results (**Figure 4-5**b). In the wide-range XPS pattern of QAFGO, three small peaks other than C 1s and O 1s are detected at binding energies of 103.1, 154.1 and 403.4 eV, assigned to Si 2p, Si 2s and N 1s, respectively. Similar characteristic peaks of Si and N are observed in the XPS pattern of QAFC. According to C 1s spectra in **Figure 4-5**c, the shifted peaks of oxygenated carbon groups in GO indicate a change degree of surface oxidation after functionalization. The decrease of peak intensity at 287.02 eV can owe to the reaction between oxygen functional groups of GO and trimethoxylsilyl of DMAOP, which is in agreement with the results of FT-IR. Furthermore, the significant increase of C-C/C-H peak intensity at 288.68 eV (GO) demonstrates the increase of carbon atoms proportion due to the attached long alkyl chains of QA groups. Similarly, the C 1s spectra of cellulose also show a downward trend of the oxygenated carbon groups peak intensity and a growing trend of C-C/C-H peak intensity, which further proves the present of QA functional groups on the surface of cellulose fibers.

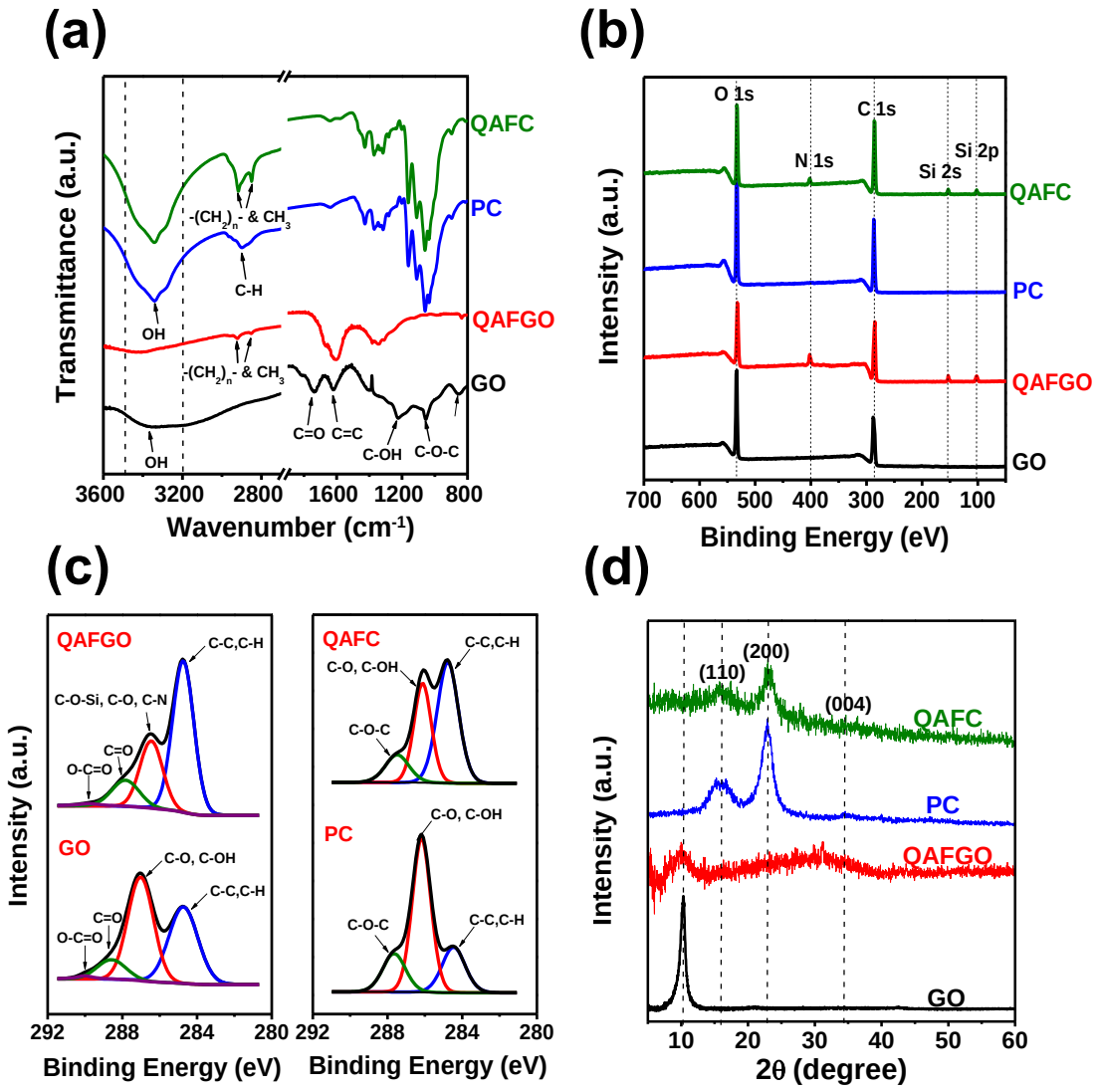

Figure 4-5. (a) FT-IR spectra. (b) wide region XPS spectra. (c) deconvoluted XPS spectra in the C 1s region. (d) XRD pattern of GO, PC, QAFGO and QAFC.

In order to analyze the structure variation of GO nanosheets and cellulose nanofibers after functionalization, the XRD of GO, PC, QAFGO and QAFC is studied in **Figure 4-5**d. In the XRD pattern of GO, a sharp and narrow peak is obtained at 2θ = 10.3°, exhibiting a d-spacing of 8.58 Å which is in agreement with the literature.[180] After functionalization with DMAOP containing bulky QA groups, the original peak at 2θ =10.3° becomes much broader, giving a higher d-spacing of 10.04 Å. This indicates that

the bulky QA groups of DMAOP have successfully bound to GO and expanded the interplanar distance of nanosheets, resulting in more free space for the entrance of small water molecules that are vital to assist the ion transport.[165] In the XRD pattern of PC, three characteristic peaks at 16.9°, 22.9°, 34.5° are detected corresponding to the typical cellulose I crystalline planes (110), (200) and (004).[179] However, the intensities of these three peaks obviously reduce in the XRD pattern of QAFC, which indicates that a significant portion of the cellulose I crystalline structure has converted into an amorphous phase. Such structural transformation can facilitate the ion transport because of the increased amorphousness with more hydrophilic domain.

The high ion conductivity is an important indication for a well-performed electrolyte. In order to study the hydroxide conductivity of the laminated QAFCGO membrane, the ion conductivities of QAFGO and QAFC after hydroxide exchange are compared to that of QAFCGO. As shown in **Figure 4-6**a. The pristine GO and PC exhibit low conductivities of only 2.5 and 2.0 mS cm^{-1} at room temperature. However, after grafting QA groups and ion-exchange of hydroxide ions, the ionic conductivities of QAFGO and QAFC significantly improve to 39.0 and 25.0 mS cm^{-1} respectively, which are almost ten times higher than those of the pristine GO and PC. The remarkable improvement of ionic conductivities is ascribed to the high mobility of hydroxide ions dissociated from the grafted QA groups. Interestingly, the functionalization of PC not only grafted adequate amount of QA groups onto the surface of cellulose fibers, but also converted a significant proportion of its crystalline structure into an amorphous phase (according to the XRD results, **Figure 4-5**d). The increase of dynamic and disordered

amorphous morphology plays a critical role in facilitating the ion transport compared to the well-ordered crystalline structure, thus further improves the ionic conductivity of QAFC. The temperature dependencies of ionic conductivities are also measured to fully understand the ion transport mechanism. All the samples are well hydrated and evaluated in the range of 30ºC to 70ºC. As shown in **Figure 4-6**b, the activation energies are calculated using the Arrhenuis equation, achieving data of 16.3, 8.4, and 10.5 kJ mol^{-1} for QAFGO, QAFC, and QAFCGO, respectively. According to the XRD results and activation energies of QAFCGO, QAFGO and QAFC, two types of ion transport mechanisms including Grotthuss mechanism and vehicle mechanism exist (**Figure 4-6**c).[24] The suggested mechanism of hydroxide mobility is similar to that of proton mobility in water, and it is already clear that the structure depends strongly on the surrounding water molecules.[181] OH^- transports through the hydrogen bonds network in water molecules by forming $[H_3O_2]^-$ conjugate and cleavages into H_2O and OH^- and keeping regularity of this process. In the presence of abundant water molecules, large amounts of hydroxide ions can be dissociated from the grafted QA groups, and then form into hydrated hydroxide ions with surrounding water molecules. After functionalization, the enlarged d-spacing of GO nanosheets gives more spaces for the hydrated hyroxide ions to migrate via vehicle mechanism. In QAFC, although some hydroxide ions can still move through the vehicle mechanism, due to the lower activation energy, the Grotthuss mechanism is dominant, in which the hydroxide ions can hop between two neighbor functionalized sites without any carrier molecules. Therefore, ion migration in the QAFCGO membrane is a complex system with two transport mechanisms occurring simultaneously. Both mechanisms have

exhibited positive temperature-conductivity linear relationships, and finally leading to a high ion conductivity of 58.8 mS cm^{-1} at 70°C for the QAFCGO membrane.

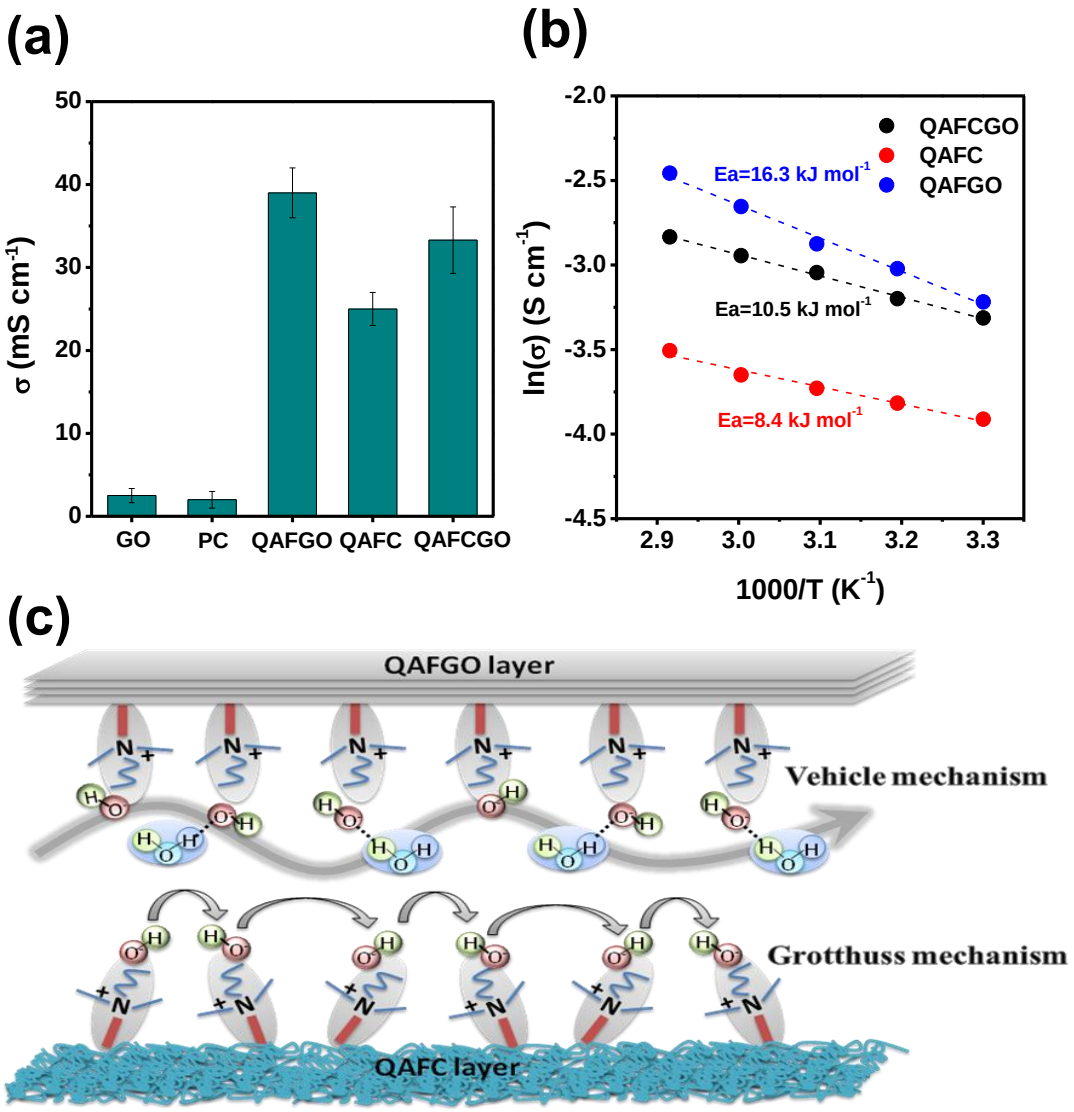

Figure 4-6. (a) Ionic conductivity of the GO, PC, QAFGO, QAFC and QAFCGO. (b) Arrhenius plot of ionic conductivity of the QAFGO, QAFC and QAFCGO membranes as a function of temperature. (c) A schematic illustration of ion transport mechanism with QAFGO and QAFC.

The practical performance of the QAFCGO membrane is demonstrated in a rechargeable, flexible zinc-air battery under atmospheric air. The battery was assembled through layer-by-layer method, in which the QAFCGO membrane was paired with a zinc pellet electrode and a bifuncitonal air electrode with commercial cobalt oxide nanoparticles deposited on a carbon paper. The battery using the commercial A201 anion-exchange membrane from Tokuyama was also fabricated for the comparison. **Figure 4-7**b shows the charge and discharge polarization curves. The QAFCGO-based battery exhibits a high open circuit voltage of ~1.4 V, similar to that of the A201-based battery. In **Figure 4-7**b, at high current densities beyond 20 mA cm^{-2}, the QAFCGO-based battery shows a remarkable advantage over the A201 battery, with smaller over potentials for both discharge and charge processes. For instance, at high current density of 60 mA cm^{-2}, the charge and discharge potentials of QAFCGO-based battery are 291 mV and 154 mV smaller than those of A201-based battery. This is further supported by the fact that the corresponding peak power density of the QAFCGO-based battery (44.1 mW cm^{-2}) is higher than that of the A201-based one (33.2 mW cm^{-2}) (**Figure 4-8).** The pronounced performance indicates the great potential of the QAFCGO membrane for the solid-state rechargeable zinc-air battery application, compared to the commercial A201 membrane. The galvanostatic charge and discharge cycling performance of the batteries using the QAFCGO and A201 membranes are also evaluated using a pulse cycling technique with each cycle per 20 min at a current density of 1 mA cm^{-2}.

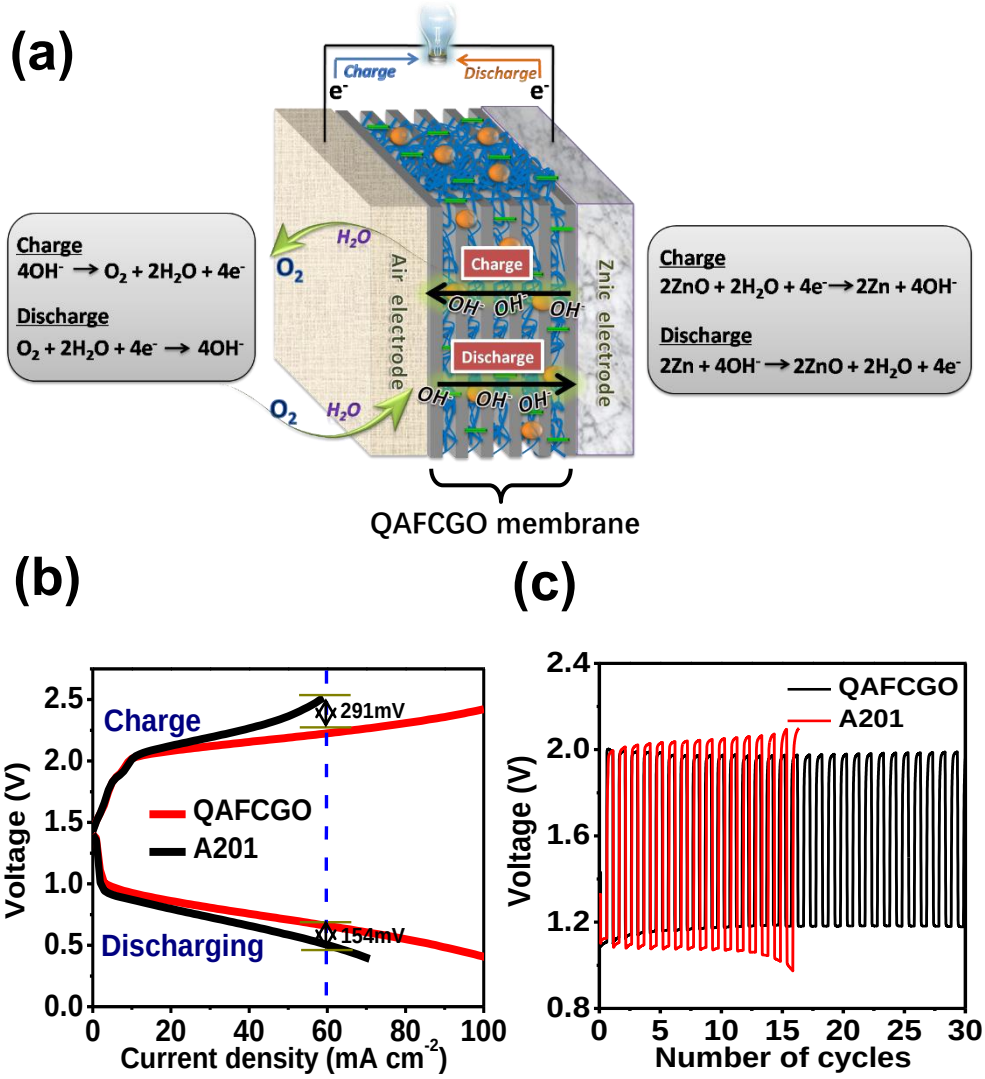

Figure 4-7. (a) A schematic image of rechargeable zinc-air battery using the QAFCGO membrane. (b) Charge and discharge polarization curves of the batteries using the QAFCGO and A201 membranes. (c) Galvanostatic charge and discharge cycling of the batteries using the QAFCGO and A201 membranes at a current density of 1 mA cm^{-2} with a 20 min per cycle period (10 min discharge followed by 10 min charge).

In addition, the QAFCGO-based battery exhibits much more stable cycling performance than that with the commercial A201 one. As shown in **Figure 4-7**c, the A201-based battery has shown noticeable performance degradation with large charge and discharge polarizations after 300 min, whereas the QAFCGO-based battery demonstrates

longer cycling time without any performance loss after 600 min. The admirable characteristics of the QAFCGO membrane, such as high ionic conductivity, guarantees enhanced cycling performance for solid-state batteries. Compared to the A201 membrane, the superior battery performance using the QAFCGO membrane owes more to its higher water uptake and smaller anisotropic swelling degree (**Table 4-1**). As shown in **Figure 4-7**a, during discharge, oxygen from the air reacts at the cathode and forms hydroxyl ions which migrate into the zinc electrode and form oxidized zinc species, releasing electrons to travel to the cathode. The oxidized zinc species decays into zinc oxide, and water returns to the electrolyte.[182] During charge, the zinc oxide reacts with water in the anode, while the water can be recycled back at cathode with oxygen evolution. Thus, during the overall operation process, the water and hydroxyl are recycled between the anode and cathode, and the water is not consumed.[183] However, water evaporation over time is unavoidable when the air electrode opened to atmosphere, leading to electrolyte dry out problems and a shortened battery life. Since water plays an important role in the ion transport, the loss of that can directly reduce the ionic conductivity, resulting in a large ohmic polarization of the battery. Meanwhile, the membrane wrinkling comes from the gain and loss of moisture during the battery charging and recharging process, which can result in an ineffective interfacial contact between the electrode and electrolyte. Thus the electrolyte becomes less accessible to the active materials at the electrode. Accordingly, the swelling ratio is another key factor that affects the battery cycling performance. As shown in **Table 4-1,** the water uptake of the QAFCGO membrane is 5 times higher than that of the A201 membrane, whereas its anisotropic swelling ratio is only half of that of the A201 membrane. As a result,

the QAFCGO-based zinc-air battery exhibits superior rechargeability and performance stability.

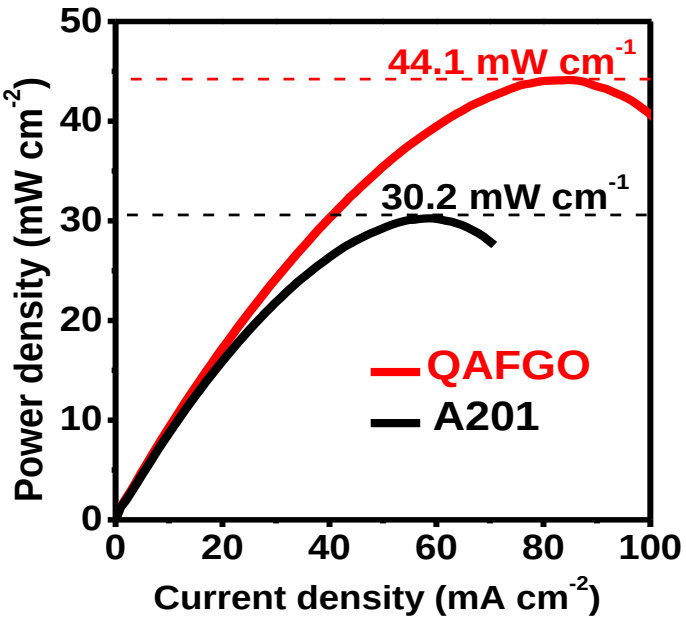

Figure 4-8. The power density plots of zinc-air batteries using the QAFCGO and A201 membranes at a current density of 1 mA cm^{-2}.

Table 4-1. Properties of the QAFCGO and A201 membranes.

Membrane	Ionic conductivity[a)] (mS cm^{-1})	Water uptake (g g^{-1})	In-plane swelling ratio (%)	Through-plane swelling ratio (%)	Anisotropic swelling degree
QAFCGO membrane	33.3	1.24	14.3	21.8	1.5
A201 membrane	42.0	0.25	2	6	3

[a)] Ionic conductivity measured at room temperature, 100% relative humidity.

As shown in **Figure 4-9**, the glavanostatic discharge performance of the solid-state zinc–air battery was investigated using the QAFCGO and A201 membranes. The measurement was carried out at a constant current of 1 mA cm^{-2} under atmospheric air. The

rapid voltage and capacity loss of the A201 membrane is due to a progressive loss of water and ionic conductivity in the membrane during the constant current discharge. It should be noted that simply wetting the A201 membrane by DDI water could regenerate the battery performance for subsequent runs with the same battery configuration. The QAFHM membrane obviously showed a higher discharge capacity (longer discharge time) than the A201 membrane. During the long-term discharge for the QAFHM membrane, a high voltage plateau of 1.15 V was observed within the first 300 min discharge, followed by a steady decline from 0.9 V to 0.7 V in the next 300 min. As a result, the QAFCGO membrane exhibited a higher discharge capacity with a more stable voltage character in comparison to the commercial A201 membrane.

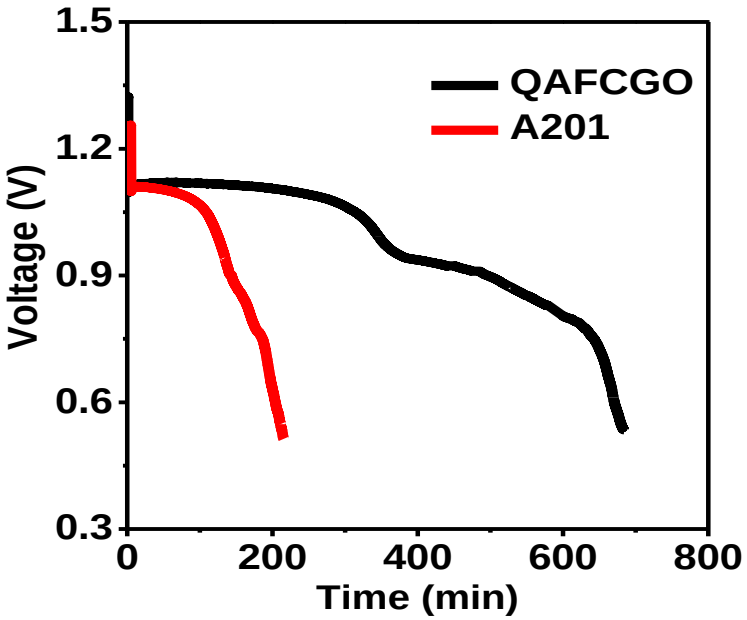

Figure 4-9. Galvanostatic discharge of zinc-air batteries using the QAFCGO and A201 membranes at a current density of 1 mA cm^{-1}.

Porous structure zinc electrode prior to the cycling is shown in **Figure 4-10**a,

where zinc particles are well-distributed at zinc electrode. After cycling, the surface of zinc particles is partially deposited with hollow, rob-shaped nanograins (**Figure 4-10**b), which is different with the well-known compact passivation layer of zinc oxide species. This observation indicates a good reversibility of the zinc electrode. The cycled zinc electrode was further identified by XRD (**Figure 4-10**c), containing zinc oxide, zinc hydroxide and zinc. In this regard, the reaction ($Zn(OH)_2(H2O)_2 \leftrightarrow ZnO + 3H_2O$) will continue to occur following the formation of $Zn(OH)_2$ at the electrode surface, depending on the availability of water and OH^-.

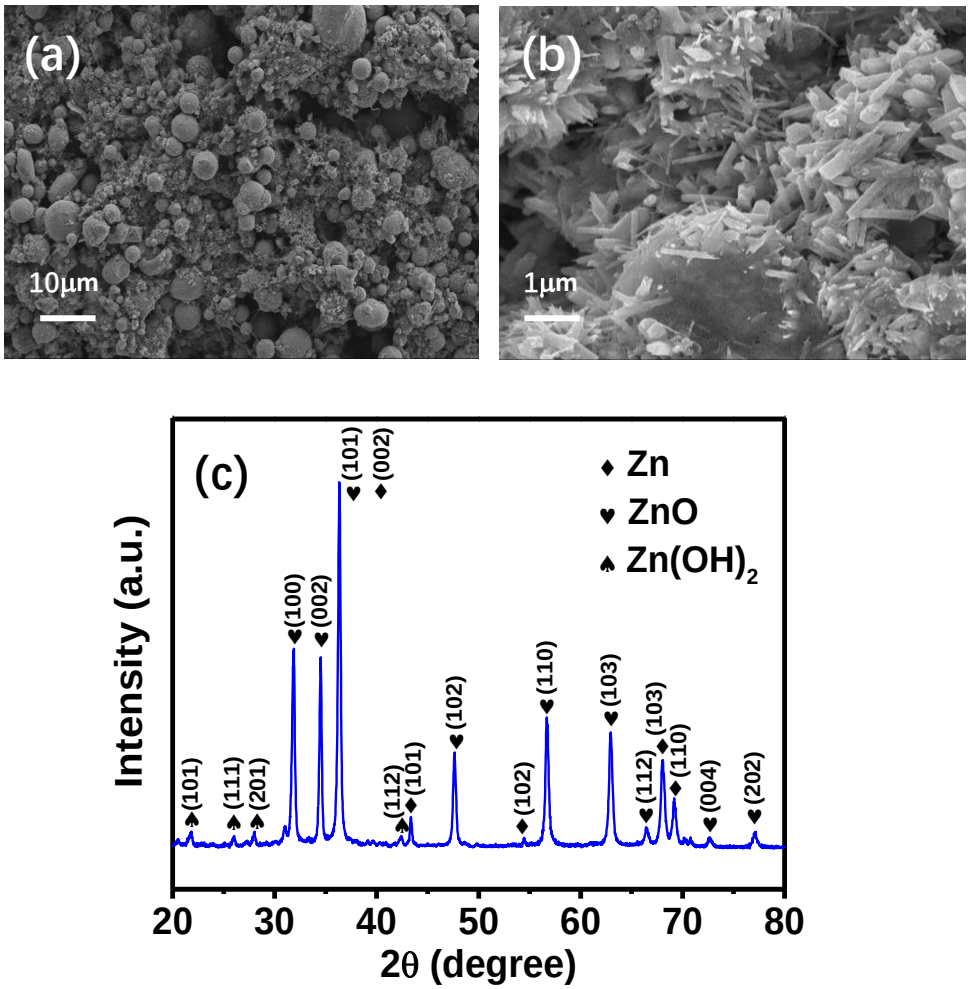

Figure 4-10. SEM images of the (a) fresh zinc electrode and (b) cycled zinc electrode. (c) XRD pattern of the cycled zinc electrode.

The mechanical property and morphology of QAFCGO membrane after 600 min galvanostatic charge and discharge cycling was performed respectively to evaluate the durability of QAFCGO membrane in Zn-air battery application. In **Figure 4-11**a, the membrane prior to the cycling presents uniform and flat GO surface. After 600 min cycling, the membrane can still keep the intact structure, only some small cracks are observed on the surface of membrane after long time cycling (**Figure 4-11**b). The mechanical property was evaluated by tensile strength and tensile elongation. As shown in **Figure 4-11**c, the elongations at break of the fresh and cycled membranes are both above 10%, indicating well tensile deformation by pulling force. After cycling, the tensile strength decreases from 120 MPa to 80 MPa, but still exhibit good material rigidity.

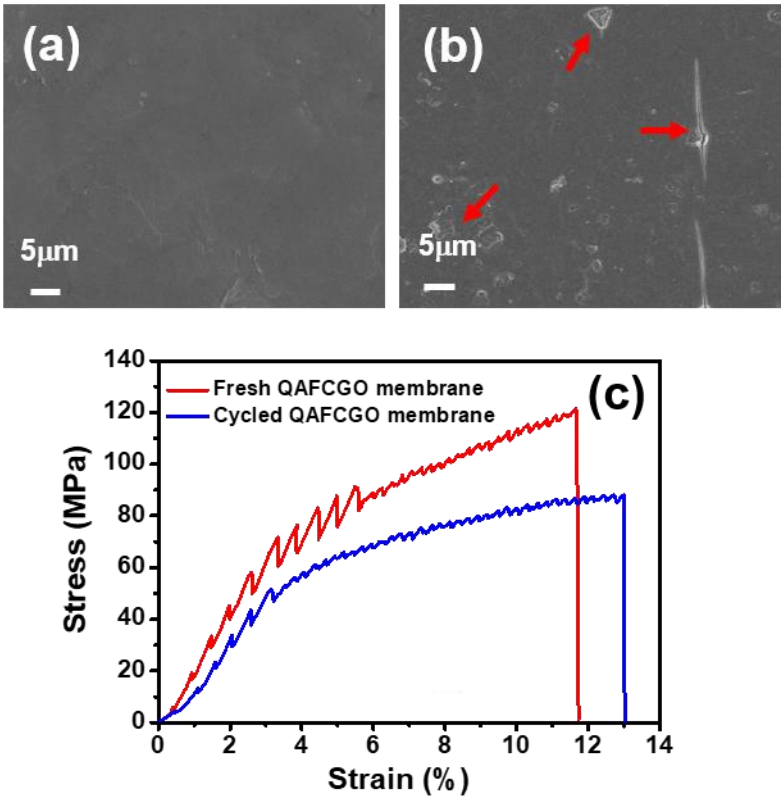

Figure 4-11. SEM images of the (a) fresh QAFCGO membrane and (b) cycled QAFCGO membrane. (c) Stress-strain curves of QAFCGO membrane before and after galvanostatic charge and discharge cycling.

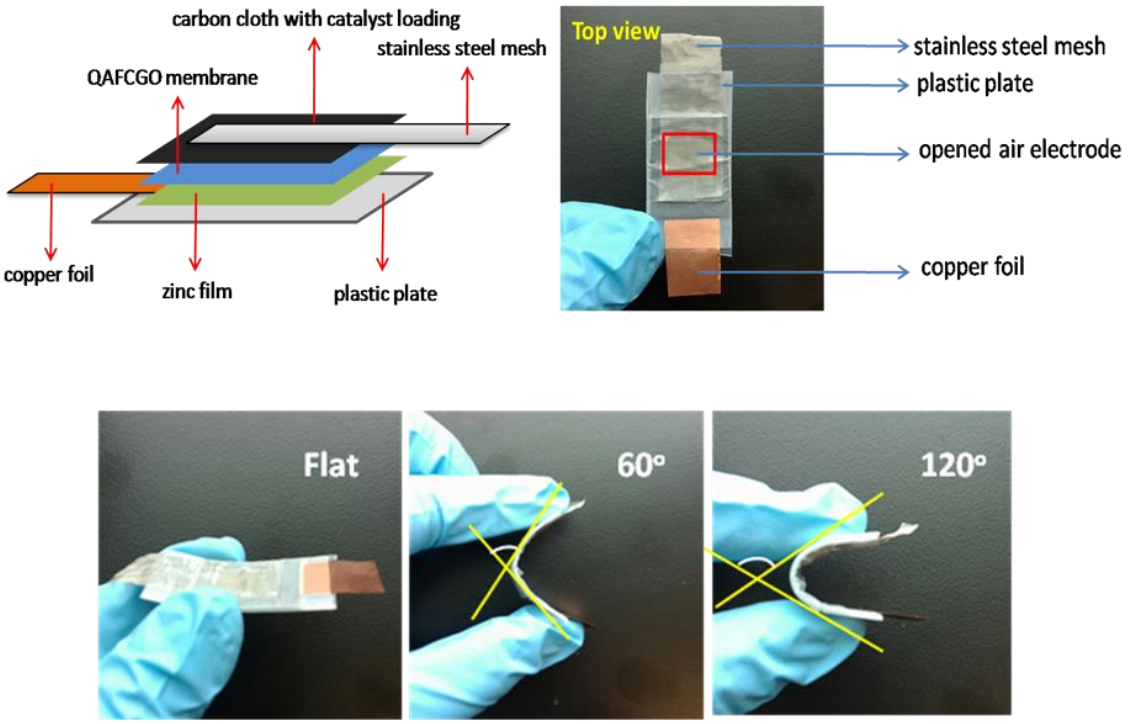

Figure 4-12. The scheme and photographs of the flexible zinc-air battery using the QAFCGO membrane under stress with different bending angles.

Based on the promising battery performance presented above, we have fabricated a flexible zinc-air battery using the QAFCGO membrane, a flexible zinc electrode and an air electrode with cobalt oxide nanoparticles loaded on a carbon cloth. As shown in **Figure 4-12**. The stainless-steel mesh and copper foil were attached respectively to the air and zinc electrode to ensure good electrical contact, and a plastic sheet was utilized as a bending substrate. As shown in **Figure 4-13**a, the application of the flexible QAFCGO-based battery is successfully demonstrated by powering an electric fan. Since in fully solid and flexible batteries, the components tend to delaminate with different bending angles, the battery resistance and the overall rechargeable performance will be affected. In order to investigate the bending effects, the galvanodynamic charge and discharge polarization and the corresponding power density are measured at 0°, 60° and 120° bending angles.

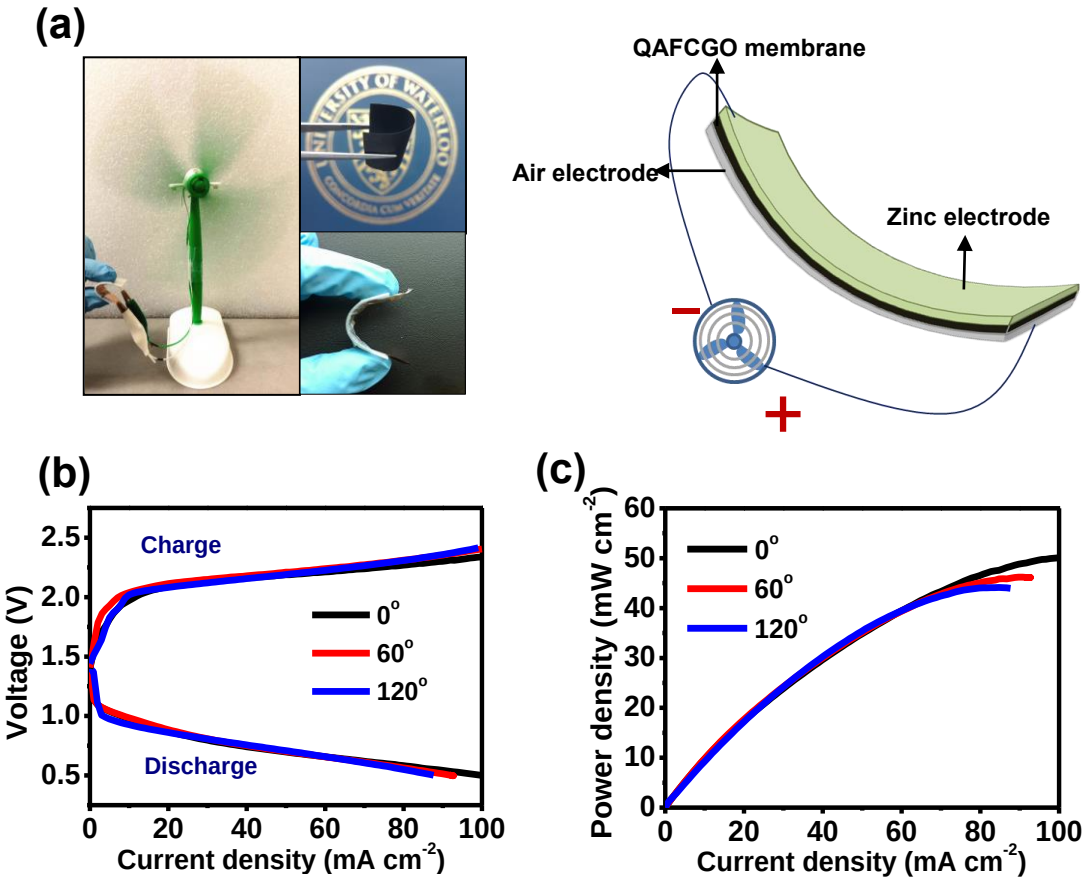

Figure 4-13. (a) Demonstration and schematic illustration images of the solid-state, flexible and rechargeable zinc-air battery. (b) Charge and discharge polarization curves of the batteries using the QAFCGO under different bending angles. (c) The corresponding power density plots of the batteries using the QAFCGO membrane under different bending angles.

As shown in **Figure 4-13**b, at any given bending angles, the charge and discharge polarization curves remain virtually uncharged even at a high current density of 80 mA cm^{-2}. This reveals not only a robust adhesion between the electrolyte membrane and the electrode but also the capability of the flexible QAFCGO membrane to maintain its high ionic conductivity under bending conditions. Only a minor loss of the output power density (i.e., 6mW cm^{-2}) is observed at a high current density of 100 mA cm^{-2} under the bending

angle of 120° (**Figure 4-13**c). At this folded region with harsh bending stress, the electrodes undergo extreme compressive deformation and the electrolyte suffers from losing water due to the shape change of the battery. In spite of this, at various bending angles, the QAFCGO-based battery exhibits significantly stable output power within current density of 60 mA cm^{-2} under stressed conditions.

4.4 Conclusions

In summary, for the first time, a functionalized nanocellulose/GO membrane with a laminated structure is developed as an effective practical hydroxide-conducting electrolyte for flexible, rechargeable zinc-air batteries. Cellulose fibers are first utilized as interconnected framework to integrate graphene oxide into a flexible membrane with high water content characteristic. Cross-linking technique is applied to guarantee its structural stability as well as low anisotropic swelling degree. In addition, the incentive for laminated crosslinked structure of the membrane with uniform and compact GO protective surface and internal layer is also to eliminate the possibility of pushing the water out of the membrane during handling or bending, and to provide good adhesion to the electrodes. The superior hydroxide conductivity of 58.8 mS cm^{-1} at 70°C was achieved after the successful functionalization. The battery using the QAFCGO membrane exhibited superior rechargeability and performance stability compared to the commercial A201 membrane. An excellent output power density was achieved when the flexible QAFCGO-based zinc-air battery under stress at different bending angles. This novel QAFCGO membrane opens up an opportunity for the development of flexible, solid-state electrochemical energy conversion and storage systems.

Chapter 5 Green Solid Electrolyte with Co-functionalized Nanocellulose/Graphene Oxide Interpenetrating Network for Fuel Cell Gas Sensor

5.1 Introduction

Gas sensors have seen a booming market owing to the ever-increasing demand of multitudinous gas detection and monitoring in industrial process, public and domestic air quality, food and drug safety, and automotive system.[184, 185] Based on different physical, chemical, and electronic mechanisms, gas sensor devices have various types including semiconducting metal oxide sensor, electrochemical sensor, optical sensor, catalytic combustion sensor, etc.[186, 187] For example, semiconducting metal oxide sensors widely exploit 2D metal oxides materials to detect target gas by physisorption and chemisorption processes originating from their enhanced surface to volume ratio and high surface area oxides. Moreover, some gasochromic oxides, such as MoO_3, WO_3 and Nb_2O_5, have sensitivity to exposed reducing gases by color changing.[188] Among all the sensors, electrochemical gas sensor, which operates by reacting with the gas of interest and outputting an electrical signal proportional to the gas concentration, has attracted much attention due to its selective, accurate and linear response for target gas components in a complex environment.[186, 189, 190] Recently, in order to overcome the aqueous electrolyte leakage problems, electrochemical gas sensor is moving towards an all-solid-state package with the requirement of portability and safety.[185, 191] Several conventional ceramic solid electrolytes have the capability to conduct ions at high temperature, and thus can be employed to construct all-solid-state gas sensors, such as yttria-stabilized zirconia (YSZ)

based oxygen sensor and sodium super ionic conductor (NASICON) based chlorine gas sensor. [190, 192, 193] However, efficient solid ion-conducting electrolyte at room temperature is still a challenge for solid electrochemical gas sensor.[190]

Cellulose, one of the most sustainable and environmentally-friendly materials on the planet, is currently widely utilized in electrochemical systems.[174, 194-196] Owing to its specific linear chain molecular structure consisting of repeated glucose units with many exposed surface hydroxyl groups, cellulose is easily chemical modified to conduct protons or hydroxide ions at room temperature, and can be applied as an ion-conducting electrolyte.[158, 197] Also, due to its hydrogen bonds and van der Walls forces between the hydroxyl groups on the surface of fibers, cellulose can be fabricated into a stable three-dimensional fibrous membrane.[1] However, because of its fibrous network structure, cellulose membrane fails to block gases flowing through its inner porous channels, resulting in unsuccessful application as solid electrolyte in electrochemical gas sensor individually. Some specific 2D materials, such as molybdenum disulfide (MoS_2), graphene, graphene oxide (GO), have relatively strong absorption or barrier performance to gas molecules, owing to their basal surfaces and prismatic edges.[198, 199] For example, MoS_2 shows a high affinity to selected model gas species because of the strong adsorption energy of gas molecules to the basal surface of 2D MoS_2.[198] Among all the 2D materials, graphene oxide (GO), which has low permeability of most gases such as methanol, ethanol, methane and carbon dioxide,[4, 190, 200] is expected to be utilized as an effective additive into cellulose-based solid electrolyte to tune its gas permeation. Moreover, due to the abundant oxygen-containing groups, GO can be covalently crosslinked with cellulose fibers and chemical

modified with a host of functional groups, [201] making it an ideal candidate material in electrochemical gas sensor applications.

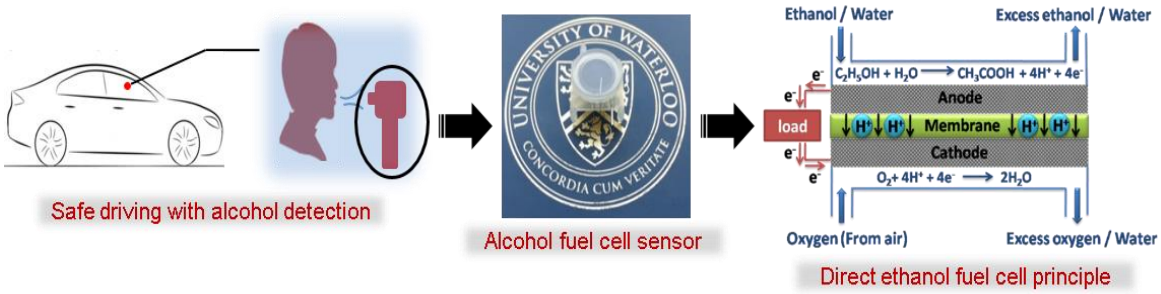

Figure 5-1. Schematic diagram of an AFCS and its electrochemical principle.

In this work, taking the advantage of the unique properties of both cellulose and GO, a co-functionalized cellulose-based membrane with GO modification was developed and applied as solid electrolyte in an electrochemical gas sensor for the detection of alcohol (ethanol). As shown in **Figure 5-1**, the ethanol gas sensor is designed on the basis of direct ethanol fuel cell principle, namely alcohol fuel cell sensor (AFCS). When the ethanol molecules diffuse into the anode, the ethanol oxidation reaction (EOR) is triggered, releasing protons and electrons. Protons travel through the solid electrolyte and react with the oxygen from the air at the cathode, undergoing oxygen reduction reaction (ORR) and generating water as the product. Transferred electrons from anode to cathode are collected as the electrical signals that could provide information on the concentration of input ethanol vapor. A promising response to the ethanol vapor was achieved for the AFCS made from co-functionalized cellulose/GO membrane, showing excellent linearity as well as sensitive response to the alcohol detection with a low limit of 25 ppm. The appreciable characteristics demonstrate a new possibility for environmentally benign cellulose based

materials utilized as ion-conducting solid electrolyte in electrochemical systems, particularly in electrochemical gas sensor.

5.2 Experimental Methods

5.2.1 Synthesis of graphene oxide

The synthesis of GO was in accordance with the improved Hummers' method.[202] First, 98% H_2SO_4 (360 mL) and 85% H_3PO_4 (40 mL) were mixed carefully in a round-bottom flask under an ice bath condition. Graphite powder (2 g) was added into the concentrated mixed acid and mechanically stirred for 1 h. Then, the strong oxidizing agent, $KMnO_4$ (18 g) was added slowly into the mixture, and the oxidation reaction was kept at 50 ºC for 16 h. The oxidation reaction was terminated by cooling down the mixture. Distilled deionized (DDI) water (400 mL) and H_2O_2 (20 mL) were added dropwise into the mixture and stirred for 30 min. Afterward, the mixture was centrifuged and washed with DDI water, 5% HCl, and ethanol respectively. Finally, the GO nanosheets were obtained by freeze-drying of GO suspension.

5.2.2 Preparation of cellulose nanofibers

The cellulose nanofibers were prepared from Northern Bleached Softwood Kraft pulp (New Brunswick, Canada) through pre-refining, enzymatic processing and nano-refining. First, the original pulp was disintegrated by using the Noram PFI mill (Quebec, Canada) with up to 30000 revolutions-per-minute. Then, an enzyme treatment is proceed with mixture of two enzymes (i.e. Mannanase and Xylanase) from Novozymes (Franklinton, USA) to gain a uniform pulp suspension. Finally, the enzyme treated pulp suspension was thoroughly washed with DDI water to remove any residues, and refined

by PFI mill again with 30000 revolutions-per-minute to produce cellulose nanofibers.

5.2.3 Fabrication of functionalized cellolose/GO membrane

In order to obtain proton conductive cellulose/GO membrane, MPTMS was applied as precursor to functionalize cellulose nanofibers and GO nanosheets with sulfonic acid groups. First, cellulose was mixed with GO in ethanol by magnetic stirring for 2 h to obtain a uniform cellulose/GO suspension. The amount of GO in mixture varied from 0%, 3%, 6% and 10% with respect to the cellulose mass. Then, MPTMS was added dropwise into the cellulose/GO mixture with mass ration of 20:1 (MPTMS:Mixture), and maintained at ambient temperature for 48 h. After washing with ethanol and DDI water to remove any unreacted trace of MPTMS, 30% H_2O_2 was added into the mixture and maintained at ambient temperature for 24 h. Afterwards, the resulting solution was centrifuged and washed with DDI water to obtain the sulfonic acid-functionalized cellulose/GO (SACGO). The resulting proton conductive cellulose/GO membrane was fabricated by vacuum filtration and then dried at 60^{o}C under vacuum for 2h.

5.2.4 Characterization and electrochemical measurement

The morphologies of cellulose nanofibers, GO nanosheets and membranes were imaged by SEM (LEO 1530) and TEM (Bruker AXS D8 Advance). The chemical and crystal structure of cellulose nanofibers, GO nanosheets and membranes were analyzed by FTIR (Avatar 320), XPS (Thermo Scientific Al Kα X-ray source) and tension testing machine (ADMET 7603-5kN). A mixed Gaussian-Lorentzian function was used while analyzing XPS peaks with a corrected Shirley background. The conductivities of membrane performed via electrochemical impedance spectroscopy (EIS) (Princeton

Versastat MC potentiostat) in frequency ranging from 100 kHz to 1 Hz with perturbation voltage amplitude of 100 mV.

5.2.5 Electrochemical gas sensor evaluation

The electrochemical gas sensor performance was evaluated by application of MEA with a series of cellulose/GO membranes. The MEA was fabricated by sandwiching the as-prepared membranes with commercial GDE (Fuelcell Etc.). The commercial GDE were coated with 60% Pt/C catalyst at a Pt loading of 0.5 mg cm^{-2} for both anode and cathode. Then, the MEA was punched into desired size and assembled into sensor housing with two Pt wires as current collectors. Before testing, the sensor housing with MEA assembled was stabilized in the humidity chamber (BTL-433) with 25℃ and RH 60% for 72 h to equilibrate the components with the desired condition. The resulting sensor housing was then inserted into the testing device to evaluate the performance. Each sample was repeated five times and the average of each parameter was taken into account.

5.3 Results and Discussions

As shown in **Figure 5-2**, 3-mercaptopropyl trimethoxysilane (MPTMS) is selected as functional precursor to conduct the functionalization. First, trimethoxysilyl groups on MPTMS are hydrolyzed and self-condensed to form the corresponding silanol oligomers intermediates. After being absorbed onto the oxygen-containing groups through hydrogen bonding, these intermediates are covalently bonded to the surface of cellulose nanofibers and GO nanosheets through the removal of water molecules. Then, the mercapto groups on the tail end of MPTMS are oxidized to sulfonic acid (SA) groups, enduing both cellulose and GO the ability to conduct protons. Lastly, the SA-functionalized mixture of cellulose

nanofibers and GO nanosheets are vacuum filtered into membrane.

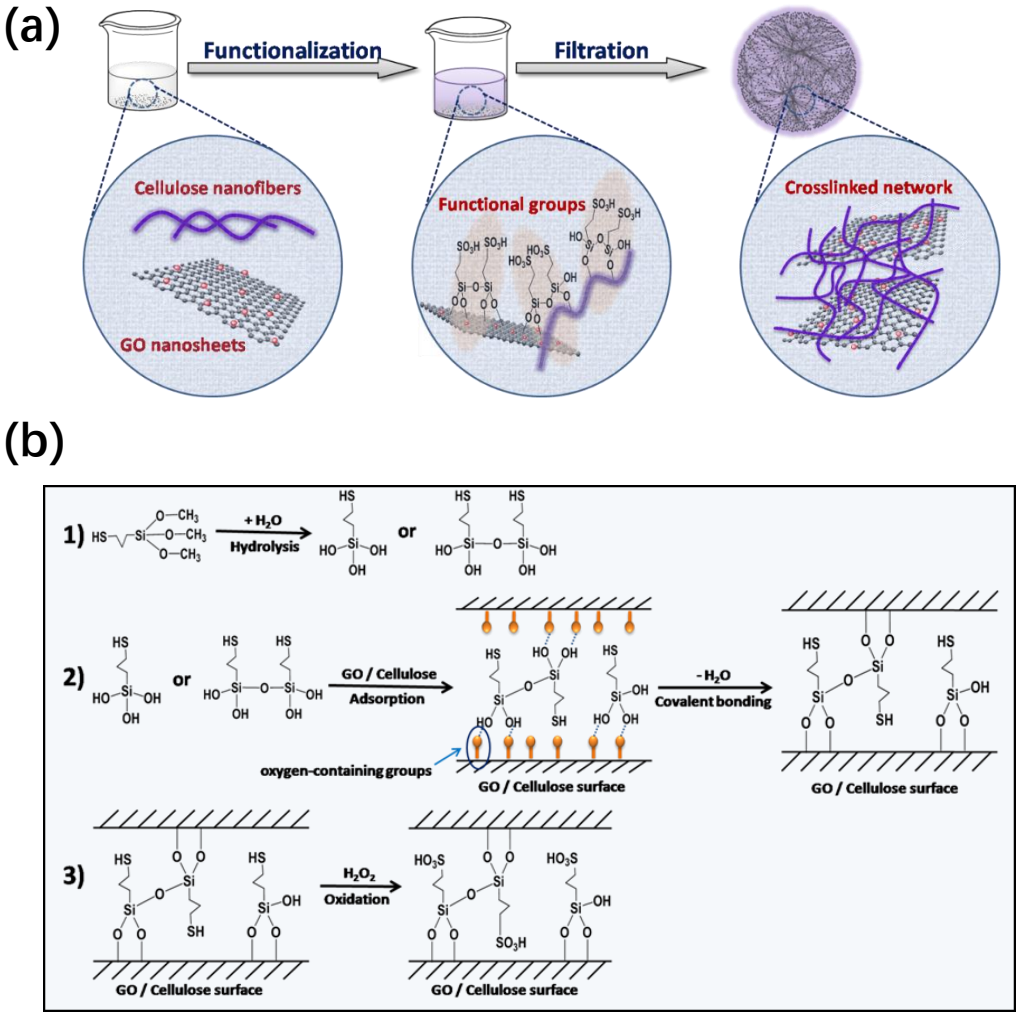

Figure 5-2. (a) Schematic diagram of the overall preparation procedure (functionalization, filtration) for the SACGO membrane. (b) Proposed three-step reaction mechanism for cellulose/GO surface functionalization with MPTMS.

As shown in **Figure 5-3** schematic illustration, the cellulose nanofibers are wrapped and covered by GO nanosheets, and reciprocally GO nanosheets are inserted into the network of cellulose nanofibers, resulting in a three-dimensional interpenetrating

network structure. The numerous cellulose nanofibers interlace into a stable network structure by hydrogen bonds and Van der Waals force,[203] giving the membrane a tough and robust skeleton. Meanwhile, the GO nanosheets are inserted into and assembled with the whole cellulose fibrous skeleton, creating barrier layers to prevent ethanol gas penetration. The TEM image (**Figure 5-4**a) shows an entangling and complex network-like structure of cellulose nanofibers. After the addition of GO, the cellulose nanofiber network is uniformly covered by the GO nanosheets (**Figure 5-4**b). The surface morphologies of membranes are further characterized by SEM. In the absence of GO, the SA-functionalized cellulose (SAC) membrane exhibits a fibrous and rough surface (**Figure 5-4**c), while the SA-co-functionalized cellulose/GO (SACGO) membrane shows a dense and smooth surface (**Figure 5-4**d) due to the coverage of GO nanosheets within this cellulose-based system.

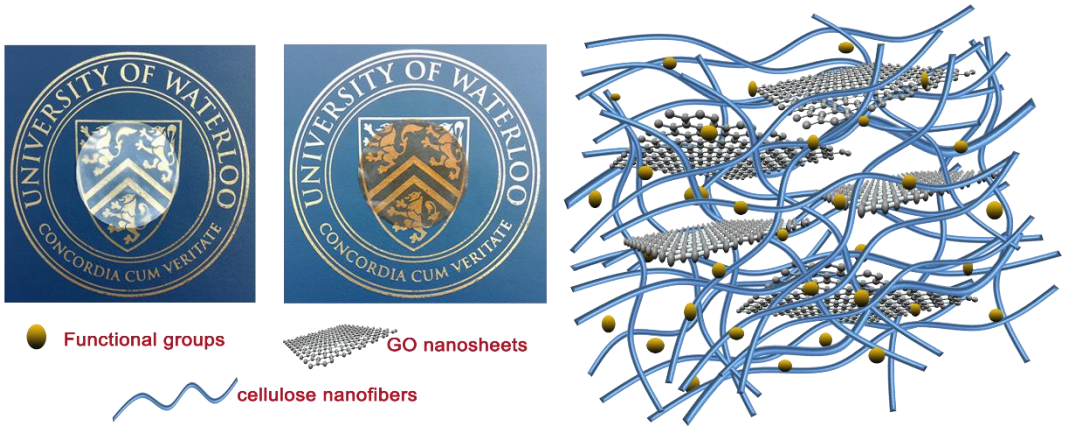

Figure 5-3. Photographs of SAC and SACGO membranes, and schematic illustration of SACGO membrane's inner three-dimensional interpenetrating structure.

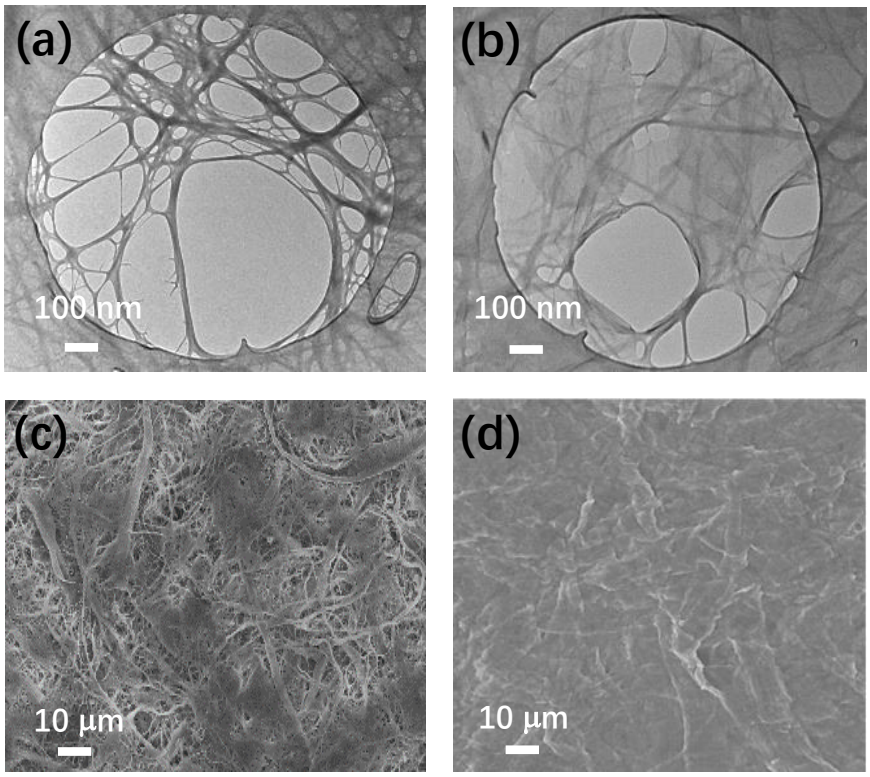

Figure 5-4. (a) A TEM image of cellulose nanofibers. (b) A TEM image of cellulose nanofibers wrapped and covered by GO nanosheets. (c) A SEM image of SAC membrane with a fibrous network surface. (d) A SEM image of SACGO membrane with a flat and dense surface (SACGO membrane here indicates the cellulose matrix mixing with 6% weight percentage of GO, i.e. 6-SACGO).

To confirm the successful sulfonic acid functionalization reaction, Fourier transform infrared (FT-IR) spectra of non-functionalized cellulose/GO (CGO) membrane and SACGO membrane are compared in **Figure 5-5**a. In the spectrum of CGO membrane, the peak at 3344 cm^{-1} is assigned to vibration-stretching hydroxyl groups, while peak occurred at 2900 cm^{-1} is assigned to vibration-stretching of C-H.[204] Small peaks at 1300-1450 cm^{-1} region are corresponding to the HCH and OCH in-plane bending vibration, C-H in-plane bending and CH_2 rocking vibration of cellulose.[205] The representative peaks located around 1037-1162 cm^{-1} are due to C-O stretching and C-O-C asymmetric vibration.

The glucose ring stretching produces two peaks at 1112 and 898cm^{-1}. [204, 206] After functionalization, the FT-IR spectrum of SACGO membrane reveals relatively weakened assigned peaks of O-H stretching, C-O-C vibration, and C-O stretching, which indicates the successful grafting reaction between the oxygen-containing groups on cellulose/GO and MPTMS. Alternatively, a new small peak at 809 cm^{-1} emerges in the spectrum, owing to the vibration of Si-O-C in the silane groups of the functional precursor MPTMS.[190, 207]

The X-ray photoelectron spectroscopy (XPS) analysis of CGO and SACGO membrane is carried out to complement the FT-IR results. The structural changes are analyzed by high-resolution spectra of C 1s, where five different peaks before functionalization are deconvoluted in **Figure 5-5**b, namely O-C=O (289.1 eV), O-C-O (287.9 eV), C-O-C (287.2 eV), C-O (286.5 eV), C-C/C-H (284.9 eV).[190, 208, 209] Similarly, after functionalization, the C 1s spectra of SACGO membrane also shows these five characteristic peaks (**Figure 5-5**c), but the peak intensity of C-O-C significantly decreases, which is in agree with the results of FT-IR, indicating the successful reaction between oxygen-containing groups of cellulose/GO and MPTMS. Meanwhile, a new peak at 285.6 eV assigned to C-S, C-O-Si of the grafted precursor MPTMS emerges,[210, 211] indicating the presence of the SA functional groups on the surface of cellulose nanofibers and GO nanosheets, corroborating our perious FT-IR results.

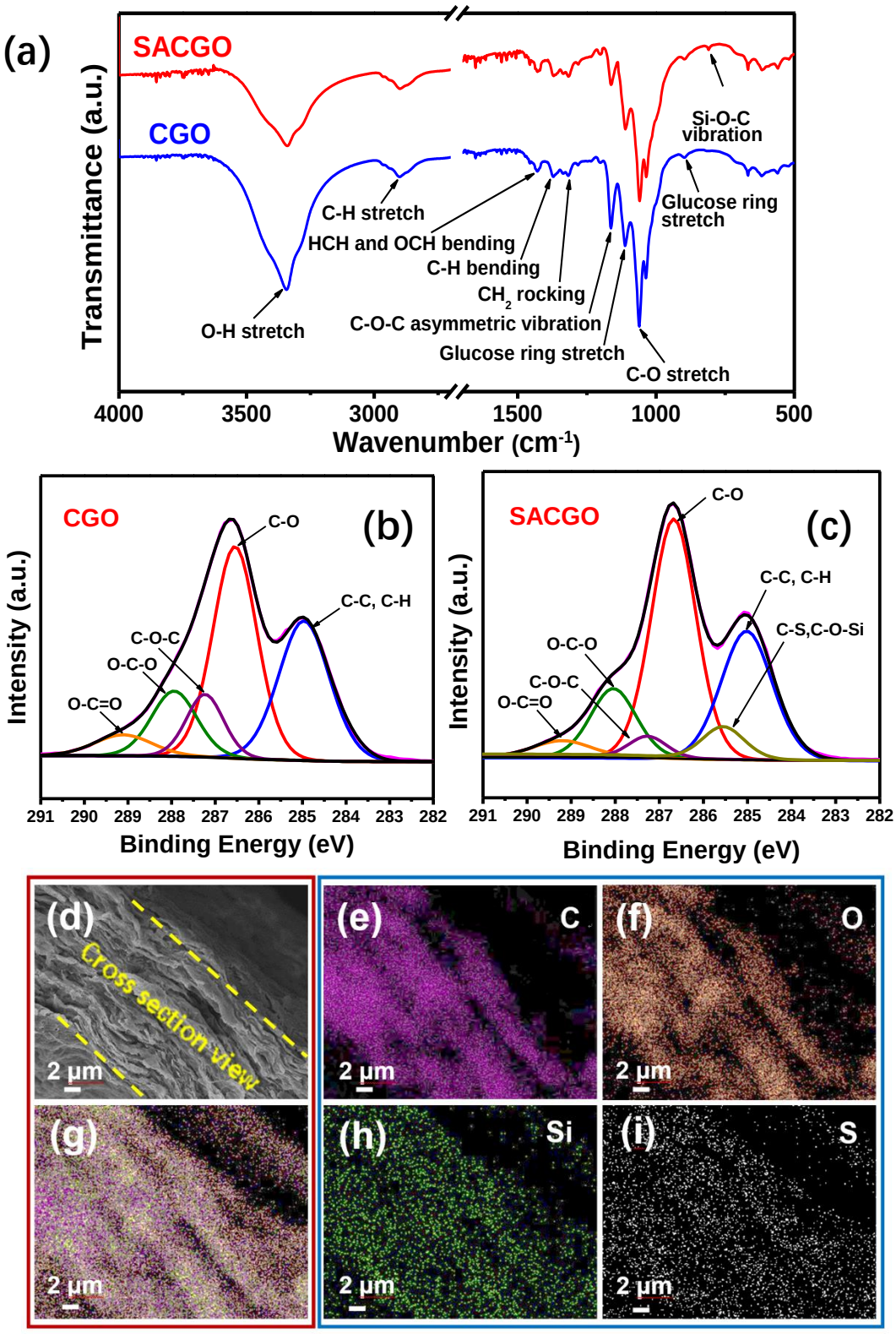

Figure 5-5. (a) FT-IR spectra. (b-c) Deconvoluted XPS spectra in the C 1s region of CGO and SACGO membranes. (d) Cross-sectional SEM image of SACGO membrane. (e–i) EDX mapping images of the cross-section of SACGO membrane (SACGO membrane here indicates the cellulose matrix mixing with 6% weight percentage of GO, i.e. 6-SACGO).

To further elucidate the existence and distribution of the grapted functional groups on cellulose and GO surface, a cross-sectional energy-dispersive X-ray spectroscopy (EDX) mapping of SACGO membrane is exhibited in **Figure 5-5**e-i. It can be found that elements Si and S (contained in the silane and sulfonic acid moieties of the graphted groups) with C and O are homogeneously distributed through the thickness of the membrane, indicating the successful functionalization in SACGO membrane. From the SEM cross section view of SACGO membrane (**Figure 5-5**d), a three-dimensional layered structure is observed through SACGO membrane. The typical structure of membrane has been proved to be effective to tune the ionic conductivities through the control of water uptake and ion transport channels.[158, 197]

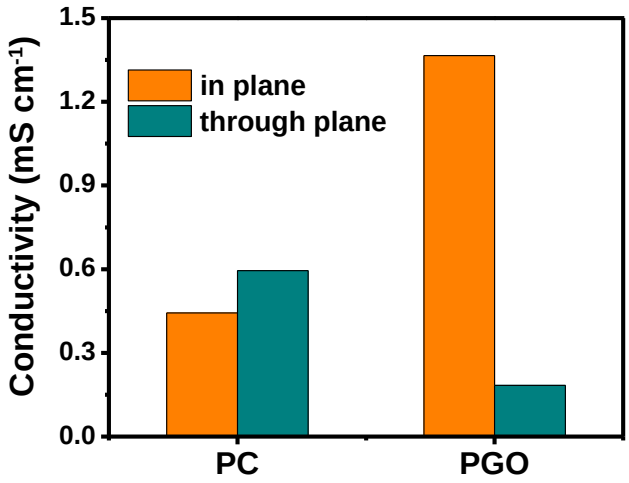

Figure 5-6. In-plane and through-plane conductivity of PC and PGO membrane (PC: pristine cellulose; PGO: pristine graphene oxide without functionalization).

In consideration of proton conductivity value (σ), it is important to note that, proton conductivity is commonly measured along the plane of the membrane, i.e. in-plane proton conductivity.[212, 213] However, in practice, the proton conductivity perpendicular to the

membrane, i.e. through-plane proton conductivity, is much more relevant for most applications.[214] Different membrane casting methods and membrane pre-treatment procedure could lead to morphological anisotropy and hence result in anisotropic ionic conductivity.[212] Therefore, relying only on in-plane conductivity to estimate the ion transportation ability is inaccurate in case of membrane exhibiting morphological anisotropy. In this work, in order to study the in-plane and through-plane proton conductivity for cellulose and GO composite system, the membranes were prepared by mixing 3%, 6% and 10% weight percentage of GO into cellulose matrix, donated as 3-SACGO, 6-SACGO and 10-SACGO. As shown in **Figure5-7**a, the in-plane conductivity (8.73 mS cm^{-1}) of SAC membrane is significantly improved compared to that of the non-functionalized pristine cellulose (PC) membrane (0.44 mS cm^{-1}, **Figure 5-6**), indicating the successful graft of SA groups onto cellulose nanofibers. With further addition of GO into cellulose matrix, the in-plane conductivity gradually raises up to 26.86 mS cm^{-1} (10-SACGO membrane), which means that the existence of SA-functionalized GO facilitates the migration of protons along the plane of the membrane. That is because GO exhibits effective ionic conductivity along the surface of 2D nanosheets. Meanwhile the insertion of SA-functionalized GO into cellulose nanofiber network could form opened and layered ion transport channels along the membrane inner structure.[215] Similarly, as shown in **Figure 5-7**b **and 5-6**, the through-plane conductivity of SAC membrane is also remarkably higher than that of non-functionalized PC membrane (9.07 *vs.* 0.59 mS cm^{-1}). However, with increasing GO weight percentage into cellulose matrix, the through-plane conductivity exhibites a gradual descending trend from 9.07 (SAC membrane) to 3.21 mS

cm^{-1} (10-SACGO membrane). The decrease of through-plane conductivity is mainly due to the GO nanosheets self-assembly along the plane that blocks the ion transportation through the direction of the thickness.[216]

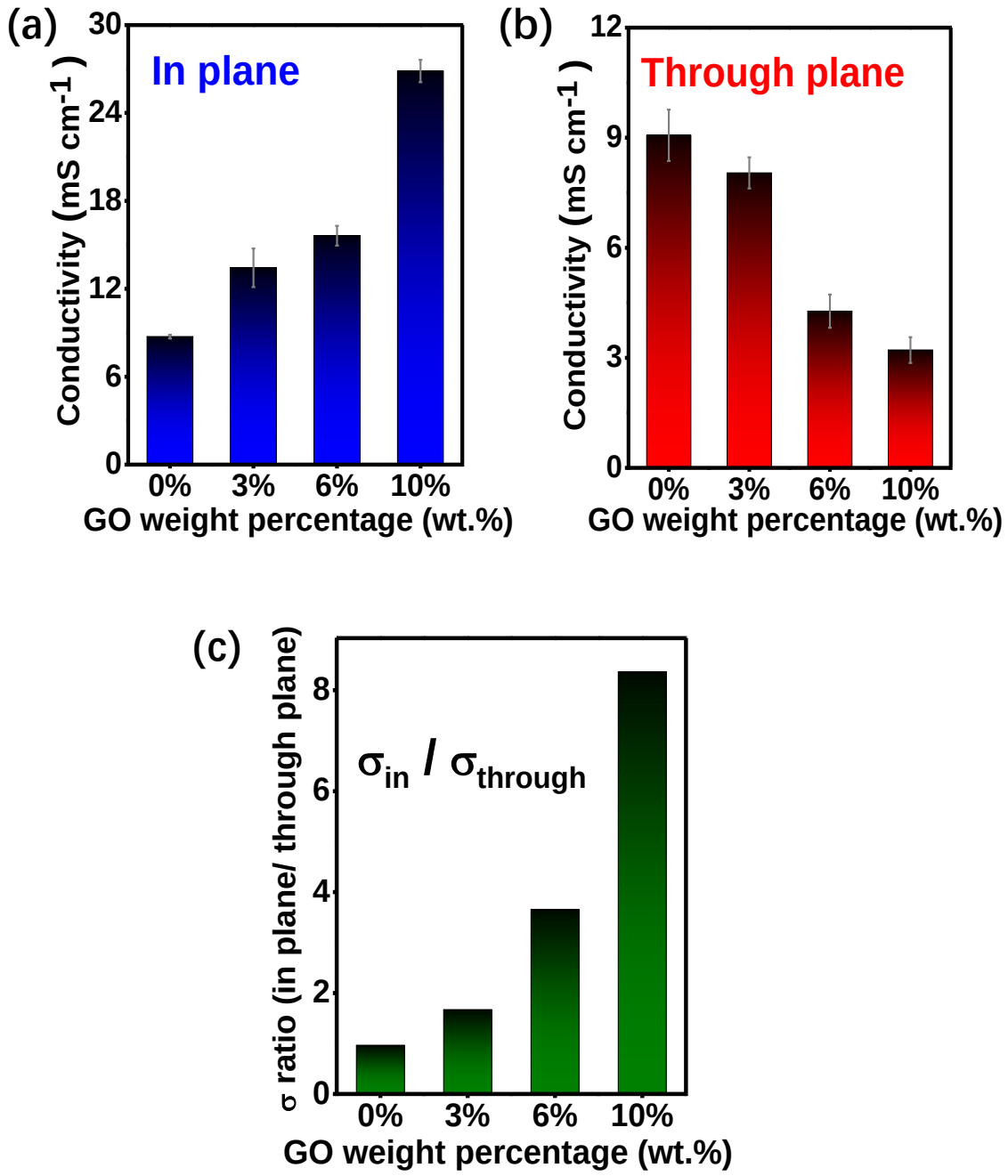

Figure 5-7. (a) In plane and (b) through plane proton conductivities of the SAC and SACGO membranes. (c) Anisotropic conductivity values of SAC and SACGO membranes.

In order to further investigate the protons transportation, the anisotropy values of cellulose/GO membranes are calculated and exhibited in **Figure 5-8** according to the ratio of in-plane to through-plane conductivities. The SAC membrane exhibits isotropic characteristic with anisotropy value of 0.96, indicating that the protons can almost be transported equally in both horizontal and vertical directions, and allowed to move freely in the membrane (**Figure 5-8**(1)). However, after the addition of SA-functionalized GO, the in-plane conductivities of 3-SACGO and 6-SACGO membranes are obviously higher compared to those of through-plane counterpart with the anisotropy value of 1.67 and 3.66, respectively. This anisotropic ionic conductivity is mainly due to the insertion of SA-functionalized GO into the cellulose nanofiber network, which creates proton transportation channels along the plane of the membrane as well as the impermeable blocking layers that limit the protons to transport through the thickness of the membrane (**Figure 5-8**(2)). Particularly, for 10-SACGO membrane, the in-plane conductivity exceeds its through-plane counterpart by eight times higher, in which the SA-functionalized GO layers stack within the cellulose matrix causing a huge impediment for protons transporting across the membrane but fast proton transportation channels along the GO nanosheets (**Figure 5-8**(3)). Therefore, the excess addition of GO into cellulose matrix (e.g. 10-SACGO membrane) is not suitable for practical applications because of the dramatic decrease of through-plane conductivity.

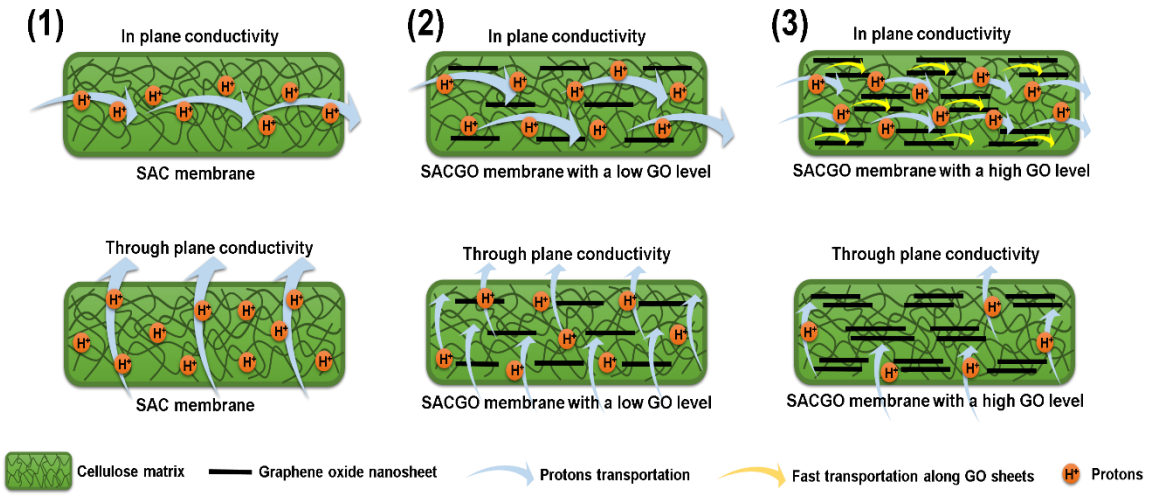

Figure 5-8. A schematic illustration of ion transport mechanism with SAC and SACGO membranes with different GO additive levels.

Water uptake of the membrane is a critical factor for proton conductivity. In the presence of water molecule, protons can be dissociated from the grafted SA groups and then hydrated into oxonium ions.[190] With the aid of oxonium ions, protons can be passed along the hydrogen bonds, or directly transports as a moving H_3O^+ "vehicle".[29, 30, 32] Accordingly, water molecule is indispensable during ion transportation, and high water uptake would be favourable for ionic conductivity. As shown in **Figure 5-9**, the water uptakes of the cellulose/GO membranes are around 90%, which is obviously higher than that of the commercial proton-conducting Nafion membrane (34.5%).[217, 218] That is owing to the excellent hydrophilic nature of cellulose nanofibers and the fibrous and porous network of the membrane which play an important role in absorbing and retaining water within the internal structure.[158] In consequence, the high water uptakes of these cellulose/GO membranes assist protons in moving along and through the plane of

membrane, resulting in promising ionic conductivity.

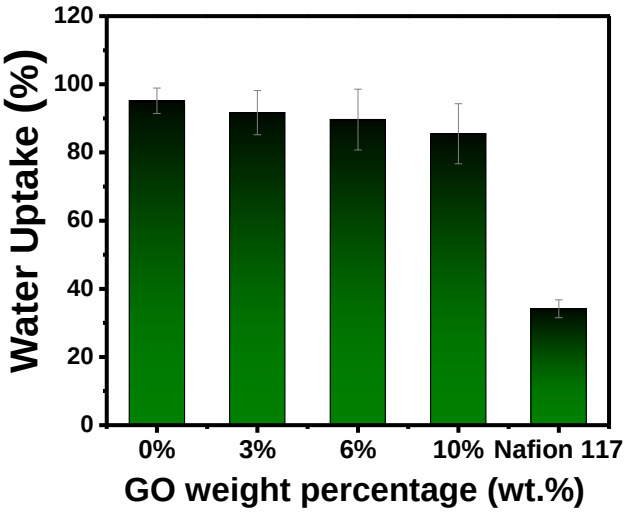

Figure 5-9. Water uptakes of SAC, SACGO membranes, and commercial Nafion 117.

The practical performance of the cellulose/GO membrane as solid electrolyte for AFCS is demonstrated in a setup consisting of flow meter, water trap, alcohol simulator, sensor, data logger, and computer analyzer (**Figure 5-10**). The core component of sensor is membrane electrode assembly (MEA), in which the membrane is sandwiched between two commercial gas diffusion electrodes (GDEs) loaded with Pt/C catalyst. In order to mimic the relative temperature and humidity of human breath, a constant of air is pumped through the alcohol simulator. Then a certain concentration of ethanol vapor will be carried out with the air and enter into the sensor. In the sensor, the ethanol vapor is sampled, and the electrochemical reaction occurs. Next, the electrical signal is generated, collected, and finally analyzed in the terminal computer, outputting a typical response current curve characterized by four different parameters, namely response time, recovery time, peak height and peak area. In theory, peak area corresponds to the quantity of transferred

electrons which is in proportion to the amount of reacted ethanol molecules. Accordingly, the ethanol concentration shows a linear relationship with the peak area, and can be used for calculating by Equation (5-1)

$$c = \frac{A_{peak}}{nFV} \tag{5-1}$$

where c is the ethanol concentration in the vapor, A_{peak} is the peak area, n is the number of transferred electrons in the electrochemical reaction, F is the Faraday constant, and V is the fixed volume of ethanol vapor sampled into the sensor.

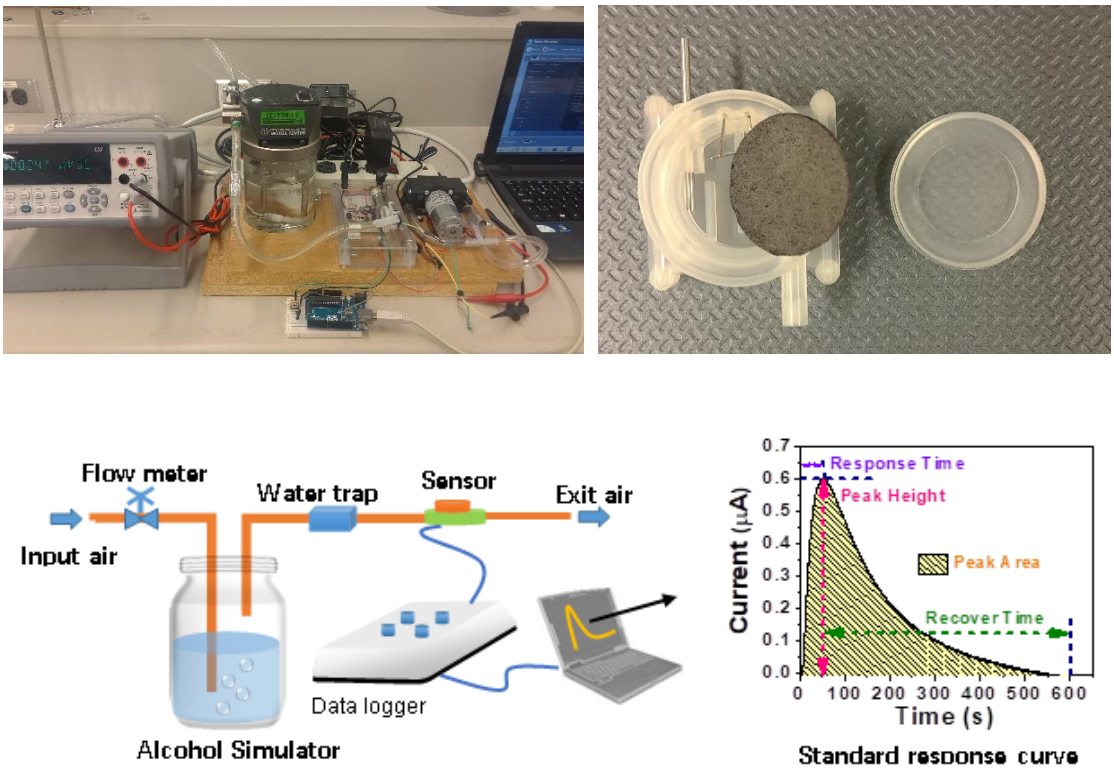

Figure 5-10. Photographs of sensor testing setup and housing with MEA, and diagram of the experiment set-up and typical response curve for sensor testing.

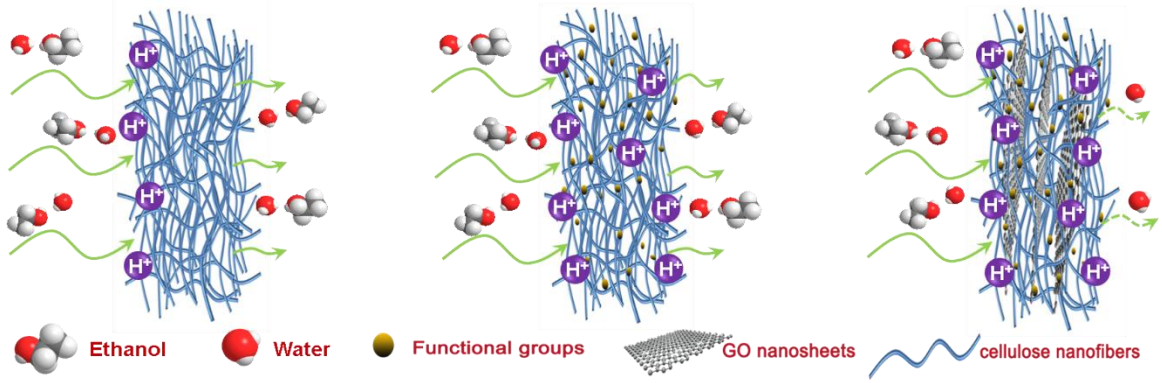

Figure 5-11. The schematic of protons and ethanol vapor transportation in cellulose/GO membrane.

In **Figure 5-13**a, the performance of sensors made from non-functionalized PC, SAC and SACGO membranes are tested in ethanol standard solution equivalent to blood alcohol concentration (BAC) of 50 mg dL^{-1}. BAC is defined as the number of milligrams of alcohol per 100 mL of blood. Evidently, the SACGO membrane has the highest peak area and peak height among these three membranes, indicating its potential application in AFCS. Compared to the PC, the SAC membrane with functionalized sulfonic acid groups can easily conduct protons in its inner structure, resulting in higher sensitivity to ethanol. However, as shown in **Figure 5-11**, the residual ethanol vapor after electrochemical reaction may pass through the SAC membrane from the anode to cathode because of its porous network structure, and finally causing the gas permeates problem. Therefore, with the addition of SA-functionalized GO which is less permeable to most gases, the SACGO membrane exhibits better sensor performance due to its resistance to ethanol vapor mass transfer. After 30 days, the SACGO membrane-based sensor shows an almost unchanged response curve from its initial test, demonstrating its excellent stability (**Figure 5-13**b).

Additionally, in **Figure 5-13**c, the sensor prepared form SACGO membrane can effectively respond to an ethanol standard solution equivalent to BAC of as low as 10 mg dL^{-1}, corresponding to the detection limit of 25 ppm ethanol in human breath. The peak area of SACGO based sensor is also calculated as a function of different concentrations of ethanol standard solution, which shows great linearity (**Figure 5-13**d). Selectivity is another critical issue for gas sensor. In order to further investigate selectivity performance, The SACGO based sensor was tested in response to water, ethanol, and acetone vapor in the equal liquid concentration. As shown in **Figure 5-12**, the SACGO based sensor demonstrates excellent selectivity of ethanol over water and acetone. Virtually, no response curves of water and acetone were observed, but obvious ethanol response was detected in the same concentration.

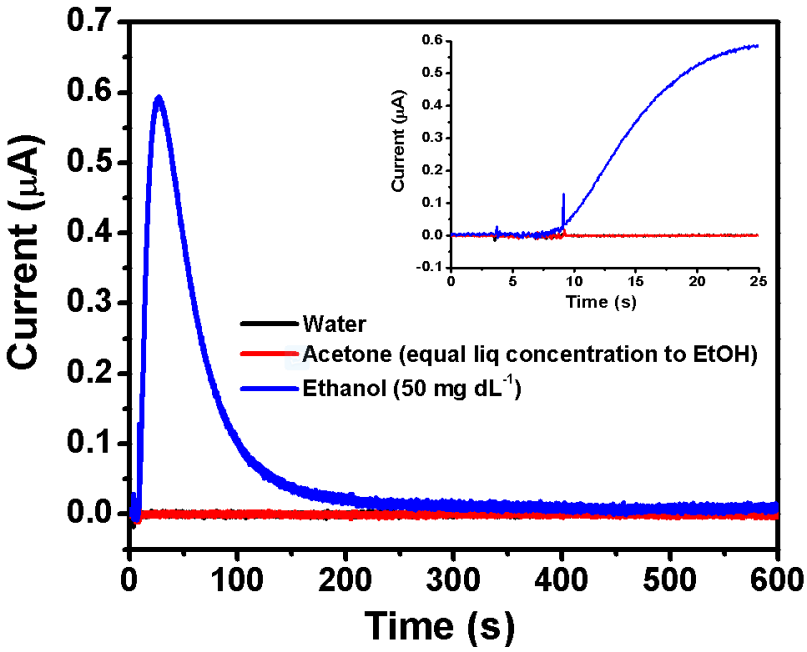

Figure 5-12. Response curves of SACGO-based sensor to water, ethanol and acetone vapors from standard solutions of the same concentration.

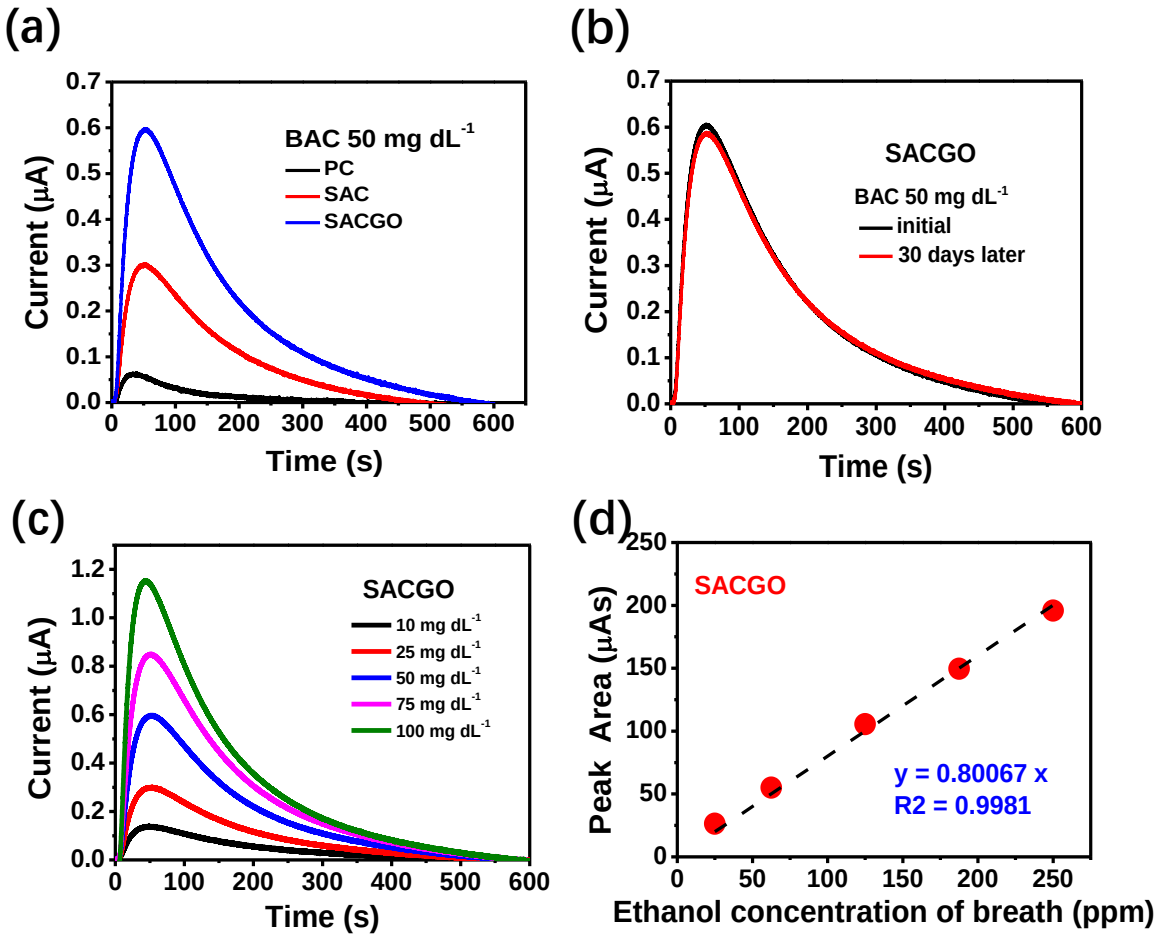

Figure 5-13. (a) Response curves of sensor employing PC, SAC and SACGO membrane. (b) The initial and 30-days-after response curves of SACGO-based sensor to the ethanol vapor from standard solution equivalent to BAC of 50 mg dL-1. (c) Response curves of SACGO-based sensor to the ethanol vapor from different standard solutions. (d) The peak areas obtained from response curves versus ethanol concentration in the vapor (SACGO membrane here indicates the cellulose matrix mixing with 6% weight percentage of GO, i.e. 6-SACGO).

5.4 Conclusions

In conclusion, for the first time, a co-functionalized cellulose-based proton-conducting membrane with GO modification is fabricated and successfully applied as solid electrolyte in an electrochemical gas sensor for the dection of alcohol. Both promising in-plane and through-plane conductivities as well as high water retention within the three-dimensional interpenetrating network structure are achieved for SACGO membrane as an effective proton-conducting solid electrolyte, indicating successful graft of sulfonic acid groups onto cellulose and GO surface. An AFCS set-up is created and further demonstrated the promising electrochemical performance of cellulose/GO membrane, where stable and linear response curves to ethanol vapor are obtained with the ethanol detection limit of as low as 25 ppm. Therefore, this novel concept of cellulose/GO system in this work will open a possible route for the development of ion-conducting solid electrolyte in electrochemical device, particularly in electrochemical gas sensor. In conclusion, for the first time, a co-functionalized cellulose-based proton-conducting membrane with GO modification is fabricated and successfully applied as solid electrolyte in an electrochemical gas sensor for the dection of alcohol.

Chapter 6 Conclusion and future work

6.1 Conclusions

In this thesis, approaches to hybrid aqueous electrolyte design (Chapter 3) and multifunctional solid electrolyte design (Chapter 4 and 5) were successfully implemented to develop a high-energy-density flow battery, a rechargeable and flexible zinc-air battery, as well as a micro fuel cell alcohol sensor.

In Chapter 3, the present work deals with a novel strategy towards an all-aqueous redox flow battery with unprecedented high energy density. In these years, the improvement of high energy density for all-aqueous redox flow battery is burgeoning. In 2015, Li et al. reported a promising high energy density (167 Wh L^{-1}) zinc-polyiodide all-aqueous flow battery. Last year, Weng et al. reported a zinc/iodine-bromide battery to achieve an energy density of 202 Wh L^{-1}, which is the highest energy density achieved for aqueous flow batteries as ever reported. In this present work, we demonstrate an all-aqueous hybrid alkaline zinc/iodine flow battery achieving a high-energy-density of 330.5 Wh L^{-1}. It is an unprecedented record for an all-aqueous redox flow battery obtained to date, which is even 1.6 times of the highest reported energy density value. Theoretically, the electrolyte acidic/basic properties have a great influence on redox pair potential. By tuning the pH of electrolyte, the battery voltage can be effectively enhanced, finally leading to an increase in energy density. Inspired by this concept, an all-aqueous hybrid alkaline zinc/iodine flow battery is designed and demonstrated with an unprecedented high-energy-density as well as a 0.47 V battery potential enhancement compared to the conventional counterpart.

Meanwhile, this hybrid zinc/iodine redox flow battery also exhibits a promising cycling performance with 100% coulombic efficiency, ~ 70% voltage and energy efficiency in 200 h. Overall, this hybrid alkaline zinc/iodine system demonstrates a new design with promising performance for an all-aqueous redox flow battery, and more importantly, opens a feasible and effective approach for achieving high-voltage high-energy-density all-aqueous electrochemical energy device.

In Chapter 4, the present work deals with a functionalized nanocellulose/graphene oxide membrane with a laminated structure to be used as a hydroxide-conducting solid-state electrolyte in flexible and rechargeable zinc-air batteries. The introduced functional groups in the graphene oxide and nanocellulose significantly boost the hydroxide conductivity (e.g., 58.8 mS cm^{-1} at 70°C) due to the enhanced ion-exchange capacity and the increased amorphousness of the membrane. Meanwhile, a cross-linking bonding network is formed between the functionalized graphene oxide and nanocellulose, providing the membrane with a superior mechanical property and excellent water retention. This modification facilitates the ion transport during the battery operation, particularly under the stress of bending conditions. A rechargeable solid-state zinc-air battery prototype is fabricated using the novel electrolyte membrane, exhibiting superior charge and discharge performances and output power density compared to the battery using the benchmark commercial alkaline anion-exchange membrane (A201, Tokuyam, Japan). Most importantly, under extreme bending conditions, the flexible zinc-air battery maintained not only its superior flexibility but also the high power density during the discharge and charge process.

In Chapter 5, the present work deals with a co-functionalized nano-

cellulose/graphene oxide membrane with three-dimensional interpenetrating structure to be used as a proton-conducting solid-state electrolyte in an electrochemical gas sensor for the detection of alcohol. This solid electrolyte was fabricated through a green, efficient and scalable approach. The numerous cellulose nanofibers interlace into a stable network structure by hydrogen bonds and Van der Waals force, giving the membrane a tough and robust skeleton. Meanwhile, the graphene oxide nanosheets are inserted into the whole cellulose fibrous skeleton, creating impermeable barrier layers to prevent ethanol gas penetration. The introduced functional groups in the nanocellulose and graphene oxide significantly boost the proton conductivity due to the enhanced ion-exchange capacity. Importantly, the modification of GO facilitates the protons transportation in both in-plane and through-plane channels of the membrane. An alcohol fuel cell sensor equipped with the novel electrolyte membrane was fabricated on the basis of direct ethanol fuel cell principle, exhibiting excellent linearity, sensitivity as well as low ethanol detection limits approaching 25 ppm.

6.2 Recommended future work

Based on the results from the studies conducted in this thesis research, the following recommendations are proposed for future work.

(1) *Further development on the separator membrane of Zn iodide flow battery.* In Chapter 3, the loss of capacity of the presented zinc iodide flow battery is discussed, and electrolyte crossover issue is the one of the main causes of the problem. The cationic exchange Nafion membrane is assembled between anode and cathode. Theoretically, the movements of any existing anions $Zn(OH)_4^{2-}$, I_3^-, and I^- are resisted, whereas K^+ ions as

mediator can smoothly shuttle between two electrodes to conduct the charges in the battery. However, as illustrated by EDX results, Zn and I elements are present on both sides of the membrane, indicating that the electrolyte crossover issue exists in this system. That is because Nafion membrane is a hydrophilic polymer which conducts ions with the assistance of water molecules. Inevitably, a small number of hydrated anions will still pass through the membrane along with water molecules. Thus, a small amount of undesired hydrated $Zn(OH)_4^{2-}$, I_3^-, and I^- ions are able to go across the membrane, which finally results in the loss of some battery capacity. To overcome this issue, a new design of separator membrane should be proposed to replace the Nafion membrane in this system. Here, three suggested points can be taken into consideration for the development of separator membrane: i) anion group functionalization. In this system, K^+ ions as mediator should smoothly shuttle between two electrodes to conduct the charges in the battery. Thus, anion group functionalization is essential to provide abundant positive conducting sites for the movement of K^+ ions. ii) hydrophilic modification. In order to prevent undesired hydrated ions moving accompanied by water molecules, hydrophilic modification should be conducted on the separator membrane to eliminate the ions crossover issue. iii) 2D structure inorganic nanofillers can be incorporated into the membrane system to tune the ion transportation pathway, thereby facilitating the movement of K^+ ions and blocking the negative charged ions crossover as well.

(2) *Further investigation on zinc dendrite suppression for zinc-based batteries.* Zinc dendrite is one of the major phenomena to limit the performance of zinc electrode, which is formed during electrodeposition as sharp and needle-like metallic protrusions. In

rechargeable zinc-based batteries, the zinc dendrites form during the charging process and will bring out two major drawbacks, i.e. capacity loss and short circuit. Firstly, the sharp and needle-like protrusions are easily to break, resulting in fracture and disconnection from electrode and finally leading to capacity loss. Secondly, the sharp zinc dendrites have the possibility to puncture the separator membrane and cause the short circuit issue. Particularly, for solid-state zinc air battery, the solid electrolyte membrane serves as separator as well, and the two electrodes are only separated and closely touched with the membrane, which has large risk of short circuit if zinc dendrite forms. To overcome this issue, special solid electrolyte or separator should be designed with the ability to recover from zinc dendrite formation. Here, a new strategy of self-healing membrane has been put forward to solve this problem. As shown in **Figure 6-1**[219], a conventional membrane was fabricated by embedding microcapsules with an isophorone diisocyanate core. When the membrane suffers from physical damage, the microcapsules will release a reactive isocyanate healing agent which can form a polyurea matrix that plugs the damage. This kind of microcapsule-embedded self-healing membranes are a promising approach to fabricating versatile, next-generation membranes for zinc-based batteries.

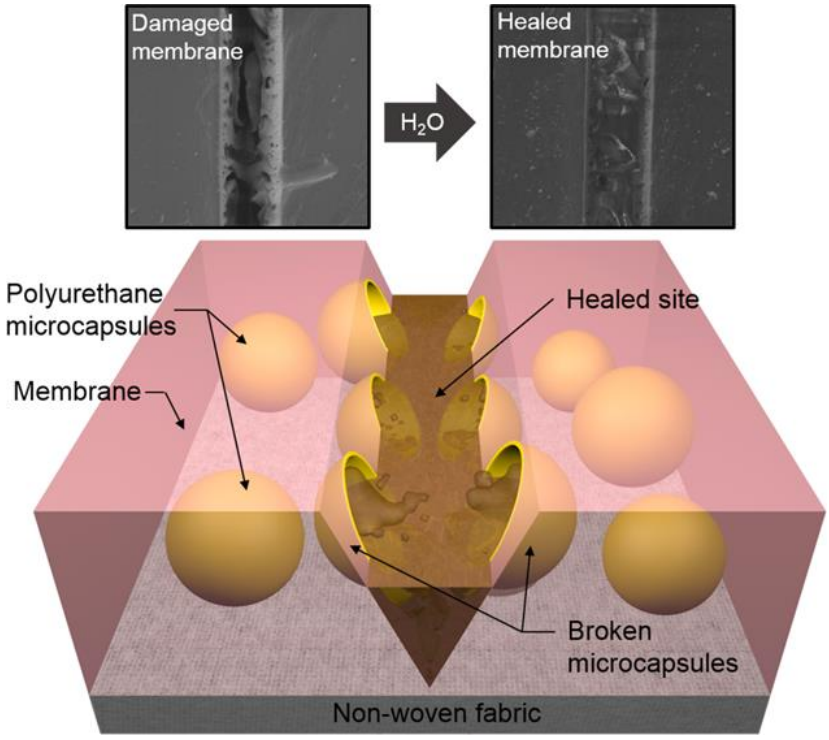

Figure 6-1. Schematic illustration of the self-healing process of microcapsule-embedded membranes. Reprinted with permission from reference 219, with permission of American Chemical Society.

(3) *Further design to solve electrode/electrolyte interfacial issue for solid-state flexible electrochemical devices.* In the solid configuration, the interfacial property between the solid electrolyte and a pair of electrodes is a big challenging. In aqueous system, the electrodes are totally wetted by liquid electrolyte, facilitating a three-phase reaction zone. In contrast, in solid-state system, the interfacial reactions are largely limited by the solid "dry" electrolyte membrane. Thus, the interfacial resistance of solid system is largely higher than that of liquid one. Particularly, for some flexible and bendable devices, at some folded regions with harsh bending stress, the electrodes undergo extreme compressive deformation and the electrolyte suffers from losing water due to the shape

change of the battery, resulting in the loss of battery performance. In response to this problem, an idea of all-in-one piece of flexible device with integration of electrode and electrolyte is proposed. As shown in **Figure 6-2**, one-piece flexible zinc-air battery is designed instead of the conventional individual components. To achieve this target, an ionic liquid material could be use to fabricate a solid electrolyte, meanwhile the ionic liquid can also be applied as ionomer for both zinc and air electrodes. The ionic liquid are entirely permeable in electrolyte and electrodes, making them one integrated piece.

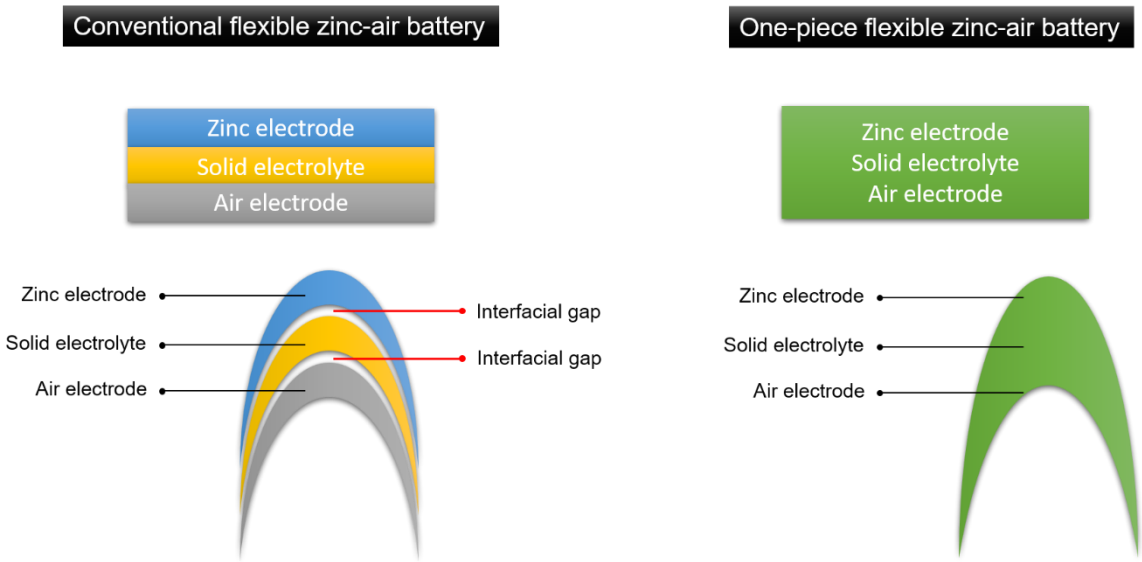

Figure 6-2. Schematic illustration of one-piece flexible zinc air battery.

References

1. G. Glenk and S. Reichelstein, *Nature Energy*, 2019.
2. J. Liu, Z. Bao, Y. Cui, E. J. Dufek, J. B. Goodenough, P. Khalifah, Q. Li, B. Y. Liaw, P. Liu, A. Manthiram, Y. S. Meng, V. R. Subramanian, M. F. Toney, V. V. Viswanathan, M. S. Whittingham, J. Xiao, W. Xu, J. Yang, X.-Q. Yang and J.-G. Zhang, *Nature Energy*, 2019.
3. S. Chu and A. Majumdar, *Nature*, 2012, **488**, 294-303.
4. J. Jewell, D. McCollum, J. Emmerling, C. Bertram, D. Gernaat, V. Krey, L. Paroussos, L. Berger, K. Fragkiadakis, I. Keppo, N. Saadi, M. Tavoni, D. van Vuuren, V. Vinichenko and K. Riahi, *Nature*, 2018, **554**, 229-233.
5. K. J. Griffith, K. M. Wiaderek, G. Cibin, L. E. Marbella and C. P. Grey, *Nature*, 2018, **559**, 556-563.
6. D. K. Bediako, M. Rezaee, H. Yoo, D. T. Larson, S. Y. F. Zhao, T. Taniguchi, K. Watanabe, T. L. Brower-Thomas, E. Kaxiras and P. Kim, *Nature*, 2018, **558**, 425-429.
7. M. Kuhne, F. Borrnert, S. Fecher, M. Ghorbani-Asl, J. Biskupek, D. Samuelis, A. V. Krasheninnikov, U. Kaiser and J. H. Smet, *Nature*, 2018, **564**, 234-239.
8. M. Winter and R. J. Brodd, ACS Publications, 2004.
9. P. Simon and Y. Gogotsi, *Nature materials*, 2008, **7**, 845.
10. T. Christen and M. W. Carlen, *Journal of power sources*, 2000, **91**, 210-216.
11. B. Smitha, S. Sridhar and A. A. Khan, *Journal of Membrane Science*, 2005, **259**, 10-26.
12. J. Cheng, G. He and F. Zhang, *International Journal of Hydrogen Energy*, 2015, **40**, 7348-7360.
13. M. Díaz, A. Ortiz and I. Ortiz, *Journal of Membrane Science*, 2014, **469**, 379-396.
14. G. Merle, M. Wessling and K. Nijmeijer, *Journal of Membrane Science*, 2011, **377**, 1-35.
15. J. B. Goodenough and P. Singh, *Journal of The Electrochemical Society*, 2015, **162**, A2387-A2392.
16. D. W. Shin, M. D. Guiver and Y. M. Lee, *Chemical reviews*, 2017, **117**, 4759-4805.
17. C. Zhong, Y. Deng, W. Hu, J. Qiao, L. Zhang and J. Zhang, *Chemical Society reviews*, 2015, **44**, 7484-7539.
18. A. Currao, *CHIMIA International Journal for Chemistry*, 2007, **61**, 815-819.
19. A. J. Bard and M. A. Fox, *Accounts of Chemical Research*, 1995, **28**, 141-145.
20. S. U. Khan, M. Al-Shahry and W. B. Ingler, *science*, 2002, **297**, 2243-2245.
21. M. Armand, F. Endres, D. R. MacFarlane, H. Ohno and B. Scrosati, in *Materials for Sustainable Energy: A Collection of Peer-Reviewed Research and Review Articles from Nature Publishing Group*, World Scientific, 2011, pp. 129-137.
22. T. Kuboki, T. Okuyama, T. Ohsaki and N. Takami, *Journal of power sources*, 2005, **146**, 766-769.
23. M. Galiński, A. Lewandowski and I. Stępniak, *Electrochimica acta*, 2006, **51**, 5567-5580.

24. Y. J. Wang, J. Qiao, R. Baker and J. Zhang, *Chemical Society reviews*, 2013, **42**, 5768-5787.
25. L. Fan, S. Wei, S. Li, Q. Li and Y. Lu, *Advanced Energy Materials*, 2018, **8**, 1702657.
26. W. Li, J. R. Dahn and D. S. Wainwright, *Science*, 1994, **264**, 1115-1118.
27. W.-S. Huang, B. D. Humphrey and A. G. MacDiarmid, *Journal of the Chemical Society, Faraday Transactions 1: Physical Chemistry in Condensed Phases*, 1986, **82**, 2385-2400.
28. F. Beck and P. Rüetschi, *Electrochimica Acta*, 2000, **45**, 2467-2482.
29. A. Dey, *Journal of The Electrochemical Society*, 1971, **118**, 1547-1549.
30. P. Wang, S. M. Zakeeruddin, P. Comte, I. Exnar and M. Grätzel, *Journal of the American Chemical Society*, 2003, **125**, 1166-1167.
31. M. Ishikawa, T. Sugimoto, M. Kikuta, E. Ishiko and M. Kono, *Journal of power sources*, 2006, **162**, 658-662.
32. M. Armand, *Solid State Ionics*, 1983, **9**, 745-754.
33. P. G. Bruce, *Solid state electrochemistry*, Cambridge university press, 1997.
34. P. Hagenmuller and W. Van Gool, *Solid electrolytes: general principles, characterization, materials, applications*, Elsevier, 2015.
35. D. Almond and A. West, *Solid State Ionics*, 1983, **9**, 277-282.
36. D. Almond, G. Duncan and A. West, *Solid State Ionics*, 1983, **8**, 159-164.
37. J. Fu, Z. P. Cano, M. G. Park, A. Yu, M. Fowler and Z. Chen, *Advanced materials*, 2017, **29**.
38. J. Miao, F.-X. Xiao, H. B. Yang, S. Y. Khoo, J. Chen, Z. Fan, Y.-Y. Hsu, H. M. Chen, H. Zhang and B. Liu, *Science advances*, 2015, **1**, e1500259.
39. M. Pasta, C. D. Wessells, R. A. Huggins and Y. Cui, *Nature communications*, 2012, **3**, 1149.
40. J. Besenhard, M. Winter, J. Yang and W. Biberacher, *Journal of Power Sources*, 1995, **54**, 228-231.
41. M. R. Wright, *An introduction to aqueous electrolyte solutions*, John Wiley & Sons, 2007.
42. K. Naoi, S. Ishimoto, J.-i. Miyamoto and W. Naoi, *Energy & Environmental Science*, 2012, **5**, 9363-9373.
43. B. E. Conway, *Electrochemical supercapacitors: scientific fundamentals and technological applications*, Springer Science & Business Media, 2013.
44. S. Ishimoto, Y. Asakawa, M. Shinya and K. Naoi, *Journal of the Electrochemical Society*, 2009, **156**, A563-A571.
45. R. Kötz, M. Hahn and R. Gallay, *Journal of Power Sources*, 2006, **154**, 550-555.
46. D. Fragiadakis, S. Dou, R. H. Colby and J. Runt, *Macromolecules*, 2008, **41**, 5723-5728.
47. R. J. Klein, S. Zhang, S. Dou, B. H. Jones, R. H. Colby and J. Runt, *The Journal of chemical physics*, 2006, **124**, 144903.
48. R. Wang, P. Wang, X. Yan, J. Lang, C. Peng and Q. Xue, *ACS applied materials & interfaces*, 2012, **4**, 5800-5806.
49. M. D. Levi, G. Salitra, N. Levy, D. Aurbach and J. Maier, *Nature materials*, 2009,

8, 872.
50. F. Blanc, M. Leskes and C. P. Grey, *Accounts of chemical research*, 2013, **46**, 1952-1963.
51. H. Wang, T. K.-J. Köster, N. M. Trease, J. Ségalini, P.-L. Taberna, P. Simon, Y. Gogotsi and C. P. Grey, *Journal of the American Chemical Society*, 2011, **133**, 19270-19273.
52. M. Deschamps, E. Gilbert, P. Azais, E. Raymundo-Piñero, M. R. Ammar, P. Simon, D. Massiot and F. Béguin, *Nature materials*, 2013, **12**, 351.
53. H. Wang, A. C. Forse, J. M. Griffin, N. M. Trease, L. Trognko, P.-L. Taberna, P. Simon and C. P. Grey, *Journal of the American Chemical Society*, 2013, **135**, 18968-18980.
54. S. Boukhalfa, D. Gordon, L. He, Y. B. Melnichenko, N. Nitta, A. Magasinski and G. Yushin, *ACS nano*, 2014, **8**, 2495-2503.
55. F. Bonhomme, J. Lassegues and L. Servant, *Journal of the Electrochemical Society*, 2001, **148**, E450-E458.
56. R. D. Rogers and K. R. Seddon, *Science*, 2003, **302**, 792-793.
57. R. D. Rogers and G. A. Voth, *Accounts of chemical research*, 2007, **40**, 1077.
58. Z. Wojnarowska and M. Paluch, *Journal of physics. Condensed matter : an Institute of Physics journal*, 2015, **27**, 073202.
59. A. Lewandowski and M. Galinski, *Journal of Power Sources*, 2007, **173**, 822-828.
60. A. Brandt, S. Pohlmann, A. Varzi, A. Balducci and S. Passerini, *MRS bulletin*, 2013, **38**, 554-559.
61. A. Lewandowski, A. Olejniczak, M. Galinski and I. Stepniak, *Journal of Power Sources*, 2010, **195**, 5814-5819.
62. J. G. Huddleston, A. E. Visser, W. M. Reichert, H. D. Willauer, G. A. Broker and R. D. Rogers, *Green chemistry*, 2001, **3**, 156-164.
63. Z. B. Zhou, H. Matsumoto and K. Tatsumi, *Chemistry–A European Journal*, 2005, **11**, 752-766.
64. J. Barthel, H.-J. Gores, G. Schmeer and R. Wachter, in *Physical and inorganic chemistry*, Springer, 1983, pp. 33-144.
65. M. Kunze, E. Paillard, S. Jeong, G. B. Appetecchi, M. Schönhoff, M. Winter and S. Passerini, *The Journal of Physical Chemistry C*, 2011, **115**, 19431-19436.
66. M. Kunze, S. Jeong, E. Paillard, M. Schönhoff, M. Winter and S. Passerini, *Advanced Energy Materials*, 2011, **1**, 274-281.
67. A. B. McEwen, S. F. McDevitt and V. R. Koch, *Journal of The Electrochemical Society*, 1997, **144**, L84-L86.
68. A. M. Stephan, *European polymer journal*, 2006, **42**, 21-42.
69. W. H. Meyer, *Advanced materials*, 1998, **10**, 439-448.
70. J. Song, Y. Wang and C. C. Wan, *Journal of power sources*, 1999, **77**, 183-197.
71. H. Fei, C. Yang, H. Bao and G. Wang, *Journal of Power Sources*, 2014, **266**, 488-495.
72. Y. Wang, Y. Song and Y. Xia, *Chemical Society reviews*, 2016, **45**, 5925-5950.
73. J. Fu, D. U. Lee, F. M. Hassan, L. Yang, Z. Bai, M. G. Park and Z. Chen, *Advanced materials*, 2015, **27**, 5617-5622.

74. C. W. Huang, C. A. Wu, S. S. Hou, P. L. Kuo, C. T. Hsieh and H. Teng, *Advanced Functional Materials*, 2012, **22**, 4677-4685.
75. M.-F. Hsueh, C.-W. Huang, C.-A. Wu, P.-L. Kuo and H. Teng, *The Journal of Physical Chemistry C*, 2013, **117**, 16751-16758.
76. S. N. Syahidah and S. Majid, *Electrochimica Acta*, 2013, **112**, 678-685.
77. Y.-D. Chiou, D.-S. Tsai, H. H. Lam, C.-h. Chang, K.-Y. Lee and Y.-S. Huang, *Nanoscale*, 2013, **5**, 8122-8129.
78. M. Schroeder, P. Isken, M. Winter, S. Passerini, A. Lex-Balducci and A. Balducci, *Journal of the Electrochemical Society*, 2013, **160**, A1753-A1758.
79. B. E. Francisco, C. M. Jones, S.-H. Lee and C. R. Stoldt, *Applied Physics Letters*, 2012, **100**, 103902.
80. A. Ulihin, Y. G. Mateyshina and N. Uvarov, *Solid State Ionics*, 2013, **251**, 62-65.
81. Q. Zhang, K. Scrafford, M. Li, Z. Cao, Z. Xia, P. M. Ajayan and B. Wei, *Nano letters*, 2014, **14**, 1938-1943.
82. P. R. Griffiths and J. A. De Haseth, *Fourier transform infrared spectrometry*, John Wiley & Sons, 2007.
83. B. C. Smith, *Fundamentals of Fourier transform infrared spectroscopy*, CRC press, 2011.
84. D. A. Shirley, *Physical Review B*, 1972, **5**, 4709-4714.
85. J. Chastain, R. C. King and J. Moulder, *Handbook of X-ray photoelectron spectroscopy: a reference book of standard spectra for identification and interpretation of XPS data*, Physical Electronics Eden Prairie, MN, 1995.
86. A. Guinier, *X-ray diffraction in crystals, imperfect crystals, and amorphous bodies*, Courier Corporation, 1994.
87. C. Suryanarayana and M. G. Norton, *X-ray diffraction: a practical approach*, Springer Science & Business Media, 2013.
88. J. Goldstein, D. E. Newbury, P. Echlin, D. C. Joy, A. D. Romig Jr, C. E. Lyman, C. Fiori and E. Lifshin, *Scanning electron microscopy and X-ray microanalysis: a text for biologists, materials scientists, and geologists*, Springer Science & Business Media, 2012.
89. D. B. Williams and C. B. Carter, in *Transmission electron microscopy*, Springer, 1996, pp. 3-17.
90. R. Fitzgerald, K. Keil and K. F. Heinrich, *Science*, 1968, **159**, 528-530.
91. D. Shindo and T. Oikawa, in *Analytical Electron Microscopy for Materials Science*, Springer, 2002, pp. 81-102.
92. I. M. Ward and J. Sweeney, *Mechanical properties of solid polymers*, John Wiley & Sons, 2012.
93. R. F. Landel and L. E. Nielsen, *Mechanical properties of polymers and composites*, CRC Press, 1993.
94. Q. Duan, S. Ge and C.-Y. Wang, *Journal of Power Sources*, 2013, **243**, 773-778.
95. T. A. Zawodzinski, C. Derouin, S. Radzinski, R. J. Sherman, V. T. Smith, T. E. Springer and S. Gottesfeld, *Journal of the electrochemical society*, 1993, **140**, 1041-1047.
96. T. Corrales, F. Catalina, C. Peinado, N. Allen and E. Fontan, *Journal of*

Photochemistry and Photobiology A: Chemistry, 2002, **147**, 213-224.
97. K. Akita and M. Kase, *Journal of Polymer Science Part A-1: Polymer Chemistry*, 1967, **5**, 833-848.
98. S.-M. Park and J.-S. Yoo, *Analytical chemistry*, 2003, **75**, 455 A-461 A.
99. S. Mikhailenko, M. Guiver and S. Kaliaguine, *Solid State Ionics*, 2008, **179**, 619-624.
100. Y. Sone, P. Ekdunge and D. Simonsson, *Journal of The Electrochemical Society*, 1996, **143**, 1254-1259.
101. W. Wang and V. Sprenkle, *Nat Chem*, 2016, **8**, 204-206.
102. J. Winsberg, T. Hagemann, T. Janoschka, M. D. Hager and U. S. Schubert, *Angewandte Chemie*, 2017, **56**, 686-711.
103. W. Wang, Q. Luo, B. Li, X. Wei, L. Li and Z. Yang, *Advanced Functional Materials*, 2013, **23**, 970-986.
104. B. Huskinson, M. P. Marshak, C. Suh, S. Er, M. R. Gerhardt, C. J. Galvin, X. Chen, A. Aspuru-Guzik, R. G. Gordon and M. J. Aziz, *Nature*, 2014, **505**, 195-198.
105. T. Janoschka, N. Martin, U. Martin, C. Friebe, S. Morgenstern, H. Hiller, M. D. Hager and U. S. Schubert, *Nature*, 2015, **527**, 78-81.
106. A. Orita, M. G. Verde, M. Sakai and Y. S. Meng, *Nat Commun*, 2016, **7**, 13230.
107. K. Lin, R. Gómez-Bombarelli, E. S. Beh, L. Tong, Q. Chen, A. Valle, A. Aspuru-Guzik, M. J. Aziz and R. G. Gordon, *Nature Energy*, 2016, **1**, 16102.
108. T. Janoschka, N. Martin, M. D. Hager and U. S. Schubert, *Angewandte Chemie International Edition*, 2016, **55**, 14427-14430.
109. C. S. Sevov, D. P. Hickey, M. E. Cook, S. G. Robinson, S. Barnett, S. D. Minteer, M. S. Sigman and M. S. Sanford, *Journal of the American Chemical Society*, 2017, **139**, 2924-2927.
110. W. Wang, W. Xu, L. Cosimbescu, D. Choi, L. Li and Z. Yang, *Chemical communications*, 2012, **48**, 6669-6671.
111. T. Liu, X. Wei, Z. Nie, V. Sprenkle and W. Wang, *Advanced Energy Materials*, 2016, **6**, 1501449.
112. X.-P. Gao and H.-X. Yang, *Energy Environ. Sci.*, 2010, **3**, 174-189.
113. L. Chen, Z. Guo, Y. Xia and Y. Wang, *Chemical communications*, 2013, **49**, 2204-2206.
114. F. R. Brushett, J. T. Vaughey and A. N. Jansen, *Advanced Energy Materials*, 2012, **2**, 1390-1396.
115. H. Chen, Q. Zou, Z. Liang, H. Liu, Q. Li and Y. C. Lu, *Nat Commun*, 2015, **6**, 5877.
116. Y. Ding, Y. Zhao, Y. Li, J. B. Goodenough and G. Yu, *Energy Environ. Sci.*, 2017.
117. W. Duan, J. Huang, J. A. Kowalski, I. A. Shkrob, M. Vijayakumar, E. Walter, B. Pan, Z. Yang, J. D. Milshtein, B. Li, C. Liao, Z. Zhang, W. Wang, J. Liu, J. S. Moore, F. R. Brushett, L. Zhang and X. Wei, *ACS Energy Letters*, 2017, **2**, 1156-1161.
118. Q. Huang, J. Yang, C. B. Ng, C. Jia and Q. Wang, *Energy Environ. Sci.*, 2016, **9**, 917-921.
119. X. Wei, W. Xu, M. Vijayakumar, L. Cosimbescu, T. Liu, V. Sprenkle and W. Wang, *Advanced materials*, 2014, **26**, 7649-7653.
120. Y. Yang, G. Zheng and Y. Cui, *Energy & Environmental Science*, 2013, **6**, 1552.

121. X. Wei, L. Cosimbescu, W. Xu, J. Z. Hu, M. Vijayakumar, J. Feng, M. Y. Hu, X. Deng, J. Xiao, J. Liu, V. Sprenkle and W. Wang, *Advanced Energy Materials*, 2015, **5**, 1400678.
122. N. Li, Z. Weng, Y. Wang, F. Li, H.-M. Cheng and H. Zhou, *Energy Environ. Sci.*, 2014, **7**, 3307-3312.
123. Y. Zhao, M. Hong, N. Bonnet Mercier, G. Yu, H. C. Choi and H. R. Byon, *Nano letters*, 2014, **14**, 1085-1092.
124. Y. Zhao, L. Wang and H. R. Byon, *Nat Commun*, 2013, **4**, 1896.
125. Y. Ding and G. Yu, *Angewandte Chemie*, 2016, **55**, 4772-4776.
126. R. M. Darling, K. G. Gallagher, J. A. Kowalski, S. Ha and F. R. Brushett, *Energy Environ. Sci.*, 2014, **7**, 3459-3477.
127. S. Gu, K. Gong, E. Z. Yan and Y. Yan, *Energy Environ. Sci.*, 2014, **7**, 2986-2998.
128. G.-M. Weng, Z. Li, G. Cong, Y. Zhou and Y.-C. Lu, *Energy Environ. Sci.*, 2017.
129. B. Li, Z. Nie, M. Vijayakumar, G. Li, J. Liu, V. Sprenkle and W. Wang, *Nat Commun*, 2015, **6**, 6303.
130. Y. Li and H. Dai, *Chemical Society reviews*, 2014, **43**, 5257-5275.
131. Y. Li and H. Dai, *Chemical Society reviews*, 2014, **43**, 5257-5275.
132. J. Zhang, J. Fu, X. Song, G. Jiang, H. Zarrin, P. Xu, K. Li, A. Yu and Z. Chen, *Advanced Energy Materials*, 2016, **6**, 1600476.
133. J. Fu, F. M. Hassan, C. Zhong, J. Lu, H. Liu, A. Yu and Z. Chen, *Advanced materials*, 2017, **29**, 1702526.
134. W. A. Braff, M. Z. Bazant and C. R. Buie, *Nat Commun*, 2013, **4**, 2346.
135. Z. Yuan, Y. Duan, H. Zhang, X. Li, H. Zhang and I. Vankelecom, *Energy Environ. Sci.*, 2016, **9**, 441-447.
136. Z. Yuan, X. Zhu, M. Li, W. Lu, X. Li and H. Zhang, *Angewandte Chemie*, 2016, **55**, 3058-3062.
137. Y. Zhao, M. Li, Z. Yuan, X. Li, H. Zhang and I. F. J. Vankelecom, *Advanced Functional Materials*, 2016, **26**, 210-218.
138. B. Li, J. Liu, Z. Nie, W. Wang, D. Reed, J. Liu, P. McGrail and V. Sprenkle, *Nano letters*, 2016, **16**, 4335-4340.
139. Z. Li, G. Weng, Q. Zou, G. Cong and Y.-C. Lu, *Nano Energy*, 2016, **30**, 283-292.
140. S. Roe, C. Menictas and M. Skyllas-Kazacos, *Journal of The Electrochemical Society*, 2015, **163**, A5023-A5028.
141. J. Fu, D. U. Lee, F. M. Hassan, L. Yang, Z. Bai, M. G. Park and Z. Chen, *Adv Mater*, 2015.
142. S. H. Kim, K. H. Choi, S. J. Cho, S. Choi, S. Park and S. Y. Lee, *Nano Lett*, 2015, **15**, 5168-5177.
143. S.-Y. Lee, K.-H. Choi, W.-S. Choi, Y. H. Kwon, H.-R. Jung, H.-C. Shin and J. Y. Kim, *Energy & Environmental Science*, 2013, **6**, 2414.
144. G. Nystrom, A. Marais, E. Karabulut, L. Wagberg, Y. Cui and M. M. Hamedi, *Nat Commun*, 2015, **6**, 7259.
145. D. Higgins, Z. Chen, D. U. Lee and Z. Chen, *Journal of Materials Chemistry A*, 2013, **1**, 2639.
146. H. W. Park, D. U. Lee, Y. Liu, J. Wu, L. F. Nazar and Z. Chen, *Journal of the*

Electrochemical Society, 2013, **160**, A2244-A2250.
147. N. Liu, Z. Lu, J. Zhao, M. T. McDowell, H. W. Lee, W. Zhao and Y. Cui, *Nat Nanotechnol*, 2014, **9**, 187-192.
148. J. S. Lee, S. Tai Kim, R. Cao, N. S. Choi, M. Liu, K. T. Lee and J. Cho, *Advanced Energy Materials*, 2011, **1**, 34-50.
149. R. Cao, J. S. Lee, M. Liu and J. Cho, *Advanced Energy Materials*, 2012, **2**, 816-829.
150. M. Park, H. Sun, H. Lee, J. Lee and J. Cho, *Advanced Energy Materials*, 2012, **2**, 780-800.
151. D. U. Lee, J. Fu, M. G. Park, H. Liu, A. Ghorbani Kashkooli and Z. Chen, *Nano Lett*, 2016.
152. Z. Chen, J.-Y. Choi, H. Wang, H. Li and Z. Chen, *Journal of Power Sources*, 2011, **196**, 3673-3677.
153. D. U. Lee, J. Y. Choi, K. Feng, H. W. Park and Z. Chen, *Advanced Energy Materials*, 2014, **4**.
154. Y. Li, M. Gong, Y. Liang, J. Feng, J.-E. Kim, H. Wang, G. Hong, B. Zhang and H. Dai, *Nat Commun*, 2013, **4**, 1805.
155. X. Liu, M. Park, M. G. Kim, S. Gupta, G. Wu and J. Cho, *Angew Chem Int Ed Engl*, 2015, **54**, 9654-9658.
156. J. Park, M. Park, G. Nam, J. s. Lee and J. Cho, *Advanced Materials*, 2015, **27**, 1395-1395.
157. Y. Xu, Y. Zhang, Z. Guo, J. Ren, Y. Wang and H. Peng, *Angew Chem Int Ed Engl*, 2015.
158. J. Fu, J. Zhang, X. Song, H. Zarrin, X. Tian, J. Qiao, L. Rasen, K. Li and Z. Chen, *Energy Environ. Sci.*, 2016, **9**, 663-670.
159. D. U. Lee, H. W. Park, M. G. Park, V. Ismayilov and Z. Chen, *ACS Applied Materials & Interfaces*, 2015, **7**, 902-910.
160. J. Zhang, J. Qiao, G. Jiang, L. Liu and Y. Liu, *Journal of Power Sources*, 2013, **240**, 359-367.
161. S. Gu, R. Cai, T. Luo, Z. Chen, M. Sun, Y. Liu, G. He and Y. Yan, *Angew Chem Int Ed Engl*, 2009, **48**, 6499-6502.
162. S. Gu, J. Wang, R. B. Kaspar, Q. Fang, B. Zhang, E. Bryan Coughlin and Y. Yan, *Scientific reports*, 2015, **5**, 11668.
163. G. Jiang, M. Goledzinowski, F. J. E. Comeau, H. Zarrin, G. Lui, J. Lenos, A. Veileux, G. Liu, J. Zhang, S. Hemmati, J. Qiao and Z. Chen, *Advanced Functional Materials*, 2016, n/a-n/a.
164. H. Zarrin, D. Higgins, Y. Jun, Z. Chen and M. Fowler, *The Journal of Physical Chemistry C*, 2011, **115**, 20774-20781.
165. H. Zarrin, J. Fu, G. Jiang, S. Yoo, J. Lenos, M. Fowler and Z. Chen, *ACS Nano*, 2015, **9**, 2028-2037.
166. S. Yu, N. Li, D. Higgins, D. Li, Q. Li, H. Xu, J. S. Spendelow and G. Wu, *ACS Appl Mater Interfaces*, 2014, **6**, 19783-19790.
167. H. W. Kim, H. W. Yoon, S.-M. Yoon, B. M. Yoo, B. K. Ahn, Y. H. Cho, H. J. Shin, H. Yang, U. Paik and S. Kwon, *Science*, 2013, **342**, 91-95.

168. D. A. Dikin, S. Stankovich, E. J. Zimney, R. D. Piner, G. H. Dommett, G. Evmenenko, S. T. Nguyen and R. S. Ruoff, *Nature*, 2007, **448**, 457-460.
169. W. Gao, G. Wu, M. T. Janicke, D. A. Cullen, R. Mukundan, J. K. Baldwin, E. L. Brosha, C. Galande, P. M. Ajayan, K. L. More, A. M. Dattelbaum and P. Zelenay, *Angew Chem Int Ed Engl*, 2014, **53**, 3588-3593.
170. C. N. Yeh, K. Raidongia, J. Shao, Q. H. Yang and J. Huang, *Nat Chem*, 2014, **7**, 166-170.
171. A. Yu, I. Roes, A. Davies and Z. Chen, *Applied Physics Letters*, 2010, **96**, 253105.
172. Y. Li, H. Zhu, F. Shen, J. Wan, S. Lacey, Z. Fang, H. Dai and L. Hu, *Nano Energy*, 2015, **13**, 346-354.
173. K. Rohrbach, Y. Li, H. Zhu, Z. Liu, J. Dai, J. Andreasen and L. Hu, *Chem Commun (Camb)*, 2014, **50**, 13296-13299.
174. H. Zhu, Z. Jia, Y. Chen, N. Weadock, J. Wan, O. Vaaland, X. Han, T. Li and L. Hu, *Nano Lett*, 2013, **13**, 3093-3100.
175. L. Hu, G. Zheng, J. Yao, N. Liu, B. Weil, M. Eskilsson, E. Karabulut, Z. Ruan, S. Fan, J. T. Bloking, M. D. McGehee, L. Wågberg and Y. Cui, *Energy Environ. Sci.*, 2013, **6**, 513-518.
176. J. Qiao, J. Zhang and J. Zhang, *Journal of Power Sources*, 2013, **237**, 1-4.
177. J. Zhang, T. Zhou, J. Qiao, Y. Liu and J. Zhang, *Electrochimica Acta*, 2013, **111**, 351-358.
178. H. Zhu, B. B. Narakathu, Z. Fang, A. Tausif Aijazi, M. Joyce, M. Atashbar and L. Hu, *Nanoscale*, 2014, **6**, 9110-9115.
179. K. K. Sadasivuni, A. Kafy, L. Zhai, H.-U. Ko, S. Mun and J. Kim, *Small*, 2015, **11**, 994-1002.
180. D. A. Dikin, S. Stankovich, E. J. Zimney, R. D. Piner, G. H. Dommett, G. Evmenenko, S. T. Nguyen and R. S. Ruoff, *Nature*, 2007, **448**, 457-460.
181. R. Ludwig, *Angewandte Chemie International Edition*, 2003, **42**, 258-260.
182. M. Xu, D. Ivey, Z. Xie and W. Qu, *Journal of Power Sources*, 2015, **283**, 358-371.
183. A. R. Mainar, O. Leonet, M. Bengoechea, I. Boyano, I. de Meatza, A. Kvasha, A. Guerfi and J. Alberto Blázquez, *International Journal of Energy Research*, 2016, n/a-n/a.
184. Z. Q. Zheng, J. D. Yao, B. Wang and G. W. Yang, *Scientific reports*, 2015, **5**, 11070.
185. J. Zhang, X. Liu, G. Neri and N. Pinna, *Advanced materials*, 2016, **28**, 795-831.
186. J. R. Stetter, W. R. Penrose and S. Yao, *Journal of The Electrochemical Society*, 2003, **150**, S11.
187. K. Xu, C. Fu, Z. Gao, F. Wei, Y. Ying, C. Xu and G. Fu, *Instrumentation Science & Technology*, 2017, **46**, 115-145.
188. K. Kalantar-zadeh, J. Z. Ou, T. Daeneke, A. Mitchell, T. Sasaki and M. S. Fuhrer, *Applied Materials Today*, 2016, **5**, 73-89.
189. C. Park, J. Fergus, N. Miura, J. Park and A. Choi, *Ionics*, 2009, **15**, 261-284.
190. G. Jiang, M. Goledzinowski, F. J. Comeau, H. Zarrin, G. Lui, J. Lenos, A. Veileux, G. Liu, J. Zhang and S. Hemmati, *Advanced Functional Materials*, 2016.
191. W. Zeng, L. Shu, Q. Li, S. Chen, F. Wang and X. M. Tao, *Advanced materials*, 2014, **26**, 5310-5336.

192. S. Yao, Y. Shimizu, N. Miura and N. Yamazoe, *Chemistry letters*, 1990, 2033-2036.
193. H. Aono and Y. Sadaoka, *Journal of The Electrochemical Society*, 2000, **147**, 4363-4367.
194. L. Hu and Y. Cui, *Energy & Environmental Science*, 2012, **5**, 6423.
195. L. Hu, M. Pasta, F. L. Mantia, L. Cui, S. Jeong, H. D. Deshazer, J. W. Choi, S. M. Han and Y. Cui, *Nano letters*, 2010, **10**, 708-714.
196. L. Hu, N. Liu, M. Eskilsson, G. Zheng, J. McDonough, L. Wågberg and Y. Cui, *Nano Energy*, 2013, **2**, 138-145.
197. J. Zhang, J. Fu, X. Song, G. Jiang, H. Zarrin, P. Xu, K. Li, A. Yu and Z. Chen, *Advanced Energy Materials*, 2016, **6**, 1600476.
198. K. J. Berean, J. Z. Ou, T. Daeneke, B. J. Carey, E. P. Nguyen, Y. Wang, S. P. Russo, R. B. Kaner and K. Kalantar-Zadeh, *Small*, 2015, **11**, 5035-5040.
199. K. J. Berean, J. Z. Ou, M. Nour, M. R. Field, M. M. Y. A. Alsaif, Y. Wang, R. Ramanathan, V. Bansal, S. Kentish, C. M. Doherty, A. J. Hill, C. McSweeney, R. B. Kaner and K. Kalantar-zadeh, *The Journal of Physical Chemistry C*, 2015, **119**, 13700-13712.
200. R. Kumar, M. Mamlouk and K. Scott, *International Journal of Electrochemistry*, 2011, **2011**, 1-7.
201. Y. Li, H. Zhu, S. Zhu, J. Wan, Z. Liu, O. Vaaland, S. Lacey, Z. Fang, H. Dai and T. Li, *NPG Asia Materials*, 2015, **7**, e150.
202. Y. Chen, H. Qin, Y. Cao, H. Zhang and J. Hu, *Sensors*, 2018, **18**.
203. J. L. Morgan, J. Strumillo and J. Zimmer, *Nature*, 2013, **493**, 181-186.
204. J. Zhang, L. Yue, P. Hu, Z. Liu, B. Qin, B. Zhang, Q. Wang, G. Ding, C. Zhang, X. Zhou, J. Yao, G. Cui and L. Chen, *Scientific reports*, 2014, **4**, 6272.
205. S. Y. Oh, D. I. Yoo, Y. Shin and G. Seo, *Carbohydrate Research*, 2005, **340**, 417-428.
206. K. K. Sadasivuni, A. Kafy, L. Zhai, H. U. Ko, S. Mun and J. Kim, *Small*, 2015, **11**, 994-1002.
207. J.-L. Huang, C.-J. Li and D. G. Gray, *RSC Advances*, 2014, **4**, 6965.
208. Y. Chen, X. Zhang, D. Zhang, P. Yu and Y. Ma, *Carbon*, 2011, **49**, 573-580.
209. S. Yokota, T. Kitaoka, J. Sugiyama and H. Wariishi, *Advanced materials*, 2007, **19**, 3368-3370.
210. H. Hamze, M. Jimenez, D. Deresmes, A. Beaurain, N. Nuns and M. Traisnel, *Applied Surface Science*, 2014, **315**, 531-537.
211. M. Y. Bashouti, R. T. Tung and H. Haick, *Small*, 2009, **5**, 2761-2769.
212. T. Soboleva, Z. Xie, Z. Shi, E. Tsang, T. Navessin and S. Holdcroft, *Journal of Electroanalytical Chemistry*, 2008, **622**, 145-152.
213. A. A. Argun, J. N. Ashcraft and P. T. Hammond, *Advanced materials*, 2008, **20**, 1539-1543.
214. J. Li, J. K. Park, R. B. Moore and L. A. Madsen, *Nature materials*, 2011, **10**, 507-511.
215. M. R. Karim, K. Hatakeyama, T. Matsui, H. Takehira, T. Taniguchi, M. Koinuma, Y. Matsumoto, T. Akutagawa, T. Nakamura, S. Noro, T. Yamada, H. Kitagawa and S. Hayami, *Journal of the American Chemical Society*, 2013, **135**, 8097-8100.

216. K. Hatakeyama, M. R. Karim, C. Ogata, H. Tateishi, A. Funatsu, T. Taniguchi, M. Koinuma, S. Hayami and Y. Matsumoto, *Angewandte Chemie*, 2014, **53**, 6997-7000.
217. S. K. Dishari and M. A. Hickner, *ACS Macro Letters*, 2012, **1**, 291-295.
218. Q. Li, *Solid State Ionics*, 2004, **168**, 177-185.
219. S.-R. Kim, B. A. Getachew, S.-J. Park, O.-S. Kwon, W.-H. Ryu, A. D. Taylor, J. Bae and J.-H. Kim, *Environmental Science & Technology Letters*, 2016, **3**, 216-221.